

**MODIFICATION OF MAGNESIUM  
HYDRIDE BY TRANSITION METAL  
CARBIDES FOR HYDROGEN  
STORAGE**

By  
Mi Tian

A thesis submitted for the degree of  
Master by Research in the Faculty of Science  
at the University of East Anglia  
September 2010

I, Mi Tian, confirm that the work presented in this thesis is my own. Where information has been derived from other sources, I confirm that this has been indicated in the thesis.

## ABSTRACT

Magnesium hydride is a promising compound for hydrogen storage but suffers from a high desorption temperature and slow desorption kinetics. This project focuses on improving these properties by modifying the particle size, structure and phases of the material using mechanical milling techniques and doping with transition metal carbides, e.g. TiC and Mo<sub>2</sub>C. Scanning Electron Microscopy (SEM) and X-Ray Diffraction (XRD) were employed to characterize the morphologies and structures of the samples. The dehydrogenation/rehydrogenation properties were evaluated using an intelligent gravimetric analyzer (IGA).

Hydrogen absorption of dehydrogenated MgH<sub>2</sub> was enhanced by both cryogenic milling and ball-milling. The hydrogen content was increased greatly to 4 wt. % after 60 min absorption at 300 °C and 8 bar hydrogen pressure, compared to that of dehydrogenated as-received MgH<sub>2</sub> (< 0.5 wt. %), due to 8 h cryomilling and further 60 h ball-milling.

The hydrogen desorption temperature of MgH<sub>2</sub> catalyzed by 2 mol % TiC was significantly lower (190 °C) than that of the as-received MgH<sub>2</sub> (418 °C). The desorption improved further in terms of temperature and kinetics following the addition of 8 mol % TiC. TiC shows an effective catalytic influence upon the H<sub>2</sub> sorption of Mg/MgH<sub>2</sub>, which is stable during H<sub>2</sub> uptake and release with no reaction with Mg or MgH<sub>2</sub>. Whilst the reduction of nano particle and grain size by milling has a positive effect on the hydrogen storage properties of MgH<sub>2</sub>. Molybdenum carbide Mo<sub>2</sub>C does not seem to influence the hydrogen desorption temperature of MgH<sub>2</sub> and has a little effect on hydrogen absorption kinetics. With the addition of Ni in the milled (MgH<sub>2</sub> + TiC) mixture, there was no further reduction in desorption temperature. The work proves that nano-sized TiC particles are inserted into the grain boundary or inner

space of  $\text{MgH}_2$ .  $\text{TiC}$  is an effective and stable catalyst that does improve the hydrogen sorption properties of  $\text{MgH}_2$ .

In order to evaluate the possible effects of impurities on hydrogen sorption of  $\text{Mg}$ , a preliminary study was carried out using a gas mixture of (80 %  $\text{H}_2$  + 20 %  $\text{CO}_2$ ) to charge dehydrogenated  $\text{MgH}_2$  with and without transition metal carbides at a pressure of 8 bar and a temperature of 300 °C in an IGA coupled with mass-spectrometer (MS). The reactions of  $\text{Mg}$  (from dehydrogenated  $\text{MgH}_2$ ) with the (80%  $\text{H}_2$  + 20%  $\text{CO}_2$ ) gas mixture at 300 °C are rather complex. Magnesium preferentially reacts with  $\text{H}_2$  due to the high content of  $\text{H}_2$  in the gas mixture. This is followed by  $\text{MgH}_2$  reacting with  $\text{CO}_2$  to form other gases, such as  $\text{CO}$  and  $\text{H}_2\text{O}$  and solids such as  $\text{MgO}$ , which reacts easily with  $\text{CO}_2$  to form  $\text{MgCO}_3$ . The results prove  $\text{CO}_2$  poisons the hydrogenation process of  $\text{Mg}$ , and provide useful information to further investigate materials for hydrogen storage or purification from the mixture gas streams of  $\text{H}_2/\text{CO}_2$  or  $\text{H}_2/\text{CO}_2/\text{CO}$ .

## **ACKNOWLEDGEMENT**

I would like to take this opportunity to thank a number of people for their contributions to this work, without which this thesis would not have been possible. Foremost, I would like to express my sincere gratitude to my supervisor, Dr. Congxiao Shang, for her continuous support during my Master by Research, for her patience, motivation, enthusiasm, immense knowledge, and guidance have helped me throughout my research and whilst writing up this thesis. I could not have imagined having a better supervisor and mentor for my master study. My sincere thanks also go to Dr. John Brindle for his technical help, and Mr. Chris Roberts and Dr. Lawson Baxter for proofreading my thesis.

Many thanks also to the academic and technical staff of the School of Environmental Science, within the University of East Anglia, for providing a friendly and worry-free environment. The friendship I have made during my time here have really helped me through lots of difficulties, and brightened up my life in the UK, particularly, Dr. Ping Jiang, Dr. Yu Liu, Qiao Li, Jianping Tian, Lien Huong Du and Dr. Matthew Bolton to mention just a few.

Last but not the least, I would like to thank my parents Lianzhang Tian and Chunmei Wang and my husband for their continuous support and endless love throughout my life.

**TABLE OF CONTENTS**

Abstract .....	I
Acknowledgement .....	III
Table of Contents.....	IV
List of Figure Captions .....	VII
List of Table Captions.....	X
Chapter 1 Introduction.....	1
Chapter 2 Literature Review.....	8
2.1 Hydrogen Storage Methods .....	8
2.1.1 Physical adsorbents.....	11
2.1.2 Metal hydrides.....	13
2.1.3 Complex hydrides .....	16
2.1.4 Storage via chemical reactions.....	18
2.2 Parameters for Hydrogen Storage in Hydrides .....	19
2.2.1 Mechanism of hydrogen absorption.....	19
2.2.2 Capacity .....	22
2.2.3 Hydrogen sorption kinetics and sorption temperature .....	23
2.2.4 Cycle-life and stability .....	25
2.3 Mg for Hydrogen Storage .....	25
2.3.1 Properties of Mg/MgH <sub>2</sub> .....	26
2.3.2 Limitation of MgH <sub>2</sub> for practical application.....	26
2.3.3 Approaches to improve sorption properties of Magnesium Hydride .....	28
2.4 Improvement of Kinetics by Milling .....	32
2.5 Alloying with other Elements and Catalyst .....	34
2.5.1 Alloying with other elements.....	34
2.5.2 Catalysis.....	35
2.6 Aims and Objectives .....	38
Chapter 3 Experimental Methods .....	39
3.1 Materials and Sample Preparation .....	39
3.1.1 Materials .....	39
3.1.2 Sample preparation .....	39

---

3.1.3	Glove box.....	40
3.1.4	Cryogenic milling .....	41
3.1.5	Ball milling .....	41
3.2	Analysis of Sample Morphology and Structure .....	42
3.2.1	X-ray diffraction (XRD) .....	42
3.2.2	Scanning Electron Microscopy (SEM) and Transmission Electron Microscopy (TEM) .....	43
3.3	Analysis of Hydrogen Sorption Properties: Intelligent Gravimetric Analyzer -Mass Spectrometry (IGA-MS) .....	44
Chapter 4	Experimental Results and Discussions .....	50
4.1	Particle Size and Grain Size Effects on Sorption Properties of MgH <sub>2</sub> .....	50
4.1.1	Structural characterizations of MgH <sub>2</sub> powder produced by cryogenic milling and ball milling .....	50
4.1.2	Dehydrogenation of MgH <sub>2</sub> by cryogenic milling and ball milling .....	54
4.1.3	Hydrogenation of MgH <sub>2</sub> by cryogenic milling and subsequent ball milling .	58
4.1.4	Summary .....	59
4.2	Effects of TiC Nanoparticles on Hydrogen Sorption of MgH <sub>2</sub> .....	60
4.2.1	Structural characterizations of milled mixtures of MgH <sub>2</sub> and TiC .....	60
4.2.2	Dehydrogenation of milled mixtures of MgH <sub>2</sub> and TiC .....	67
4.2.3	Hydrogenation of milled mixtures of MgH <sub>2</sub> and TiC .....	70
4.2.4	Summary .....	71
4.3	Effects of Mo <sub>2</sub> C Nanoparticles on Hydrogen Sorption Properties of MgH <sub>2</sub> .....	71
4.3.1	Structural characterizations of milled mixtures of MgH <sub>2</sub> and Mo <sub>2</sub> C .....	72
4.3.2	Dehydrogenation of milled mixtures of MgH <sub>2</sub> and Mo <sub>2</sub> C .....	76
4.3.3	Hydrogen absorption of milled mixtures of MgH <sub>2</sub> and Mo <sub>2</sub> C .....	79
4.3.4	Summary .....	80
4.4	Effects of Ni Nanoparticles on Hydrogen Desorption Properties of 60 h Ball- milled (MgH <sub>2</sub> +TiC or Mo <sub>2</sub> C).....	80
4.4.1	Structural characterizations of (MgH <sub>2</sub> + TiC/Mo <sub>2</sub> C+ 2 mol.% Ni) mixtures	81
4.4.2	Dehydrogenation of milled mixtures of MgH <sub>2</sub> and catalysts .....	83
4.4.3	Summary .....	85
4.5	Effects of Selected Gas Mixture of (H <sub>2</sub> + CO <sub>2</sub> ) on Hydrogen Sorption of MgH <sub>2</sub> ..	86
4.5.1	(H <sub>2</sub> + CO <sub>2</sub> ) absorption of dehydrogenated cryomilled MgH <sub>2</sub> .....	87

---

4.5.2	(H <sub>2</sub> + CO <sub>2</sub> ) absorption of dehydrogenated milled-(MgH <sub>2</sub> + TiC / MO <sub>2</sub> C).....	91
4.5.3	Interaction between Mg/MgH <sub>2</sub> and CO <sub>2</sub> gas.....	92
4.5.4	Summary .....	94
Chapter 5	General Discussion .....	95
5.1	The Effect of Milling Conditions on Microstructure and Hydrogen Sorption Properties of Magnesium Hydride. ....	95
5.2	The Catalytic Mechanism of TiC on Hydrogen Sorption Properties of Magnesium Hydride .....	99
5.2.1	Analysis of hydrogen sorption of MgH <sub>2</sub> catalyzed by TiC .....	99
5.2.2	Structure of TiC to improve catalytic effect .....	103
5.2.3	Thermodynamic stability of TiC for catalysis .....	104
5.2.4	Summary .....	105
5.3	Effect of Mo <sub>2</sub> C and Ni on Hydrogen Sorption Properties of MgH <sub>2</sub> .....	105
5.4	Interaction of Mg/MgH <sub>2</sub> with (H <sub>2</sub> +CO <sub>2</sub> ) Gas Mixture.....	106
Chapter 6	Conclusions and Future Work.....	108
6.1	Conclusions.....	108
6.2	Future Work.....	109
	References.....	111
	Publications and Presentations.....	122

## LIST OF FIGURE CAPTIONS

Figure 1-1 Status of hydrogen storage systems.....	5
Figure 2-1 Primitive phase diagram for hydrogen. Liquid hydrogen only exists between the solidus line and the line from the triple point at 21.2K and the critical point at 32K.....	9
Figure 2-2 Pressure composition isotherms for hydrogen absorption in a typical intermetallic compound on the left hand side. ....	15
Figure 2-3 Potential energy curve for the Lennard-Jones potential for hydrogen binding to a metal indicating.....	20
Figure 2-4 Simple representation of phase transition between the $\alpha$ phase and the $\beta$ phase.	22
Figure 2-5 An example of an energy barrier for hydrogenation and dehydrogenation.....	24
Figure 2-6 Different controlled milling modes available in the Uni-ball .....	33
Figure 3-1 The experimental framework .....	40
Figure 3-2 Synthesis in a glove box.....	40
Figure 3-3 SPEX SamplePrep 6750 Freezer/Mill and SPEX 8000D Mixer/Mill.....	40
Figure 3-4 Vial and impactor in the SPEX SamplePrep Freezer/Mill 6750 .....	41
Figure 3-5 Diagram of ball milling.....	42
Figure 3-6 Intelligent Gravimetric Analyzer combined with Mass Spectrometer.....	45
Figure 3-7 Gas sorption procedure in IGA-MS .....	46
Figure 4-1 X-ray diffraction patterns of the as-received $MgH_2$ , 8 h cryomilled $MgH_2$ and 60 h ball-milled $MgH_2$ after 8 h cryomilling. ....	52
Figure 4-2 SEM images of (a)as-received $MgH_2$ , (b) 8 h cryomilled $MgH_2$ , (c) 60 h ball-milled $MgH_2$ after cryomilling; and (d) particle sizes of them. ....	53
Figure 4-3 Thermogravimetry (TG) curves of cryomilled and ball-milled $MgH_2$ at the heating rate of 10 K/min and 1 bar helium pressure. ....	54
Figure 4-4 Derivative thermogravimetric (DTG) curves of cryomilled and further ball-milled $MgH_2$ , derived from Figure 4-3. ....	56

---

Figure 4-5 Kinetic plots and activation energy of the $\text{MgH}_2$ samples, based on Figure 4-4 and Equation 3-8 .....	57
Figure 4-6 Hydrogen absorption curves of the cryomilled and ball-milled $\text{MgH}_2$ , measured under 8 bar $\text{H}_2$ pressure at 300 °C .....	58
Figure 4-7 X-ray diffraction patterns of the as-received $\text{MgH}_2$ , TiC and the milled ( $\text{MgH}_2+2\text{mol.}\% \text{ TiC}$ ) mixtures.. .....	61
Figure 4-8 Grain sizes of $\text{MgH}_2$ and 2% TiC before and after milling. ....	62
Figure 4-9 SEM micrograph of (a) as-received $\text{MgH}_2$ , (b) as-received TiC, (c) ( $\text{MgH}_2+2\% \text{ TiC}$ ) cryomilled for 8 h, (d) ( $\text{MgH}_2+2\% \text{ TiC}$ ) ball milled for 16 h after cryomilling, (e) ( $\text{MgH}_2+2\% \text{ TiC}$ ) ball milled for 60h after cryomilling and (f) Back Scattering Electron (BSE) image of ( $\text{MgH}_2+2\% \text{ TiC}$ ) cryomilled for 8h. ....	64
Figure 4-10 Mean particle sizes of the milled ( $\text{MgH}_2+2\% \text{ TiC}$ ) mixtures, calculated from SEM images Figure 4-9. ....	65
Figure 4-11 TEM images of the samples cryomilled for 8 h and further ball milled for 60 h: (a) $\text{MgH}_2$ and (b) ( $\text{MgH}_2+\text{TiC}$ ) mixture (c)&(d) partial enlarged view from b. ....	65
Figure 4-12 Thermogravimetric (TG) curves of the $\text{MgH}_2$ milled with TiC .....	67
Figure 4-13 Derivative thermogravimetric (DTG) curves of the $\text{MgH}_2$ milled with TiC.....	67
Figure 4-14 Kinetic plots and activation energy of cryomilled and ball-milled ( $\text{MgH}_2+2\% \text{ TiC}$ ) and ball-milled .....	69
Figure 4-15 Hydrogen absorption curves of the $\text{MgH}_2$ catalyzed with and without TiC, measured under 8 bar $\text{H}_2$ pressure at 300 °C.....	70
Figure 4-16 XRD patterns of the as-received $\text{MgH}_2$ , $\text{Mo}_2\text{C}$ and milled ( $\text{MgH}_2+ \text{Mo}_2\text{C}$ ) mixtures.. .....	73
Figure 4-17 Grain sizes of $\text{MgH}_2$ and $\text{Mo}_2\text{C}$ before and after milling .....	74
Figure 4-18 SEM micrographs of (a) as-received $\text{Mo}_2\text{C}$ , (b) 8 h cryomilled ( $\text{MgH}_2+2\text{mol}\% \text{ Mo}_2\text{C}$ ), (c) BSE of cryomilled ( $\text{MgH}_2+2\text{mol}\% \text{ Mo}_2\text{C}$ ), (d) 60 h ball-milled ( $\text{MgH}_2+2\text{mol}\% \text{ Mo}_2\text{C}$ ) after cryomilling, and (e) BSE of ball-milled ( $\text{MgH}_2+2\text{mol}\% \text{ Mo}_2\text{C}$ ).....	75
Figure 4-19 Mean particle sizes of the milled ( $\text{MgH}_2+\text{Mo}_2\text{C}$ ).....	76
Figure 4-20 Thermogravimetric (TG) curves of $\text{MgH}_2$ milled with $\text{Mo}_2\text{C}$ .....	77
Figure 4-21 Derivative thermogravimetric (DTG) curves of the $\text{MgH}_2$ milled with $\text{Mo}_2\text{C}$ . .	78

---

Figure 4-22 Kinetic plots and activation energy of cryomilled and ball-milled ( $\text{MgH}_2 + \text{Mo}_2\text{C}$ ).....	78
Figure 4-23 Hydrogen absorption of $\text{MgH}_2$ catalyzed by $\text{Mo}_2\text{C}$ .....	79
Figure 4-24 XRD patterns of the as-received $\text{MgH}_2$ , $\text{TiC}$ , $\text{Mo}_2\text{C}$ , $\text{Ni}$ , ( $\text{MgH}_2 + \text{Mo}_2\text{C} + \text{Ni}$ ) and ( $\text{MgH}_2 + \text{TiC} + \text{Ni}$ ) .....	81
Figure 4-25 SEM-BSE images of ( $\text{MgH}_2 + \text{Mo}_2\text{C} + \text{Ni}$ ) .....	82
Figure 4-26 SEM-BSE images of ( $\text{MgH}_2 + \text{TiC} + \text{Ni}$ ) .....	82
Figure 4-27 Comparison of mean particle size of the milled samples .....	83
Figure 4-28 TG curves of the milled samples with $\text{Ni}$ .....	84
Figure 4-29 DTG curves of the milled samples with $\text{Ni}$ , derived from Figure 4-28 .....	84
Figure 4-30 TG-MS of the empty sample holder.....	87
Figure 4-31 TG-MS of the dehydrogenated cryomilled- $\text{MgH}_2$ .....	89
Figure 4-32 TG-MS of 2 <sup>nd</sup> decomposition of dehydrogenated cryomilled $\text{MgH}_2$ after $\text{H}_2 + \text{CO}_2$ absorption .....	90
Figure 4-33 XRD patterns of the samples.....	91
Figure 4-34 ( $\text{H}_2 + \text{CO}_2$ ) absorption of dehydrogenated $\text{MgH}_2$ with and without catalyst .....	92
Figure 4-35 TG-MS of $\text{CO}_2$ absorption of dehydrogenated cryomilled- $\text{MgH}_2$ . .....	93
Figure 4-36 TG-MS of $\text{CO}_2$ absorption of cryomilled- $\text{MgH}_2$ .....	94
Figure 5-1 Scheme of the ( $\text{MgH}_2 + \text{TiC}$ ) mixture in different states of dehydrogenation .....	102
Figure 5-2 (a) Crystal structure of $\text{TiC}$ , and (b) projection of $\text{Ti}-\text{C}$ atoms along $[111]$ direction. ....	104

---

## LIST OF TABLE CAPTIONS

Table 1-1 DOE technical targets: on-board hydrogen storage systems. ....	4
Table 2-1 Six basic hydrogen storage methods and phenomena. ....	10
Table 2-2 Adsorption Data for Metal–Organic Frameworks.....	12
Table 2-3 Volumetric and gravimetric hydrogen content in various materials.....	13
Table 2-4 the most important families of hydride-forming intermetallic compounds. ....	16
Table 2-5 Material Properties of Complex Hydrides.....	18
Table 2-6 Hydrogen sorption properties of Mg based hydrides .....	29
Table 3-1 Details of chemicals were used in the study at UEA.....	39
Table 4-1 Estimates of grain size (crystallite size), particle size of $\beta$ -MgH <sub>2</sub> from XRD and SEM analysis, and TG-DTG desorption temperature ( $T_{\text{Onset}}$ is onset temperature of desorption, $T_{\text{Peak}}$ is peak temperature of desorption.).....	59
Table 4-2 Onset & Peak desorption temperatures and absorption rates of the MgH <sub>2</sub> catalyzed by TiC. ....	68
Table 4-3 Onset & Peak desorption temperatures and absorption rates for the MgH <sub>2</sub> catalyzed with Mo <sub>2</sub> C.....	78
Table 5-1 Hydrogen sorption parameters of all samples. ....	98
Table 5-2 Atomic Structure of Ti, Ni and Mo .....	106

## CHAPTER 1 INTRODUCTION

The increase in threats from global warming due to the consumption of fossil fuels requires our planet to adopt new strategies to harness the inexhaustible sources of energy<sup>1, 2</sup>. CO<sub>2</sub> emission from burning fossil fuels has been clearly identified as the main culprit for global warming. Global CO<sub>2</sub> emission from fossil fuel combustion increases from 20.7 billion tones (Gross tonnage, Gt) in 1990 to 32.5 Gt in 2006 (9.9 Gt of carbon equivalent)<sup>3</sup>, currently growing 35% faster than expected because of high demand in fossil fuel use and the weakening of natural carbon sinks<sup>4</sup>. This has resulted in a sharp rise of atmospheric CO<sub>2</sub> from around 180–280 ppm in the last 400,000 years to >400 ppm in recent years (a quarter of the level that was once believed to cause extinction of all living species on land in the Triassic–Jurassic boundary, and it only takes less than 100 years to reach that level if no effective action is taken). Moreover, projected world energy demand will double by 2050, whereas available fossil fuels are likely to decline steeply after 20–30 years. There are quite a number of available alternative energy sources such as solar, wind, ocean, geothermal, hydrogen and others, but with a consideration regarding the application for transportation and environmental compatibility, hydrogen is concluded as one of the alternative fuels to fossil fuels<sup>5</sup>. Also hydrogen is an energy carrier which holds tremendous promise as a renewable and clean energy option<sup>2</sup>. In fact, hydrogen can be produced from a variety of sources including fossil fuels, renewables and water (by means of nuclear, wind or solar energy). It is non-toxic and extremely environmentally benign since water is the only exhaust product when hydrogen is converted into energy.

Despite obvious benefits, an immediate incorporation of hydrogen into the world economy faces a number of challenges. Unlike oil and natural gas, hydrogen has no large-scale infrastructure supporting its transportation. Although it is routinely used by chemical and

refining industries, the cost of hydrogen storage and delivery is too high for practiced applications, thus impeding the introduction of the hydrogen economy in which energy is stored and transported using hydrogen as a major energy carrier. The hydrogen economy Infrastructure is comprised of five key elements—Production, Delivery, Storage, Conversion, and Applications, which are in different stages of technological advancement<sup>6,7,8</sup>, described as following.

**Production**—Hydrogen can be produced using diverse, domestic resources including fossil fuels, such as natural gas and coal (with carbon sequestration); nuclear; biomass; and other renewable energy technologies, such as wind, solar, geothermal, and hydro-electric power.

**Delivery**—The existing infrastructure can be used to move the hydrogen from its point of production to an end-use device. Similar to natural gas distribution, pipelines are used to supply hydrogen to customers. Currently hydrogen pipelines have been used in a few areas of the United States<sup>9</sup>. Other options, such as blending with natural gas, a compressed gas or cryogenic liquid delivery as well as alternative hydrogen carriers (methanol, ethanol, and other organic liquids), are being considered.

**Conversion**—Hydrogen can be used both in engines and in fuel cells. Engines can combust hydrogen in the same manner as gasoline or natural gas, while fuel cells use the chemical energy of hydrogen to produce electricity and thermal energy. Since electrochemical reactions are more efficient than combustion at generating energy, fuel cells are more efficient than internal combustion engines.

**Application**—Hydrogen can be used in conventional power generation technologies, such as automobile engines and power plant turbines, or in fuel cells, which are relatively cleaner and more efficient than conventional technologies. Fuel cells have broad application

potential in both transportation and electrical power generation, including on-site generation for individual homes and office buildings.

Storage — Storage issues cut across the production, transport, delivery, and end-user applications of hydrogen as an energy carrier. Mobile applications are driving the development of safe, space-efficient, and cost-effective hydrogen storage systems, yet other applications will benefit substantially from all technological advances made for these on-board storage systems.

Hydrogen can be stored as a discrete gas or liquid or in a chemical compound. Currently available technologies permit the physical storage, transport, and delivery of gaseous or liquid hydrogen in tanks and pipeline systems. But none of the options in the market currently satisfy the needs of end users, which explains the growing interest and investment in hydrogen energy related research and development<sup>6</sup>. Compressed hydrogen storage is a mature technology, though improvements in cost, weight, and volume storage efficiency must continue to be made. Some automotive manufacturers are considering liquid hydrogen storage because of its good volumetric storage efficiency compared with compressed hydrogen; however the special handling requirements, long-term storage losses, and energy demands for liquefaction currently detract from its commercial viability. Metal hydrides offer the advantages of lower pressure storage, conformable shapes, and reasonable volumetric storage efficiency, but have weight penalties and thermal management issues. Although chemical hydrides present a potentially safer and more volumetrically efficient option, there are a number of challenges that must be addressed, including cost, recycling, overall energy efficiency, and infrastructure. Physical absorption materials with high surface areas are emerging, but the design of practical systems awaits a better understanding of the fundamental adsorption/desorption processes and development of mass production processes for the materials.

By translation vehicle performance requirements into storage system needs, U.S. Department of Energy (DOE) set a series of hydrogen storage targets for 2010 and 2015. A complete summary of DOE targets based on lower heating value of hydrogen and greater than 300-mile vehicle range is shown in Table 1-1. The targets are based on the U.S. weighted average corporate vehicle (WACV) that includes minivans, light trucks, economy cars, and SUV/crossover vehicles in proportion to their sales. Depending on progress in other areas related to hydrogen vehicle development, these targets have been altered in DOE 2009 Annual Progress Report<sup>10</sup> and may have to be altered in the future.

Table 1-1 DOE technical targets: on-board hydrogen storage systems<sup>11</sup>.

Storage Parameter	Units	2010	2015
Gravimetric Capacity	kWh/kg	2.0	3.0
	wt. % hydrogen	6	9
Volumetric Capacity	kWh/L	1.5	2.7
	g/L	45	81
Storage System Cost	\$/kWh	4	2
	\$/kg H <sub>2</sub>	133	67
Operating ambient Temperature	°C	-30/50 (sun) *	-46/60(sun) *
Min/Max delivery temperature	°C	-30/85	-40/85
Cycle life (1/4 tank to full)	Cycles	1 000	1 500
System Fill Time for 5 kg H <sub>2</sub>	min	3	2.5
Loss of usable H <sub>2</sub>	(g/h)kg H <sub>2</sub> stored	0.1	0.05

\* The notation (sun) indicates that the upper temperature is a hot soak condition in full direct sun, including radiant heat from the pavement.

Currently, research is focused on achieving the targets of volumetric and gravimetric capacity, while also meeting the energy and temperature requirements for hydrogen release and the kinetics of hydrogen charging and discharging. The current status of hydrogen storage system for vehicle is shown in Figure 1-1<sup>10</sup>, in comparison to the gravimetric and volumetric targets. An ideal hydrogen storage material should meet the targets at a high hydrogen capacity, low desorption temperature, moderate dissociation pressure, low heat dissipation during the exothermic hydride formation, good reversibility, fast kinetics, and low sensitivity to O<sub>2</sub> and moisture for long cycle life<sup>10</sup>.

On-board hydrogen storage approaches presently include compressed hydrogen gas, liquid hydrogen, high surface area adsorbents, and chemical hydrogen storage media, as already stated previously. Compressed and cryogenic hydrogen, adsorbents and some metal hydrides are categorized as “reversible” storage system which can be refilled with hydrogen completely, similar to gasoline refueling today. In contrast, some complex chemical hydrogen storage materials, such as  $\text{LiBH}_4$ ,  $\text{NaAlH}_4$  etc.. known as complex hydride, generally require a chemical reaction pathway to be regenerated to the original form, so the storage system cannot be directly refueled with hydrogen on-board the vehicle. Such systems are referred to as “off-board regenerable”, requiring the spent media to be removed from the vehicle and then regenerated with hydrogen either at the fueling station or at a centralized processing facility. Complex chemical storage materials may also serve as a hydrogen delivery carrier by providing an alternative to transporting hydrogen as a gas or cryogenic liquid.

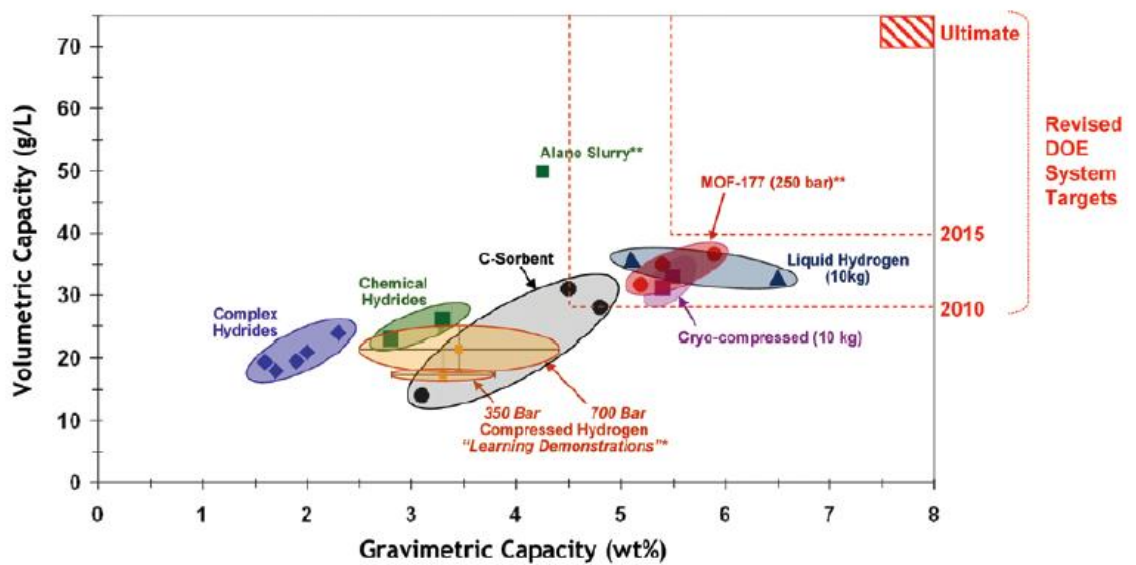


Figure 1-1 Status of hydrogen storage systems<sup>10</sup>.

For compressed gas and cryogenic tanks, volume and cost are the primary concerns. Cost and thermal management are issues for all material approaches. For complex chemical

storage materials, the cost and energy efficiency for off-board regeneration are key issues. Research is also needed on improving hydrogen discharge kinetics and simplifying the reactor required for discharging hydrogen on-board the vehicle (e.g. the volume, weight, and operation). For metal hydrides, weight, system volume and refueling time are the primary issues. Volumetric capacity, operating temperature and pressure are drawbacks for physical adsorbents that are inherently low density materials and have low hydrogen binding energies thus requiring cryogenic temperature. Finally, for all chemical materials approaches, transient performance and its control for hydrogen discharge is relatively unexplored from a “full” tank to the “nearly depleted” tank<sup>6</sup>.

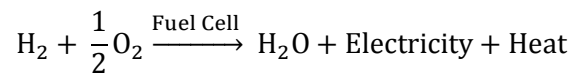
Magnesium hydride is considered as one of promising hydrogen storage materials due to its high capacity of 7.6 wt %, relatively low cost and light weight<sup>1, 12</sup>. However its slow kinetics and high desorption temperature of >300 °C limits its practical applications<sup>13-16</sup>. Many methods such as doping with catalyst, reducing crystallite and particle size have been developed to improve the hydrogen sorption properties. It is reported that the sorption kinetics of MgH<sub>2</sub> can be dramatically increased by ball milling with some transition metals, oxides and fluorides<sup>16, 17</sup>. Particularly, transition-metal compounds have attracted considerable interest as effective catalysts, due to high affinity of transition-metal cation toward hydrogen<sup>17, 18</sup>. For example, the small addition of Nb<sub>2</sub>O<sub>5</sub> significantly improves both the absorption and desorption kinetics of MgH<sub>2</sub><sup>19, 20</sup>. Comparative studies based on various transition-metal oxides emphasize that the appropriate chemical interaction between catalyst and host hydride is essential for realizing high catalytic activity, suggesting the functionality of contact anion in tailoring the activity of transition-metal cation<sup>11</sup>. Titanium-based compounds have been successfully used to improve sorption kinetics in several hydrogen storage systems, exhibiting a high affinity of Ti cation toward hydrogen even at moderate temperatures. For example, titanium halides are exceptionally effective in reducing the

kinetic barrier of dehydrogenation of alkaline alanates <sup>17, 21, 22</sup>. In addition, TiN is found to be very active in accelerating the amide/imide conversion as a promising catalyst for the Li-N-H system <sup>17</sup>. It has been also found that the temperature for hydrogen release from MgH<sub>2</sub> can be greatly reduced by doping it with Ti-containing agents e.g. TiF<sub>3</sub> and TiC <sup>16, 23</sup>. The interactions between the hydrides and the Ti-containing agents weaken the Mg-H bonds and thus facilitate the recombination of hydrogen atoms to the hydrogen molecules.

Following this brief introduction, Chapter 2 provides a thorough literature review on metal hydrides storage systems, and the hydrogen sorption properties of Mg-based storage materials, addressing the thermodynamic properties, kinetic limitations, and various modifications to the system. Chapter 3 describes the experimental facilities and the process of sample preparation. The results are studied in Chapter 4. Chapter 5 covers a general discussion of all the experimental findings. The conclusions are drawn in Chapter 6 with a future plan. References cited in each chapter are listed at the end of the thesis.

## CHAPTER 2 LITERATURE REVIEW

Hydrogen is the ideal fuel for the future since it significantly reduces the greenhouse gas emissions, reduces the global dependence on fossil fuels, for both internal combustion engines and proton exchange membrane fuel cells<sup>12</sup>. Hydrogen used in the fuel cell directly converts the chemical energy of hydrogen into water, electricity, and heat<sup>24</sup> as represented by



### 2.1 Hydrogen Storage Methods

Hydrogen molecule  $\text{H}_2$  can be found in various forms depending on the temperature and the pressure which are shown in the phase diagram Figure 2-1<sup>25</sup>. At low temperature, hydrogen is a solid with a density of  $70.6 \text{ kg/m}^3$  at  $-262 \text{ }^\circ\text{C}$  and hydrogen is a gas at higher temperatures with a density of  $0.09 \text{ kg/m}^3$  at  $0 \text{ }^\circ\text{C}$  within a pressure of 1 bar. A small zone starting at the triple point and ending at the critical point exhibits the liquid hydrogen with a density of  $70.8 \text{ kg/m}^3$  at  $-253 \text{ }^\circ\text{C}$ . At ambient temperature ( $25 \text{ }^\circ\text{C}$ ) hydrogen is a gas and can be described by a Van der Waals equation:

$$p(V) = \frac{n \cdot R \cdot T}{V - n \cdot b} - a \cdot \frac{n^2}{V^2}$$

Where  $p$  is the gas pressure,  $V$  the volume,  $T$  the absolute temperature,  $n$  the number of mols,  $R$  the gas constant  $8.314 \text{ J K}^{-1} \text{ mol}^{-1}$ ,  $a$  is the dipole interaction or repulsion constant  $2.476 \times 10^{-2} \text{ m}^6 \text{ Pa mol}^{-2}$  and  $b$  is the volume occupied by the hydrogen molecules itself  $2.661 \times 10^{-5} \text{ m}^3 \text{ mol}^{-1}$ <sup>26</sup>. The first criterion of hydrogen storage implies basically the reduction of the enormous volume of the hydrogen gas. One kilogram of hydrogen at ambient temperature and atmospheric pressure takes a volume of  $11 \text{ m}^3$ . In order to increase the hydrogen density in a storage system either work can be applied to compress hydrogen or the temperature has

to be decreased below the critical temperature or finally the repulsion has to be reduced by the interaction of hydrogen with an other material.

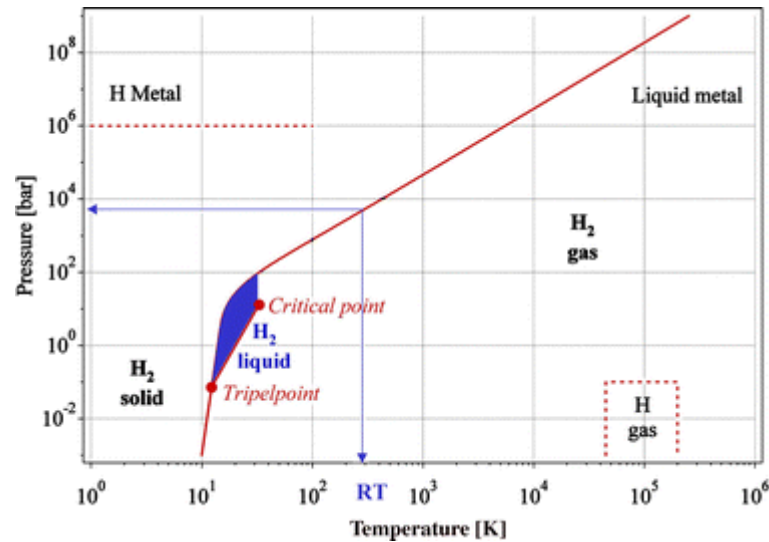


Figure 2-1 Primitive phase diagram for hydrogen. Liquid hydrogen only exists between the solidus line and the line from the triple point at 21.2K and the critical point at 32K

The second criterion for a hydrogen storage system is the reversibility of charging and discharging. Based on the two criteria, six methods of reversible hydrogen storage with a high volumetric and gravimetric density are known today, listed in Table 2-1<sup>2, 27, 28</sup>. Each of these options possesses attractive attributes for hydrogen storage. Available technologies permit directly to store hydrogen by modifying its physical state in gaseous or liquid form in pressurized or in cryogenic tanks. The traditional hydrogen-storage facilities are complicated because of its low boiling point  $-253\text{ }^{\circ}\text{C}$  and low density in the gaseous state  $0.08988\text{ g/L}$  at  $1\text{ atm}^2$ . Liquid hydrogen requires the addition of a refrigeration unit to maintain a cryogenic state, thus adding weight and energy costs, and a resultant 40 % loss in energy content<sup>2</sup>. High-pressure storage of hydrogen gas is limited by the weight of the storage canisters and the potential for developing leaks. Moreover, storage of hydrogen in liquid or gaseous form poses important safety problems for on-board transport applications. Designs involving the use of methane as a hydrogen source require the addition of a steam reformer to extract

hydrogen from the carbon which adds weight, additional space requirements, and the need for a device to sequester CO<sub>2</sub><sup>29</sup>.

Table 2-1 the six basic hydrogen storage methods and phenomena. The gravimetric density  $\rho_m$ , the volumetric density  $\rho_v$ , the working temperature T, and pressure p are listed. RT stands for room temperature (25 °C)<sup>2, 27, 28</sup>

Storage method	$\rho_m$ mass %	$\rho_v$ kg H <sub>2</sub> /m <sup>3</sup>	T °C	P bar	Phenomena and remarks
High pressure gas cylinders	13	<40	RT	80 0	Compressed gas in light weight composite cylinders (tensile strength of the material is 2000 MPa)
Liquid hydrogen in cryogenic tanks	Size dependent	70.8	-252	1	Liquid hydrogen, continuous loss of a few % per day of hydrogen at RT.
Physical adsorbents	~ 2	20	-80	10 0	Physisorption on materials, e.g. carbon with a very large specific surface area, fully reversible.
Adsorbed on interstitial sites in a host metal	~ 2	150	RT	1	Hydrogen (atomic H) intercalation in host metals, metallic hydrides working at r tater fully reversible
Complex chemical compounds	< 18	150	>10 0	1	Complex compounds ([AlH <sub>4</sub> ] <sup>-</sup> or [BH <sub>4</sub> ] <sup>-</sup> ), desorption at elevated temperature, adsorption at high pressures
Metals and complexes together with water	< 40	> 150	RT	1	Chemical oxidation of metals with water and liberation of hydrogen, not directly reversible.

The U.S. Department of Energy (DOE)<sup>10</sup> published a long-term vision for hydrogen-storage applications considering economic and environmental parameters. The predicted minimum hydrogen-storage capacity of 2010 target should be 6.5 wt% and 65 g/L hydrogen available, at the decomposition temperature between 60 and 120 °C for commercial viability ideally. It was also required low temperature of hydrogen desorption and low pressure of hydrogen absorption (a plateau pressure of the order of a few bars at room temperature) and nonthermal transformation between substrates and products of decomposition, as reported by Schulz<sup>30</sup>. Furthermore, the cost of a storage medium and its toxicity properties need to be carefully considered for the realization of the set goals.

Storage by absorption in chemical compounds or by adsorption on porous materials has definite advantages from the safety perspective such that some form of conversion or energy input is required to release the hydrogen for use. A great deal of effort has been made on solid forms of hydrogen storage systems, including metal hydrides, chemical complex hydrides, carbon nano structures and metallic alloy.

### 2.1.1 Physical adsorbents

Carbon materials such as high surface area activated carbons (AC), carbon nanotubes (SWNTs), carbon nanofibers and metal–organic frameworks (MOFs) have been proposed as storage media for hydrogen. The research on hydrogen storage in carbon materials was dominated by announcements of high storage capacities in carbon nanostructures. However, the experimental results on hydrogen storage in carbon nanomaterials scatter over several orders of magnitude. The hydrogen storage capacity for carbon materials is reported between 0.2 and 10 wt%<sup>31, 32</sup>. Considering the experimental results for metal hydrides, the storage capacities of which have been reported to vary only within a few percent due to stable structures and good reversibility. Why it is so difficult to determine the hydrogen storage capacity of carbon nanostructures? The reasons may be the limited quantity and purity of carbon nanotubes and different experimental conditions. A reliable characterization of carbon nanostructures and the determination of their purity are extremely difficult.

Recently, metal–organic frameworks have attracted great attention for hydrogen storage because they are amenable to being designed<sup>33-35</sup>, have extraordinary permanent porosity<sup>35, 36</sup>, and a large pore volume<sup>37, 38</sup>. A series of MOF-n materials with various structures were reported in 2000 by Yaghi and co-workers<sup>39</sup>. One member of the MOF-n family, MOF-5, has a zeolite-like framework in which inorganic  $[\text{Zn}_4\text{O}]^{6+}$  groups are joined to an octahedral array of  $[\text{O}_2\text{C}-\text{C}_6\text{H}_4-\text{CO}_2]_2$  (1,4-benzendicarboxylate, BDC) groups to form a robust and highly porous cubic framework of space group (Fm-3m) with  $a = 25.6690(3) \text{ \AA}$  and  $V =$

16,1913.2 (3) Å<sup>3</sup>. In their first paper, they reported that MOF-5 showed high hydrogen capacities, 4.5 wt% at 77K and 0.8 bar, and 1 wt% at room temperature and pressure of 20 bar<sup>40</sup>. In later research, this group observed that maximum uptakes hydrogen of MOF-5 can reach 1.32 wt% at 1 bar and 77K<sup>41</sup>. However Panella and Hirscher reported a hydrogen storage value of 1.6 wt% for MOF-5 at 77 K and pressures above 10 bar<sup>42</sup>. Nevertheless, the adsorption capacity of MOF-5 is very low at room temperature: less than 0.2 wt% at pressures up to 67 bar<sup>42</sup>. More recently, Panella et al. showed that the hydrogen uptake of MOF-5 can reach a saturation value of 5.1 wt% at 77 K and over 80 bar due to the synthesis of single-crystal MOF-5<sup>43</sup>. The results show that there are considerable differences in the hydrogen storage capacities of MOF-5 synthesized by different approaches and even by the same approach (Table 2-2)<sup>2</sup>.

Table 2-2 Adsorption Data for Metal–Organic Frameworks

Material	Wt % Hydrogen	Absorption condition	Raw materials	Surface Area (m <sup>2</sup> /g)	Reference
MOF-5	2.96	77 K, 1.45 MPa	Zn(NO <sub>3</sub> ) <sub>2</sub> · 6H <sub>2</sub> O H <sub>2</sub> BDC Dimethylformamide(DMF) Triethylamine(TEA) H <sub>2</sub> O <sub>2</sub>	611, BET	<sup>44</sup>
MOF-5	4.5 1	77 K, 0.8 bar 298K, 20 bar	Zinc (II) nitrate H <sub>2</sub> BDC DMF N,N'- H <sub>2</sub> O <sub>2</sub>	2 900, Langmuir	<sup>40</sup>
IRMOF	1.32	77 K, 1 bar	zinc oxide clusters benzene-1,4-dicarboxylate, naphthalene-2,6-dicarboxylate, 4,5,9,10-tetrahydropyrene-2,7-dicarboxylate, 2,3,5,6-tetramethylbenzene-1,4-dicarboxylate	3362, Langmuir	<sup>41</sup>
MOF-5	1.6	77 K, 10 bar	Zn(NO <sub>3</sub> ) <sub>2</sub> · γH <sub>2</sub> O BDC TEA DMF	1014, Langmuir	<sup>42</sup>

### 2.1.2 Metal hydrides

Hydrogen forms compounds with metals like Li, Na, Mg, Ti (Table 2-3), which are generally known as metal hydride. Many of these compounds, (MH<sub>n</sub>), show large deviations from ideal stoichiometry (n = 1, 2, 3) and can exist as multiphases systems. The lattice structure is that of a typical metal with hydrogen atoms on the interstitial sites; and for this reason they are also called interstitial hydrides. This type of structure is limited to the compositions MH, MH<sub>2</sub>, and MH<sub>3</sub>, with the hydrogen atoms fitting into octahedral or tetrahedral holes in the metal lattice, or a combination of the two. Especially interesting are the metallic hydrides of intermetallic compounds, in the simplest case the ternary system AB<sub>x</sub>H<sub>n</sub>, because the variation of the elements allows the properties of these hydrides to be tailored. Element A is usually a rare earth or an alkaline earth metal and tends to form a stable hydride. Element B is often a transition metal and forms only unstable hydrides. Some well defined ratios of B: A, where x = 1.5, 1, 2, 5, have been found to form hydrides with a hydrogen to metal ratio of up to two<sup>45</sup>.

Table 2-3 Volumetric and gravimetric hydrogen content in various materials <sup>45</sup>

Material	H-atoms per cm <sup>3</sup> ( $\times 10^{22}$ )	Wt % Hydrogen
H <sub>2</sub> gas, 200 bar (2850 psi)	0.99	100
H <sub>2</sub> liquid, 20 K (-253 °C)	4.2	100
H <sub>2</sub> solid, 2.4 K (-269 °C)	5.3	100
MgH <sub>2</sub>	6.5	7.6
Mg <sub>2</sub> NiH <sub>4</sub>	5.9	3.6
FeTiH <sub>1.95</sub>	6.0	1.89
LaNi <sub>5</sub> H <sub>6.7</sub>	5.5	1.37
ZrMn <sub>2</sub> H <sub>3.6</sub>	6.0	1.75
VH <sub>2</sub>	11.4	2.10

The reaction of hydrogen gas with a metal is called the absorption process and the hydrogen atoms contribute their electron to the band structure of the metal. At a small hydrogen to metal ratio (H/M < 0.1), the hydrogen is exothermically dissolved in the metal (solid-solution,  $\alpha$ -phase). The metal lattice expands proportional to the hydrogen concentration by

approximately 2-3 Å<sup>3</sup> per hydrogen atom<sup>5</sup>. At greater hydrogen concentrations in the host metal (H/M >0.1), a strong hydrogen-hydrogen interaction becomes important because of the lattice expansion, and the hydride phase (β-phase) nucleates and grows. The hydrogen concentration in the hydride phase is often found to be H/M = 1. The volume expansion between the co-existing α- and β-phase corresponds, in many cases, to 10-20% of the metal lattice. At the phase boundary, therefore, a large stress builds up and often leads to a decrepitation of brittle host metals such as intermetallic compounds. The thermodynamic aspects of hydride formation from gaseous hydrogen are described by pressure-composition-isotherms (P-C-I), shown in Figure 2-2. When solid solution and hydride phases coexist, there is a plateau in the isotherms, the length of which determines the amount of hydrogen stored. In the pure β-phase, the hydrogen pressure rises steeply with the concentration. The two phases region ends in a critical point, T<sub>c</sub>, above which the transition from the α- to β-phase is continuous. The equilibrium pressure, p<sub>eq</sub>, is related to the changes ΔH and ΔS in enthalpy and entropy, respectively, as a function of temperature by the Van't Hoff equation:

$$\ln \left( \frac{p_{eq}}{p_{eq}^0} \right) = \frac{\Delta H}{R} \cdot \frac{1}{T} - \frac{\Delta S}{R}$$

p<sub>eq</sub><sup>0</sup> is the equilibrium constant at absolute temperature T, and R is the universal gas constant (8.314 J/ mol/K).

As the entropy change corresponds mostly to the change from molecular hydrogen gas to dissolved solid hydrogen, it is approximately the standard entropy of hydrogen S<sub>0</sub> = 130 J K<sup>-1</sup> mol<sup>-1</sup> and is, therefore, ΔS<sub>f</sub> ≈ -130 J K<sup>-1</sup> mol<sup>-1</sup> H<sub>2</sub> for all metal-hydrogen systems. The enthalpy term characterizes the stability of the metal hydrogen bond. To reach an equilibrium pressure of 1 bar at 300 K, ΔH should amount to 39.2 kJ mol<sup>-1</sup> H<sub>2</sub>. The entropy of formation term for metal hydrides leads to a significant heat evolution ΔQ = T·ΔS (exothermal reaction) during hydrogen absorption. The same heat has to be provided to the

metal hydride to desorb the hydrogen (endothermal reaction). If the hydrogen desorbs below RT, the necessary heat has to be delivered from an external source, such as the combustion of hydrogen. For a stable hydride like  $\text{MgH}_2$ , the heat necessary for the desorption of hydrogen at 300 °C and 1 bar is about 25 % of the higher heating value of hydrogen.

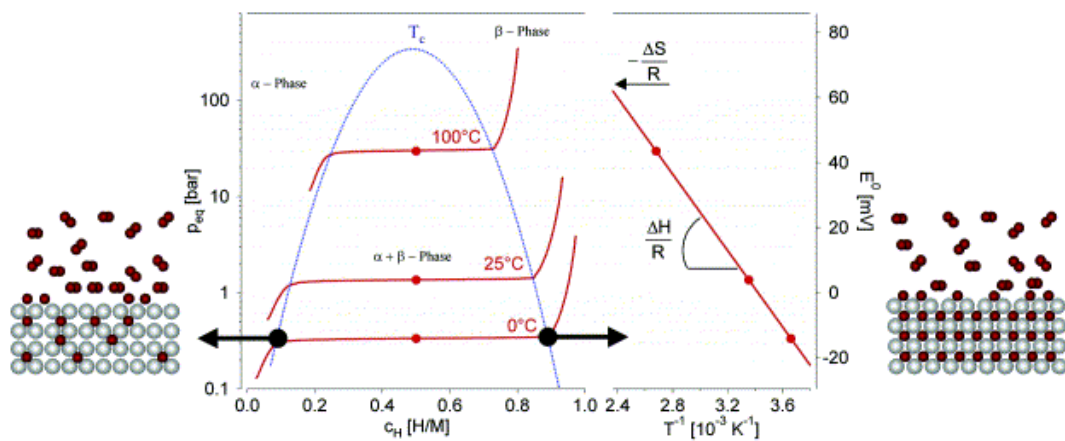


Figure 2-2 Pressure composition isotherms for hydrogen absorption in a typical intermetallic compound on the left hand side. The solid solution ( $\alpha$ -phase), the hydride phase ( $\beta$ -phase) and the region of the coexistence of the two phases are shown. The coexistence region is characterized by the flat plateau and ends at the critical temperature  $T_c$ . The construction of the Van't Hoff plot is shown on the right hand side. The slope of the line is equal to the enthalpy of formation divided by the gas constant and the intercept is equal to the entropy of formation divided by the gas constant.<sup>46</sup>

Metal hydrides, can absorb large amounts of hydrogen at a constant pressure, because of this phase transition, i.e. the pressure does not increase with the amount of hydrogen adsorbed. The characteristics of hydrogen absorption and desorption can be tailored by partial substitution of the constituent elements in the host lattice. Some metal hydrides adsorb and desorb hydrogen at ambient temperature and close to atmospheric pressure. Several families of intermetallic compounds listed in Table 2-4 are interesting for hydrogen storage<sup>28</sup>. They all consist of an element with a high affinity to hydrogen, element A, and a low affinity one, element B. The latter is often at least partially Ni, since it is an excellent catalyst for hydrogen dissociation.

Table 2-4 the most important families of hydride-forming intermetallic compounds.

Intermetallic compound	Prototype	Structure
<b>AB<sub>5</sub></b>	LaNi <sub>5</sub>	Haucke phase, hexagonal
<b>AB<sub>2</sub></b>	ZrV <sub>2</sub> , ZrMn <sub>2</sub> , TiMn <sub>2</sub>	Laves phase, hexagonal or cubic
<b>AB<sub>3</sub></b>	CeNi <sub>3</sub> , YFe <sub>3</sub>	Hexagonal
<b>A<sub>2</sub>B<sub>7</sub></b>	Y <sub>2</sub> Ni <sub>7</sub> , Th <sub>2</sub> Fe <sub>7</sub>	Hexagonal
<b>A<sub>6</sub>B<sub>23</sub></b>	Y <sub>6</sub> Fe <sub>23</sub>	Cubic
<b>AB</b>	TiFe, ZrNi	Cubic
<b>A<sub>2</sub>B</b>	Mg <sub>2</sub> Ni, Ti <sub>2</sub> Ni	Cubic

One of the most interesting features of metallic hydrides is the extremely high volumetric density of hydrogen atoms present in the host lattice. The highest volumetric hydrogen density reported to date is  $150 \text{ kg m}^{-3}$  in Mg<sub>2</sub>FeH<sub>6</sub> and Al(BH<sub>4</sub>)<sub>3</sub>. Both hydrides belong to the complex hydride family. However, all hydrides with hydrogen to metal ration of more than two are ionic or covalent compounds and belong to the complex hydrides group.

Metal hydrides are very effective in storing large amounts of hydrogen in a safe and compact way. All the reversible hydrides working around ambient temperature and atmospheric pressure consist of transition metals; therefore, the gravimetric hydrogen density is limited to less than 3 mass%. It remains a challenge to explore the properties of the lightweight metal hydrides.

### 2.1.3 Complex hydrides

Group I and II salts of [AlH<sub>4</sub>]<sup>-</sup>, [NH<sub>2</sub>]<sup>-</sup>, and [BH<sub>4</sub>]<sup>-</sup> (alanates, amide, and borohydride) have recently received considerable attention as potential hydrogen storage materials. All of these materials are currently referred to as “complex hydrides”, although only the alanates contain anionic metal complexes. These materials have high hydrogen gravimetric densities (Table 2-5) and are, in some cases, commercially available. Thus, a priori, they would seem to be viable candidates for application as practical, on-board hydrogen storage materials. Many of these “complex hydrides” have, in fact, been utilized in “one-pass” hydrogen storage systems in which hydrogen is evolved from the hydride upon contact with water. However,

the hydrolysis reactions are highly irreversible and could not serve as the basis for rechargeable hydrogen storage systems. All of these materials are also plagued by high kinetics barriers to dehydrogenation and/or rehydrogenation in the solid state. Traditionally, it was thought that it would be impossible to reduce the barrier heights to an extent that would give reaction rates that even approached those that would be required for vehicular applications. Thus, until recently, complex hydrides were not considered as candidates for application as rechargeable hydrogen carriers. This situation was changed by Bogdanović and Schwickardi. Their pioneering studies demonstrated that, upon doping with selected titanium compounds, the dehydrogenation of anionic aluminum hydrides could be kinetically enhanced and rendered reversible under moderate conditions in the solid state<sup>47</sup>. This breakthrough has led to a worldwide effort to develop doped alanates as practical hydrogen storage materials that was quickly expanded to include amides and borohydride.

Over the past decade, tremendous progress has been made toward the development of complex hydrides for potential use as an onboard hydrogen carrier. This approach to hydrogen storage, which was once thought to be “impossible”, has been brought to the threshold of commercial viability. Alanates are attractive because of the rapid kinetics of their dehydrogenation and rehydrogenation. Borohydrides have extremely high available hydrogen mass percents that meet the current, highly stringent U.S. DOE targets. Amides have reaction kinetics and hydrogen mass percents which both approach practical viability. However, all of the complex hydrides currently have practical limitations that must be overcome. Alanates have insufficient reversible capacity; Borohydrides suffer from unacceptably slow kinetics and also from undesirable evolution of diborane; and amides are plagued by capacity and kinetic limitations as well as undesirable evolution of ammonia. Additionally, the problem of thermal management on recharging is common to all complex hydrides. In view of the great progress that has been made, it can be anticipated that further

advances will be made toward the development of group I and II complex hydrides. Recently, the frontier of research in this area has been extended to the combinations of transition metal salts of these compounds. This new area of research may lead to the identification of materials which are free from the above-mentioned problems.

Table 2-5 Material Properties of Complex Hydrides<sup>48</sup>

Material	Density (g/mol)	Density (g/cm <sup>3</sup> )	Hydroge n (wt %)	Hydrogen (kg/m <sup>3</sup> )	$T_m^a$ (°C)	$\Delta H_f^\circ$ (kJ/mol)
LiAlH <sub>4</sub>	37.95	0.917	10.54		190 <sup>d</sup>	-119
NaAlH <sub>4</sub>	54.00	1.28	7.41		178	-113
KAlH <sub>4</sub>	70.11		5.71	53.2		
Mg(AlH <sub>4</sub> ) <sub>2</sub>	86.33		9.27	72.3		
Ca(AlH <sub>4</sub> ) <sub>2</sub>	102.10		7.84	70.4	>230 <sup>d</sup>	
LiNH <sub>2</sub>	22.96	1.18	8.78	103.6	372-400	-179.6
NaNH <sub>2</sub>	39.01	1.39	5.15	71.9	210	-123.8
KNH <sub>2</sub>	55.12	1.62	3.66	59.3	338	-128.9
Mg(NH <sub>2</sub> ) <sub>2</sub>	56.37	1.39	7.15	99.4	360	
Ca(NH <sub>2</sub> ) <sub>2</sub>	72.13	1.74	5.59	97.3		-383.4
LiBH <sub>4</sub>	21.78	0.66	18.36	122.5	268	-194
NaBH <sub>4</sub>	37.83	1.07	10.57	113.1	505	-191
KBH <sub>4</sub>	53.94	1.17	7.42	87.1	585	-229
Mg(BH <sub>4</sub> ) <sub>2</sub>	53.99	0.989	14.82	146.5	320 <sup>d</sup>	
Ca(BH <sub>4</sub> ) <sub>2</sub>	69.76		11.47		260 <sup>d</sup>	
Al(BH <sub>4</sub> ) <sub>3</sub>	71.51	0.7866	16.78	132	-64.5 <sup>d</sup> 44.5 <sup>b</sup>	

d and b represent decomposition and boiling temperatures, respectively.

#### 2.1.4 Storage via chemical reactions

Hydrogen can be generated by reacting metals and chemical compounds with water. The common experiment, seen in many chemistry classes, where a piece of Na floating on water produces hydrogen, demonstrates the process.

The Na transforms to NaOH in this reaction. The reaction is not directly reversible, but NaOH can be removed and reduced in a solar furnace back to metallic Na. Two Na atoms react with two H<sub>2</sub>O molecules and produce one hydrogen molecule. The hydrogen molecule produces a H<sub>2</sub>O molecule in combustion, which can be recycled to generate more hydrogen gas. However, the second H<sub>2</sub>O molecule necessary for the oxidation of the two Na atoms has to be added. Therefore, Na has a gravimetric hydrogen density of 3 mass%. The same

process carried out with Li leads to a gravimetric hydrogen density of 6.3 mass%. The major challenge of this storage method is reversibility and control of the thermal reduction process in order to produce the metal in a solar furnace. The process has been successfully demonstrated with Zn<sup>49</sup>.

The six different hydrogen storage methods (in Table 2-1) have been described here. Alongside well-established, high-pressure cylinders for laboratory applications and liquid hydrogen storage methods for air and space applications, metal hydrides, complex hydrides and some physical adsorbents offer a safe and efficient way to store hydrogen. Further research and technical development will lead to higher volumetric and gravimetric hydrogen density. The best materials known today show a volumetric storage density of 150 kg m<sup>-3</sup>, which can still be improved by approximately 50 % according to theoretical estimations.

## **2.2 Parameters for Hydrogen Storage in Hydrides**

In 2009, the on-board hydrogen storage system targets were revised to reflect knowledge gained in hydrogen fueled vehicles since original release of the targets by the US Department of Energy (DOE). In order to achieve system-level capacities of 1.8 kWh/kg system (5.5 wt.% hydrogen) and 1.3 kWh/L (0.040 kg hydrogen /L) and the ultimate targets of 2.5 kWh/kg system (7.5 wt.% hydrogen) and 2.3 kWh/L (0.070 kg hydrogen /L) in 2015, the gravimetric and volumetric capacities of the material respectively must clearly be higher than the system-level targets. In addition to high storage capacity, researcher must optimize other parameters like sorption temperature, hydrogen absorption/desorption kinetics, activation procedure, cycle-life, and so on in the materials development.

### **2.2.1 Mechanism of hydrogen absorption**

The absorption of hydrogen to form a metal hydride consists of several steps which may be described using the long-range attractive/short-range repulsive Lennard-Jones potential. As

the molecular hydrogen approaches the metallic surface, it encounters successive minima in the potential curve corresponding to molecular adsorption, atomic adsorption, and bulk absorption, as shown in Figure 2-3. Molecular hydrogen is first physisorbed on the surface of the metal. Physisorption is a process whereby a molecule adheres to a surface without the formation of a chemical bond, usually by van der Waals forces or electrostatic attraction with energy levels approximating those of condensation. Physisorption is a reversible process strongly dependent on both pressure and temperature.

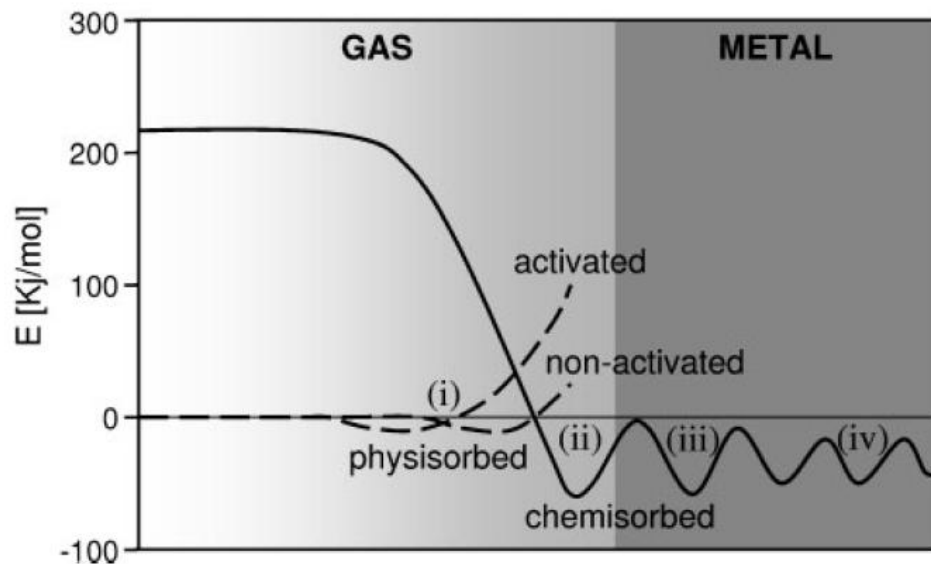


Figure 2-3 Potential energy curve for the Lennard-Jones potential for hydrogen binding to a metal indicating: (1) physisorption for both activated and non-activated processes; (2) dissociation and surface chemisorptions; (3) surface penetration and chemisorptions on subsurface sites; and (4) diffusion<sup>46</sup>.

The weak bonding usually prevents significant absorption at room temperature, which is why hydrogen storage on high surface area materials like carbon nanotubes or metal organic frameworks is achieved only at cryogenic temperatures<sup>50</sup>. Other models like the BET model are capable of describing multilayer adsorption<sup>51</sup>. The multiple layers are the result of the gas interacting with its condensate so that the binding energy approaches the condensation energy.

If the pressure and temperature are high enough, the adsorbed hydrogen is then dissociated at the surface and becomes chemisorbed. Chemisorptions are the chemical combination of hydrogen with the metal to form a new compound, which characteristically has a binding energy well above 50 kJ/mol. Both the host and adsorbate are chemically changed in the process and the initial compound is usually trapped irreversibly on the surface or within the bulk of the solid media. This involves an electron transfer between the metal and the hydrogen and may require thermal or catalytic activation due to the dissociation energy barrier.

After surface chemisorptions, the hydrogen atoms move to subsurface sites and rapidly diffuse through the material. This solution of H in the metal is referred to as the  $\alpha$  phase. As the hydrogen concentration in the  $\alpha$  phase increases, H-H interactions become important and a more stable phase nucleates ( $\beta$  phase), shown in Figure 2-4. Figure 2-4 (a) shows a few hydrogen atoms have dissociated and diffused into the low density  $\alpha$  phase. Then as the hydrogen concentration increases in the  $\alpha$  phase, Figure 2-4 (b), the interaction between hydrogen atoms through lattice deformations make nucleation of the high hydrogen density  $\beta$  phase energetically favorable. The  $\beta$  phase is characterized by a higher hydrogen density and often a different crystalline structure.<sup>52</sup> This phase transition is usually characterized by a crystalline structure change, a volume expansion, and a nucleation energy barrier associated with volume expansion and interface energy between the phases.

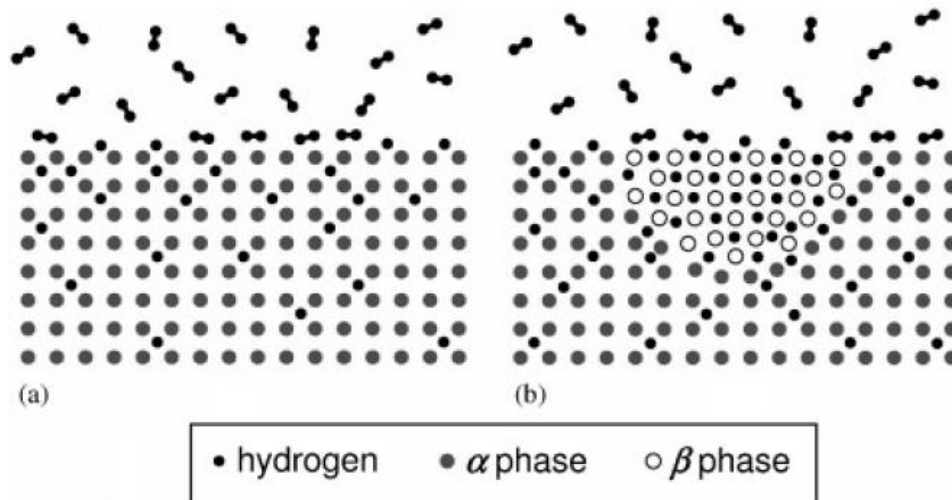


Figure 2-4 Simple representation of phase transition between the  $\alpha$  phase and the  $\beta$  phase<sup>52</sup>.

### 2.2.2 Capacity

There are two capacities commonly used in discussion of hydrogen storage. One is the volumetric capacities and the other is the gravimetric capacity. The volumetric capacity is defined as the amount of hydrogen adsorbed either in mass or in volume divided by the total volume occupied by the adsorbents and hydrogen, i.e.  $\text{kg/m}^3$ ,  $\text{H atm/m}^3$  or  $\text{H atm/f.u}$  that indicates the number of adsorbed H atoms per unit metal or alloy formula. The volumetric capacity is the more important in situations where space is limited, such as in a family car. Similarly, the gravimetric capacities are often defined as the weight percentage of the adsorbed gas to the total weight of the system, including the weight of the gas. Usually the gravimetric capacity is described as  $\text{kg/m}^3$  or wt. %.

The theoretical hydrogen storage capacity for the hydrides with known hydride formula can be calculated from the atomic weight percentage of hydrogen in one unit formula. In practice, hydrogen storage capacity can be give determined from the thermogravimetry (TG), which will be given more details in Section 3.3.

### 2.2.3 Hydrogen sorption kinetics and sorption temperature

Kinetic properties of a hydrogen storage material determine its application in the industrial world. Fast hydrogenation kinetics directly leads to the short refilling time for a hydrogen-powered car and fast dehydrogenation kinetics is essential for adequate performance<sup>52</sup>. Song<sup>53</sup> reviewed the kinetic studies of the hydriding and the dehydriding reactions of Mg. Numerous works are in disagreement regarding the rate-controlling steps for the hydriding or dehydriding of magnesium. However, there is no contradiction surrounding the points that the hydriding and dehydriding reactions of Mg are nucleation-controlled under certain conditions and progress by the mechanism of nucleation and growth, and that the hydriding rates of Mg are controlled by the diffusion of hydrogen through a growing Mg hydride layer. The hydriding and dehydriding kinetics of magnesium can be improved, therefore, by a treatment such as mechanical alloying<sup>13, 54-56</sup> which can facilitate nucleation by creating many defects on the surface and/or in the interior of Mg, or by the additive acting as active sites for nucleation, and shorten diffusion distances by reducing the effective particle size of Mg. Bobet et al.<sup>57</sup> reported that mechanical alloying in H<sub>2</sub> (reactive mechanical grinding) for a short amount of time, 2h, is an effective way to improve the hydrogen storage kinetics of both magnesium and Mg + 10% Co, Ni or Fe mixtures significantly. Huot<sup>58</sup> increased the hydrogenation rate of magnesium by milling under hydrogen with the addition of graphite. Imamura<sup>59</sup> improved the hydrogen sorption kinetics of magnesium by the mechanical milling of graphite and magnesium with organic additives. Oelerich<sup>60</sup>, Dehouche<sup>61</sup>, and Barkhordarian<sup>19</sup> increased the hydriding and dehydriding rates of magnesium via the planetary ball milling of magnesium hydride and a metal, a compound, or an oxide. Yavari<sup>62</sup> improved the hydrogen sorption kinetics of MgH<sub>2</sub> powders through the use of Fe nanoparticles generated by a reactive FeF<sub>3</sub> addition.

An example has been given in Figure 2-5. Even if the hydriding reaction is thermodynamically favorable due to a negative Gibbs free energy  $\Delta G$ , the reaction cannot take place at low pressure and temperature because of the energy barrier for adsorption  $E_{bar}^{ads}$  that must be overcome. The energy barrier  $E_{bar}^{des}$  is even larger for the desorption process, which explains the high release temperature for metal hydrides. The heat released is directly related to the difference in internal energy  $\Delta E$  between the initial and the hydride states. Destabilizing the hydrides will speed up the desorption kinetics and reduce the heat released, while the use of a catalyst can help both the hydrogenation and dehydrogenation kinetics<sup>52</sup>.

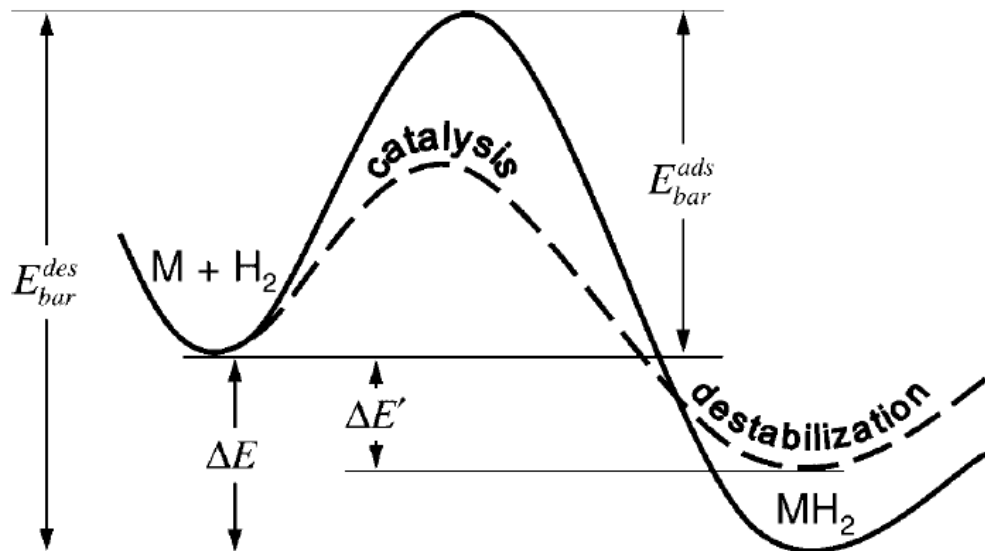


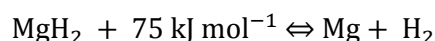
Figure 2-5 An example of an energy barrier for hydrogenation and dehydrogenation<sup>52</sup>.

Another important fact which has an effect on the hydrogenation/dehydrogenation kinetics is the metal surface. All hydrides except palladium have great affinity for oxygen than for hydrogen and they are normally coated with an oxidizing film that forbids the attack by the gaseous reactants at some points. Therefore, the oxide surface has to be removed or disrupted before the hydride formation. Heat treatment or cycling are mainly used on most metals to remove the oxide film<sup>63</sup>.

There are several methods for calculating kinetic parameters which depend not only on the experimental conditions but also on the mathematical treatment of the data. In this work, TG and differential thermogravimetry (DTG) measurements are used for the kinetics of hydrogen sorption of the materials, using Firedman techniques which allow us to calculate every point in a TG curve and a DTG curve, and the variations with temperature are discussed<sup>64</sup>. The dehydrogenation kinetics from TG-DTG has been described in Section 3.3. Kinetic curves also measure the content of adsorbed/desorbed hydrogen versus time at one or various constant pressures and temperatures. This curve also illustrates temperature dependence of both the hydrogenation and dehydrogenation reactions.

#### 2.2.4 Cycle-life and stability

An ideal hydrogen storage system should have a good cyclability, meaning that the system should maintain its physical and chemical properties through multiple absorption/desorption cycles. In the case of MgH<sub>2</sub>-Mg system, the desired reversible reaction is:



However, some loss in the hydrogen storage capacity of MgH<sub>2</sub>/Mg could happen during cycling due to low kinetics or impurities. Dehouche<sup>65</sup> reported the presence of magnesium oxide is responsible for the degradation of the hydriding and dehydriding properties of the MgH<sub>2</sub>/Mg after 1000 cycles. The MgO forms a barrier at the hydrogen diffusion stage, preventing the hydrogen from penetrating into the nanoparticle interior. Fan et al.<sup>66</sup> investigated the MgH<sub>2</sub>+10 wt.% TiC composite has good cycle stability, its hydrogen capacity only decreases 3.3% of hydrogen of the 1st run after 10 de/hydrogenation cycles.

### 2.3 Mg for Hydrogen Storage

Mg has shown promise for on-board hydrogen storage especially for vehicular application due its high hydrogen content 7.6 wt % and volumetric density about twice to that of liquid

hydrogen. Metallic magnesium is fairly accessible and a low cost material. Besides, the Mg based hydrides possess good quality functional properties, such as heat resistance, vibration adsorbing, reversibility and recyclability<sup>2</sup>. Magnesium hydride has the highest energy density (9 MJ / kg Mg) of all reversible hydrides applicable for hydrogen storage. Magnesium hydride differs from other metal hydrides according to the type of M-H bonds and crystal structure and properties and is similar to ionic hydrides of alkali and alkaline earth metals. MgH<sub>2</sub> is a stoichiometric compound with H/Mg atomic ration of  $0.99 \pm 0.01$ <sup>67</sup>. The equilibrium modification of MgH<sub>2</sub> under normal conditions,  $\alpha$ -MgH<sub>2</sub> has a tetragonal crystal structure of the rutile type<sup>68-70</sup>. Under high pressure  $\alpha$ -MgH<sub>2</sub> undergoes polymorphic transformations to form two modifications:  $\gamma$  – MgH<sub>2</sub> and  $\beta$  – MgH<sub>2</sub>, with an orthorhombic structure and a hexagonal structure, respectively<sup>71-73</sup>.

### 2.3.1 Properties of Mg/MgH<sub>2</sub>

Mg is the most practical option for hydrogen storage. Mg as a storage material meets two important storage criteria:

- 1) It can store large quantities of hydrogen, more than any other metal hydrides system.
- 2) It is relatively inexpensive. So it offers potential for storage of hydrogen for automobile or on-board applications.<sup>2, 74-76</sup>

### 2.3.2 Limitation of MgH<sub>2</sub> for practical application

Although Mg fulfills many commandments required for practical applications but still it cannot be used onboard. The main reason is that the reaction for hydrogenation/dehydrogenation is very slow and occurs only at very high temperatures. In practice, both absorption and desorption of hydrogen require a temperature of at least 350–400 °C and even then only occur over a time scale of hours<sup>77</sup>. The pressure of hydrogen gas in equilibrium with magnesium hydride is low (1bar at about 280 °C) and therefore

thermodynamically the hydride should form readily at room temperature. However, this never occurs in practice because of kinetic limitations. There are several factors that significantly reduce the rate of hydrogenation. One of them is the oxidation of magnesium surface and/or formation of magnesium hydroxide. Magnesium oxide forms easily on Mg surface exposed to air. Usually oxide layers on the metal surface are not transparent to hydrogen molecules so that MgO layer prevents hydrogen molecules from penetrating into the material<sup>78</sup>. Hence to initiate hydrogen absorption, the oxide layer should be broken down by activation process. The activation may consist in the cyclic heating and cooling in a vacuum or hydrogen atmosphere. But even after such an activation process, magnesium could form hydride completely after several hours at 400 °C<sup>78</sup>.

Another reason for the slow hydrogenation rate of magnesium (even after activation) is low dissociation rate of hydrogen molecules on the metal surface. A clean surface of pure magnesium needs a very high energy for dissociation<sup>77</sup>. In addition the diffusion of dissociated hydrogen atoms within metal hydride is very difficult. The growth rate of MgH<sub>2</sub> phase depends on the hydrogen pressure since, as the pressure increases, the thermodynamic driving force for the reaction increases. However, if the initial hydrogenation process is sufficiently rapid, a surface magnesium hydride layer that blocks the hydrogen penetration is formed<sup>79</sup>, the surface diffusion becomes an important and significant factor for hydrogenation. For pressures higher than about 30 bars, the absorption rate is again reduced<sup>80</sup>. This effect occurs when initial hydrogenation is relatively fast and leads to the formation of a “surface shell” of magnesium hydride which blocks further hydrogen uptake. At this point, hydrogenation is limited by the growth of the hydride. Although in general, growth has been found to be faster than nucleation<sup>80</sup>, growth limitations are usually responsible for reducing the final hydrogen capacity. Studies on hydrogenation kinetics showed that growth is controlled by diffusion of hydrogen atoms, which is very slow

throughout magnesium hydride<sup>81</sup>. Further experiments indicated that the growth is controlled by a slow migration of the interface between the hydride and magnesium<sup>82</sup>, in particular by hydrogen diffusion along the hydride–metal interface and not throughout the hydride layer<sup>80</sup>. In any case, hydrogenation of magnesium is normally almost impossible to complete, even at very high temperatures and pressures. It has also been observed that hydrogen uptake declines when the hydride nuclei start to coalesce on the magnesium surface to form a compact hydride layer<sup>83</sup> and that the hydrogenation reaction diminishes completely when the hydride layer exceeds 30–50  $\mu\text{m}$ . For kinetic reasons, the remaining magnesium cannot be further hydrogenated<sup>80</sup>.

### **2.3.3 Approaches to improve sorption properties of Magnesium Hydride**

Mg based systems can be modified to improve the sorption characteristics. Many efforts have been made to reduce desorption temperatures and to fasten the re/dehydrogenation reactions. The main approaches are listed as following:

- 1) Improving surface and kinetic properties by ball milling
- 2) Alloying with other transition metal and their oxides
- 3) Catalysis
- 4) Formation of thin film and nano-structured materials

Hydrogen absorption/desorption parameters for various Mg based Materials are summarized in Table 2-6.

Table 2-6 Hydrogen sorption properties of Mg based hydrides

Material	Method of preparation	Temperature (°C)	Pressure Conditions(bar)	Kinetics (min)	Max. Hydrogen (wt %)	Ref.
Mg- 20 wt%Ni–Y	Reactive Ball milling	T <sub>abs</sub> :200 T <sub>des</sub> :300	P <sub>abs</sub> :30 P <sub>des</sub> :1	t <sub>abs</sub> :5 t <sub>des</sub> :15	5.59	84
Mg-Ti <sub>0.28</sub> Cr <sub>0.50</sub> V <sub>0.22</sub>	Reactive Ball milling	T <sub>abs</sub> :275	P <sub>abs</sub> :30	t <sub>abs</sub> :10	4.0	85
Sn / MgH <sub>2</sub>	Ball milling	T <sub>des</sub> :300			3.4	86
Mg <sub>2</sub> NiH <sub>4</sub>	Hydriding combustion synthesis	T <sub>abs</sub> :330C	P <sub>abs</sub> :18	t <sub>abs</sub> :<8 (for 90%)	3.4	87
MgH <sub>2</sub> -17%Nb <sub>2</sub> O <sub>5</sub>	Ball milling	T <sub>abs</sub> :274 T <sub>des</sub> :274	P <sub>abs</sub> :10 P <sub>des</sub> :0.001	t <sub>abs</sub> :2 t <sub>des</sub> :3	7.0	88
Mg-10%Ni	Melting, Casting, Ball milling	T <sub>abs</sub> :300 T <sub>des</sub> :350			4.6	89, 90
Mg <sub>2</sub> Ni <sub>0.9</sub> Co <sub>0.1</sub>	Hydrogen Plasma Metal reaction & ultrasonic homogenizer	T <sub>abs</sub> :300 T <sub>des</sub> :300	P <sub>abs</sub> :40 P <sub>des</sub> :0.001	t <sub>abs</sub> :2 t <sub>des</sub> :4	2.66	90
MgH <sub>2</sub> / C (graphite, CNT, carbon black)	Reactive Ball milling	T <sub>abs</sub> :300 T <sub>des</sub> :300	P <sub>abs</sub> :12	t <sub>abs</sub> :20	6.2	91
Mg–Mm–Ni alloy	Equal channel angular pressing	T <sub>abs</sub> :300 T <sub>des</sub> :300	P <sub>abs</sub> :15 P <sub>des</sub> :1		5.4	92

Continued Table 2-6

MgH <sub>2</sub> -4 mol% TiF <sub>3</sub>	Reactive ball milling	T <sub>abs</sub> :300 T <sub>des</sub> :300	P <sub>abs</sub> :20 P <sub>des</sub> :0.1	t <sub>abs</sub> :<1 t <sub>des</sub> :10	5.0	93
Mg-10 wt%Ni-5 wt%Fe-5 wt%Ti	Reactive ball milling	T <sub>abs</sub> :300 T <sub>des</sub> :300	P <sub>abs</sub> :12 P <sub>des</sub> :1	t <sub>abs</sub> :10 t <sub>des</sub> :60	6.72	94
Mg-10 wt% Cr <sub>2</sub> O <sub>3</sub>	Ball milling	T <sub>abs</sub> :300 T <sub>des</sub> :300	P <sub>abs</sub> :10 P <sub>des</sub> :1	t <sub>abs</sub> :3 t <sub>des</sub> :5	6.0	95
Mg-20 wt% CNM	Ball milling	T <sub>abs</sub> :180	P <sub>abs</sub> :20	t <sub>abs</sub> :80	5.0	96
Mg-2 mol% NbF <sub>5</sub>	Reactive ball milling	T <sub>abs</sub> :300 T <sub>des</sub> :300	P <sub>abs</sub> :20 P <sub>des</sub> :<10 Pa	t <sub>abs</sub> :60 t <sub>des</sub> :60	6.0	97
Mg-20 wt%Ni-1 wt%TiO <sub>2</sub>	Reactive ball milling	T <sub>abs</sub> :180 T <sub>des</sub> :370	P <sub>abs</sub> :40 P <sub>des</sub> :1	t <sub>abs</sub> :3 t <sub>des</sub> :5	5.32	98
MgH <sub>2</sub> -1mol%La <sub>2</sub> O <sub>3</sub>	Ball milling	T <sub>abs</sub> :303 T <sub>des</sub> :303			6.0	99
MgH <sub>2</sub> -5 wt%LaNi <sub>5</sub>	Reactive ball milling	T <sub>abs</sub> :285 T <sub>des</sub> :285	P <sub>abs</sub> :20	t <sub>abs</sub> :2 t <sub>des</sub> :100	6.0	100
MgH <sub>2</sub> -35 wt%LaNi <sub>5</sub>	Reactive ball milling	T <sub>abs</sub> :285 T <sub>des</sub> :285	P <sub>abs</sub> :20	t <sub>abs</sub> :10 t <sub>des</sub> :15	4.0	100
Mg-23.5 wt%Ni-10 wt%La	Gravity casting	T <sub>abs</sub> :300 T <sub>des</sub> :350	P <sub>abs</sub> :11	t <sub>abs</sub> :30 t <sub>des</sub> :15	4.96	101
MgH <sub>2</sub> + 10 wt%Zr-Ni alloy	Ball milling	T <sub>abs</sub> :304, 324	P <sub>abs</sub> :20 P <sub>des</sub> :0.25	t <sub>abs</sub> :100s t <sub>des</sub> :300s	5.4	102
Mg + 30 wt% LaNi <sub>5</sub>	Hydriding combustion synthesis followed by mechanical milling	T <sub>des</sub> :197	P <sub>abs</sub> :0.003	t <sub>abs</sub> :50s	3.8	103

Continued Table 2-6

MgH <sub>2</sub> + 1 mol% Cr <sub>2</sub> O <sub>3</sub> + 0.2 mol% Nb <sub>2</sub> O <sub>5</sub>	Mechanical milling	T <sub>abs</sub> :300		t <sub>abs</sub> :5 t <sub>des</sub> :20	6.0	104
Mg + WO <sub>3</sub> Mg + H <sub>0.23</sub> WO <sub>3</sub>	Ball milling	T <sub>abs</sub> :300 T <sub>des</sub> :330	P <sub>abs</sub> :0.01 P <sub>des</sub> :0.0003			105
Mg <sub>1.9</sub> Nd <sub>0.1</sub> Ni	Vacuum induction melting	T <sub>abs</sub> :300 T <sub>des</sub> :300	P <sub>abs</sub> :0.00135 P <sub>des</sub> :0.0011		3.35	106
Mg + 5 wt%LaMg <sub>2</sub> Ni	Ball milling	T <sub>abs</sub> :180 T <sub>des</sub> :300	P <sub>abs</sub> :0.003 P <sub>des</sub> :0.0001	t <sub>abs</sub> :100 t <sub>des</sub> :30	4.4	99
MgH <sub>2</sub> + Cr <sub>2</sub> O <sub>3</sub>	Ball Milling	T <sub>abs</sub> :300 T <sub>des</sub> :300	P <sub>abs</sub> :0.003 P <sub>des</sub> :0.0001	t <sub>abs</sub> :20 t <sub>des</sub> :30	6.3	95
Mg+ TiF <sub>3</sub>	Ball milling	T <sub>abs</sub> :150 T <sub>des</sub> :320	P <sub>abs</sub> :10 P <sub>des</sub> :1	t <sub>abs</sub> :100 t <sub>des</sub> :0.5	3.8	107
Mg + TiC	Ball milling	T <sub>abs</sub> :300 T <sub>des</sub> :199	P <sub>abs</sub> :10	t <sub>abs</sub> :20 t <sub>des</sub> :30	6.2	16
MgH <sub>2</sub> +5wt%SiC	Ball milling	T <sub>abs</sub> :350 T <sub>des</sub> :350	P <sub>abs</sub> :30 P <sub>des</sub> :0.1	t <sub>abs</sub> :0.5 t <sub>des</sub> :6.7	6.3	15
MgH <sub>2</sub> + 0.1 TiH <sub>2</sub>	Ball milling	T <sub>abs</sub> :300 T <sub>des</sub> :240	P <sub>abs</sub> :20 P <sub>des</sub> :0.1	t <sub>abs</sub> :240 t <sub>des</sub> :20	4	108

## 2.4 Improvement of Kinetics by Milling

It has been found that the milling of  $\text{MgH}_2$  instead of pure Mg produces a nanocrystalline powder with high surface area beneficial for the hydrogen sorption properties<sup>30</sup>. The surface of pure Mg is important for hydrogen kinetics. Diffusion is not the limiting step initially, but after a partial formation of  $\text{MgH}_2$  surface it becomes important as the diffusion coefficient in  $\text{MgH}_2$  is much smaller than that in Mg<sup>81, 109, 110</sup>. It has been reported that after the formation of certain amount of  $\text{MgH}_2$  the hydrogenation rate decreases with increase of hydride layer thickness and finally become zero after a critical thickness<sup>111</sup>.

There are different types of high-energy ball mills which are used for the engineering of  $\text{MgH}_2$  in its nanocrystalline form in combination with different additives. These mills differ in their milling energies, milling modes and uniformity of milling which have strong influence on end milling product, shown in Figure 2-6. Marek<sup>95</sup> have found that the high-energy (ball) milling greatly improves the hydrogen sorption kinetics of  $\text{MgH}_2$ . There is no significant difference in the hydriding/dehydriding properties between  $\text{MgH}_2$  powders milled in different commonly used mills.

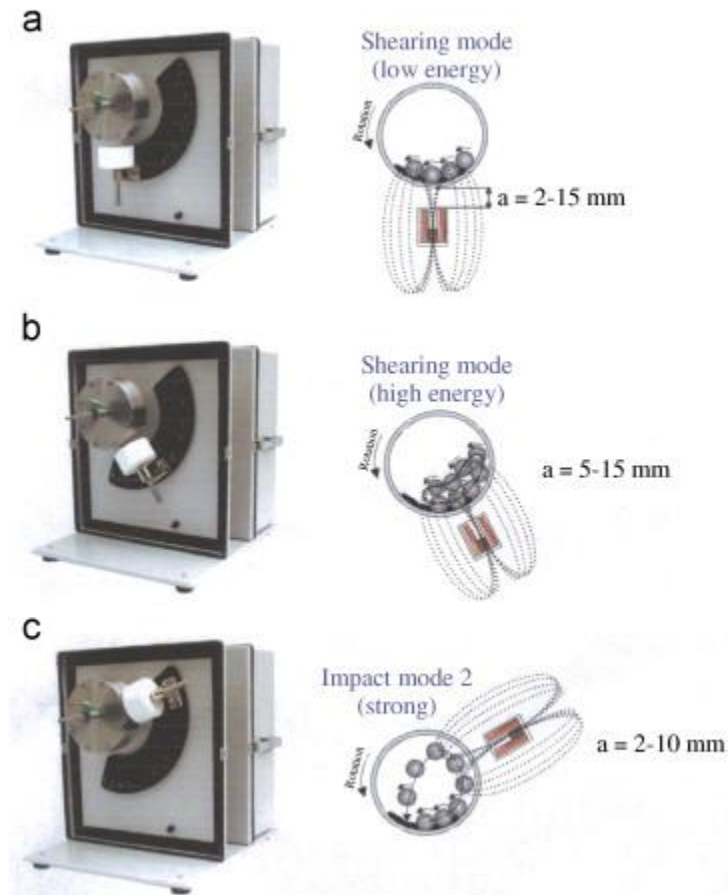


Figure 2-6 Different controlled milling modes available in the Uni-ball: (a) low-energy shearing, (b) high-energy shearing and (c) impact.

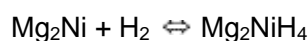
The mechanical/ball milling has shown a path to overcome this problem which relies on mechanical impact and friction to refine and alloy powder materials. Mechanical alloying can lead to several changes by the introduction of structural defects, phase change, and/or crystallinity<sup>112</sup>. Depending on the ball milling conditions, the onset temperature of  $\text{MgH}_2$  desorption can be decreased as large as  $100$  °C<sup>113</sup>. It has been found that with the decrease in crystal grain size, the desorption energy decreases drastically, reducing the desorption temperature up to  $200$  °C<sup>114</sup>. Another approach has been adopted in the form of milling under hydrogen atmosphere which provides an easy way to diffuse hydrogen into the material<sup>115</sup>. The results indicated that the pulverization and deformation processes occurring during high energy ball milling play a major role in the hydriding reaction. So it is

concluded that nano-structured materials can provide much better results for storing high a content of hydrogen with fast kinetics<sup>116</sup>. However, the preparation of such small particles by ball milling at large scale is a major challenge<sup>5</sup>. The method is based on infiltration of nanoporous carbon with molten magnesium. The size of thus prepared Mg crystallites has been reported from 2-5 nm to less than 2 nm. Another alternative for ball milling to modify the microstructure of the material is equal-channel angular pressing technique<sup>117</sup>. The microstructure refinement and increase in the density of the crystal lattice defects caused by equal channel angular pressing increase hydrogen desorption pressure, change the slope of the pressure plateau in pressure-composition isotherms, decrease the pressure hysteresis, and accelerate the hydrogen desorption kinetics<sup>118</sup>. Even though on the basis of present knowledge it is doubtful that such a procedure could be applied to a scale greater than laboratory.

## 2.5 Alloying with other Elements and Catalyst

### 2.5.1 Alloying with other elements

This method has also shown a way to reduce the desorption temperature and to remove other thermodynamic constraints. Mg<sub>2</sub>Ni is the very first and most popular alloy prepared in this category<sup>119</sup>. Since then Mg<sub>2</sub>Ni and its multiphase alloys have been studied intensively<sup>119-121</sup>. Mg<sub>2</sub>Ni reacts with hydrogen as per the following reaction at 470 – 500 K<sup>119</sup>:



The standard enthalpy of this reaction was found to be 65 kJmol<sup>-1</sup>H<sub>2</sub> which is less than that of pure MgH<sub>2</sub> (78 kJmol<sup>-1</sup>H<sub>2</sub>)<sup>122</sup>. Amorphous and nano-crystalline MgNiRe based alloys were also prepared for the improvement in hydrogen storage properties<sup>123-125</sup>. Recently Ren<sup>125</sup> has reported the improvement in the hydrogenation and electrochemical performance of Mg<sub>2</sub>Ni type alloy by introducing a fraction of La in place of Mg. It is found that the

hydrogen absorption and desorption capacities and kinetics of the as-cast alloys clearly rise with increasing La content. For La content  $x = 2$ , the as-quenched alloy displays an optimal hydrogen desorption kinetics at 200 °C. Actually this alloying could be done on the basis of nature of heat of mixing<sup>76</sup>. First route is to use the elements which exhibit negative heat of mixing with Mg and thus forms stable Mg compounds; Mg<sub>2</sub>Ni is a strong example of this case, and Mg<sub>2</sub>Si, Mg<sub>2</sub>Ca are other good examples. Mg<sub>2</sub>Si is important for having  $-79 \text{ kJmol}^{-1}$  enthalpy of formation but having densely packed crystal structure interaction is not possible at moderate conditions and hence attempts were made to modify the crystal structure by doping it with other elements such as Li, C, Al, Ca, Co, Ni & Cu. The second category involved the systems having positive heat of mixing e.g. Mg<sub>2</sub>FeH<sub>6</sub> materials which has highest volumetric capacity of hydrogen i.e. 150 Kg/m<sup>3</sup>,<sup>27, 126</sup> but as Mg and Fe do not form any intermetallic compound, the hydride phase is more difficult to synthesize. However, hydrogen can act as binding component to form Mg<sub>2</sub>FeH<sub>6</sub><sup>127</sup>. Another example of this family is Mg–Ti alloy which was synthesized by using a high pressure anvil cell by the reaction of MgH<sub>2</sub> and TiH<sub>1.9</sub> at 8GPa and 873 K<sup>27, 128</sup>. Recently, an Mg–Al alloy has attracted worldwide attention as an alternative for hydrogen storage applications<sup>129</sup>. Aluminum is considered to destabilize MgH<sub>2</sub> and forms Mg/Al alloys after dehydrogenation<sup>129-131</sup>. Recently, Grivello had studied a series of this kind of alloy Mg<sub>x</sub>Al<sub>100-x</sub><sup>130, 131</sup>. It was found that for the two process  $x = 70$  compound, the reversible hydrogenation is accomplished in three transformation steps. At first, only Mg reacts and forms MgH<sub>2</sub> then the  $\gamma$ -Mg<sub>17</sub>Al<sub>12</sub> phase is decomposed into the Mg-poor  $\beta$ -Mg<sub>2</sub>Al<sub>3</sub> phase. Finally, the Mg hydride phase is fully completed for the resulting Mg<sub>2</sub>Al<sub>3</sub>. These reactions are reversible.

### 2.5.2 Catalysis

The use of catalysts has been proved an important pathway to enhance surface kinetics. Firstly several catalysts were used such as transition metals<sup>20, 132-134</sup>, metal oxides,

intermetallic compounds that adsorb hydrogen in milder conditions<sup>19, 135</sup> and carbon materials<sup>136-138</sup>. It has been investigated the catalytic effects of five 3d elements Ti, V, Mn, Fe & Ni on the reaction kinetics of Mg hydride by the rapid desorption at low temperature for MgH<sub>2</sub>-V followed by MgH<sub>2</sub>-Ti, MgH<sub>2</sub>-Fe, MgH<sub>2</sub>-Ni & MgH<sub>2</sub>-Mn<sup>18, 139</sup>. Among the different oxides i.e. Nb<sub>2</sub>O<sub>5</sub>, TiO<sub>2</sub>, V<sub>2</sub>O<sub>5</sub>, Cr<sub>2</sub>O<sub>3</sub>, Mn<sub>2</sub>O<sub>3</sub>, Fe<sub>3</sub>O<sub>4</sub>, CuO, SiC; Nb<sub>2</sub>O<sub>5</sub> found to have better improved kinetics in comparison to the other oxides<sup>88, 135, 140</sup>. Bhat et al.<sup>141</sup> reported that high specific surface area nanocrystalline Nb<sub>2</sub>O<sub>5</sub> induces fastest kinetics than does commonly used Nb<sub>2</sub>O<sub>5</sub>. A further improvement in the sorption properties of Nb<sub>2</sub>O<sub>5</sub> doped MgH<sub>2</sub> was found when a small amount of Cr<sub>2</sub>O<sub>3</sub> was added by Patah et al<sup>104</sup>. They reported drastic reduction in the activation energy of Cr<sub>2</sub>O<sub>3</sub> and Nb<sub>2</sub>O<sub>5</sub> doped MgH<sub>2</sub> upto 136 kJmol<sup>-1</sup> in comparison to 197 kJmol<sup>-1</sup> and 206 kJmol<sup>-1</sup> for 1 mol% doped MgH<sub>2</sub> and pure MgH<sub>2</sub>, respectively. Recently, the use of a new catalyst SiC has been reported to improve the hydrogenation properties of MgH<sub>2</sub> by Ranjbar et al<sup>15, 142</sup>. They found improved hydrogen absorption/desorption kinetics by adding SiC and capacity of MgH<sub>2</sub> is also found to be increased by increasing the surface area and defect concentration. An additional improvement was achieved by adding Ni to the MgH<sub>2</sub>/SiC composite because of catalytic effects of Ni. Although the explanation for the action of these catalyst is still not clear but it is suggested that these catalysts are responsible for modification of Mg surface on mechano-chemical treatment destruction of MgO layer, formation of active nucleation centers and partial reduction of the oxides to form metal cluster<sup>74</sup>.

The second route to lower reaction enthalpy of MgH<sub>2</sub> is the formation of composite with other hydrogen sorbing alloys such as LaNi<sub>5</sub>, FeTi, ZrCr<sub>2</sub> based IMCs<sup>100, 102, 143-145</sup>. LaNi<sub>5</sub> has a significant effect on reducing the working temperature and to increase the reaction kinetics. It was found that Mg- LaNi<sub>5</sub> based composites can desorb significant amounts of hydrogen at 245 °C with reasonable reaction rate<sup>100</sup>. Deposition processes could occur even at a low

temperature of 185 °C with an extremely slow desorption rate. Another processing material for making compounds with Mg is Zr based alloys. ZrNi is one of the promising materials to prepare composite with MgH<sub>2</sub>. MgH<sub>2</sub>+10 wt %<sup>102</sup> composite could adsorb about 5 wt% in less than 3 mins and desorb the same amount in 7 mins at 300 °C. FeTi has also been reported as an exciting material to improve the kinetics of MgH<sub>2</sub>. The maximum capacity was found to be 5.8 wt% at 300 °C and 5.12 wt% at 290 °C for Mg-5 wt% FeTi<sup>144</sup>. The surface modification of MgH<sub>2</sub> with nanosized Ti<sub>0.4</sub>Cr<sub>0.15</sub>Mn<sub>0.15</sub>V<sub>0.3</sub> alloy could also enhance the kinetics of MgH<sub>2</sub>. It desorbed 5.7 wt% hydrogen in 3 mins at 290 °C and adsorbed more than 90% of its capacity within 100 min even below 100 °C<sup>145</sup>.

The third route is the combination of MgH<sub>2</sub> with other light hydrides<sup>126,146</sup>. This category termed as reactive hydride composite as the composite compounds taking path in reaction with each other upon desorption e.g. of this category is MgH<sub>2</sub>+ LiBH<sub>4</sub>, MgH<sub>2</sub>+NaBH<sub>4</sub>, MgH<sub>2</sub>+Ca(BH<sub>4</sub>)<sub>2</sub> which form MgB<sub>2</sub> during desorption and can be reversibly hydrogenated.

The most recent effort is to make the composite of MgH<sub>2</sub> with a carbon based material<sup>91, 96, 136, 147-149</sup>. Due to their high specific surface area and unique adsorbing properties, nano structured carbon has been shown to have a high catalytic activity<sup>150</sup>. Imamura<sup>59, 136</sup> in a series of publications confirmed that the magnesium/graphite (Mg/C) composite formed by mechanical milling with the organic additives not only show improved hydriding-dehydriding properties of magnesium but also additional hydrogen uptake other than that due to the magnesium component. Several reasons have been given by them for this prominent effect<sup>151</sup>: (1) Segregation of carbon at grain boundary thus resulting the increment in hydrogen diffusion along the boundaries. (2) The dispersive feature of carbon assists to obtain Mg particles that shorten the diffusion path.

## 2.6 Aims and Objectives

MgH<sub>2</sub> is an ideal hydrogen carrier due to its high theoretical storage capacity, 7.6 wt%, low cost, light weight and good reversibility. However, widespread industrial application are inhibited by its stable thermodynamic properties (high desorption temperature 300 °C-400 °C, and low plateau pressure of 10 Pa at ambient condition) and slow hydrogenation/dehydrogenation kinetics. Many experimental efforts have been focused on improving the reaction kinetics of MgH<sub>2</sub>, increasing the plateau pressure and reducing the thermodynamic stability. However, none of them has made Mg-based hydrogen storage materials meet all the requirements for on-board applications successfully. Therefore, the main aims of this work are to improve the hydrogen sorption kinetics of MgH<sub>2</sub> by ball milling and by the catalysts.

In order to improve further the properties of Mg-based hydrogen storage materials, the investigation will focus on the following specific objectives:

- To identify the effects of different milling modes on the hydrogen sorption properties of MgH<sub>2</sub> in order to facilitate the dehydrogenation/hydrogenation kinetics and thermodynamic destabilization;
- To analyze role of particle size and grain size on hydrogen sorption and kinetics of MgH<sub>2</sub>;
- To investigate the influence of transition metal carbides on surface modification and on dehydrogenation/hydrogenation properties of MgH<sub>2</sub>;
- To identify the catalytic mechanism of the selected catalysts on hydrogen sorption properties of MgH<sub>2</sub>.

## CHAPTER 3 EXPERIMENTAL METHODS

### 3.1 Materials and Sample Preparation

#### 3.1.1 Materials

MgH<sub>2</sub> powder was the main material for the study that was purchased from Th. Gold Schmidt AG, with a composition of 95 wt. % MgH<sub>2</sub> and a mean particle size of 50 μm. Other chemicals used for modification of MgH<sub>2</sub> are detailed in Table 3-1.

Table 3-1 Details of chemicals were used in the study at UEA.

Materials	Suppliers	Purity (wt. %)	Particle size
MgH <sub>2</sub>	Th. Gold Schmidt AG	95	50 μm
TiC	Sigma-Aldrich	95	< 200 nm
Mo <sub>2</sub> C	Sigma-Aldrich	99.5	-325 mesh
Ni	Sigma-Aldrich	99.9	< 100 nm

#### 3.1.2 Sample preparation

The powder mixtures were cryogenically milled for 8 h using liquid nitrogen to freeze the sealed milling vial in a SPEX SamplePrep 6750 Freezer/Mill, then were further mechanically milled for 16 h and 60 h at ambient temperature using a high energy ball mill, SPEX 8000D, under Argon atmosphere. Stainless steel vial and balls were used for milling. The initial ball-to-powder weight ratio was 10:1. The weight of (MgH<sub>2</sub> + TiC) mixture was 1.92 g MgH<sub>2</sub> and 0.08 g TiC; the weight of (MgH<sub>2</sub>+Mo<sub>2</sub>C) mixture was 1.74 g MgH<sub>2</sub> and 0.26 g Mo<sub>2</sub>C. After milling, the resulting powder was removed from the vial inside the glove box under high purity argon. Some 60h ball-milled (MgH<sub>2</sub> + TiC)/ (MgH<sub>2</sub>+Mo<sub>2</sub>C) was mixed with nickel in the high energy ball mill, SPEX 8000D for 15 min, equal-weight-ration of Ni to MgH<sub>2</sub> is 5wt.%. The framework of the experiment is listed in Figure 3-1. All the powder handling was performed in a dry glove box under high purity argon.

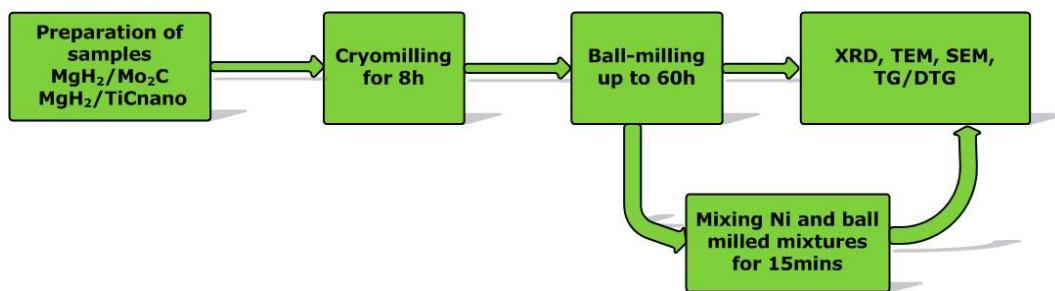


Figure 3-1 The experimental framework

### 3.1.3 Glove box

A glove box was used during sample preparation, as shown in Figure 3-2. The moisture and oxygen levels were maintained below 5 ppm by the function of recirculation of the glove box. A SPEX mill was encased within the glove box to prevent sample oxidation during milling. All steps of sample transfer and preparation for characterization were performed inside the glove box under argon.

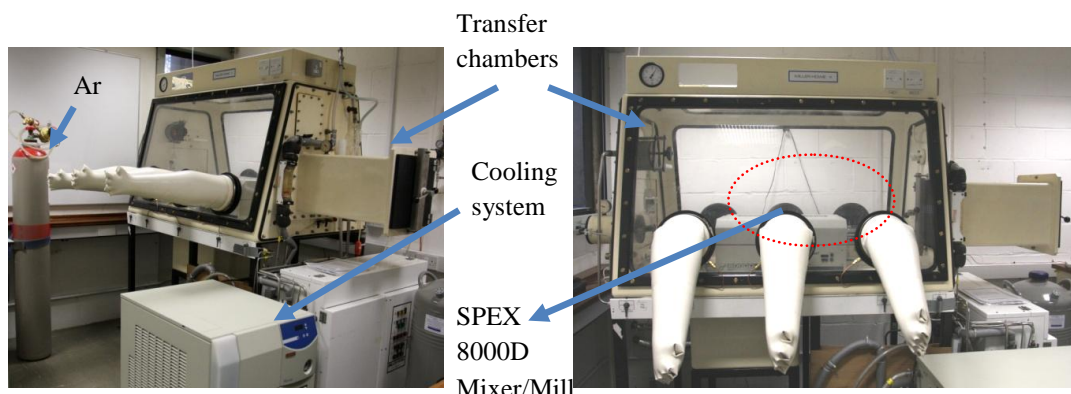


Figure 3-2 Synthesis in a glove box

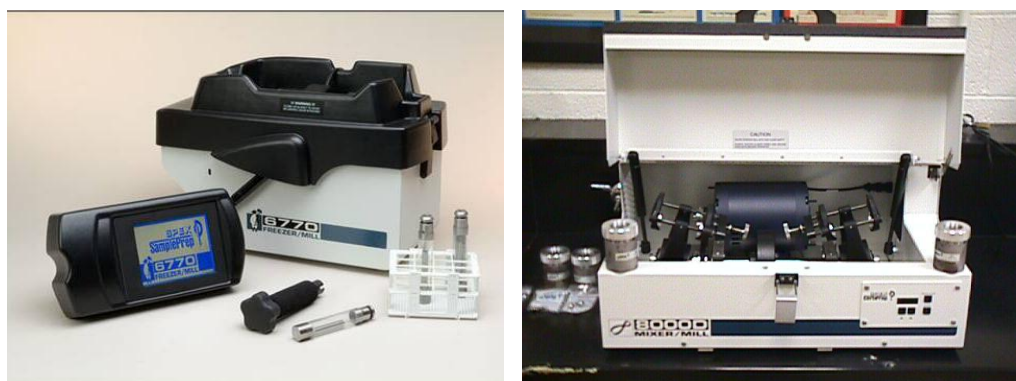


Figure 3-3 SPEX SamplePrep 6750 Freezer/Mill (left) and SPEX 8000D Mixer/Mill (right)

### 3.1.4 Cryogenic milling

SPEX SamplePrep Freezer/Mill 6750 (Figure 3-3 left) is a cryogenic laboratory mill which chills samples in liquid nitrogen and pulverizes them with a magnetically driven impactor. Each sample is placed in a separate grinding vial which is immersed in a liquid nitrogen bath inside the mill. This maintains the low temperature of the sample during grinding. Chilling materials in liquid nitrogen (at temperatures approaching  $-190\text{ }^{\circ}\text{C}$ ) has two important consequences for sample preparation; it embrittles flexible samples so they can be pulverized by impact milling, and it preserves structural and compositional aspects usually damaged or lost during room temperature pulverizing. A Freezer/Mill incorporates an insulated tub into which liquid nitrogen is poured. The grinding mechanism is a magnetic coil assembly suspended in the nitrogen bath. Each sample was placed in a closed grinding vial along with a steel impactor. The magnetic coil shuttles the impactor rapidly back and forth pulverizing the sample against the end plugs of the vial (Figure 3-4). The cryomilling cycles used in this study were 10 min grinding with 1 min rest in-between each grind. The total grinding time was 8 h.

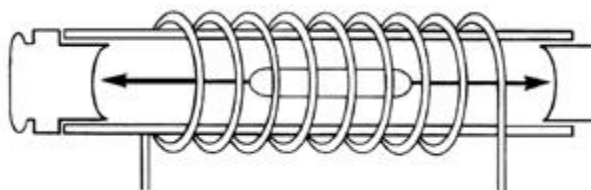


Figure 3-4 Vial and impactor in the SPEX SamplePrep Freezer/Mill 6750<sup>152</sup>

### 3.1.5 Ball milling

Mechanical milling is an effective technique for the preparation of fine metallic and ceramic powders and can also be used to drive a wide range of chemical reactions. Functionally described high-energy ball mill or shaken mill, the SPEX SamplePrep 8000D (shown in Figure 3-3 right), shakes two clamps back and forth several thousand times a minute. In each

clamp, a vial containing sample and balls, is shaken in a complex motion which combines back-and-forth swings with short lateral movements, shown in Figure 3-5. With each swing the balls impact against one end of the vial, simultaneously milling the sample and blending it. Because of the amplitude and velocity of the clamp's swing, each ball develops fairly high grinding-forces.

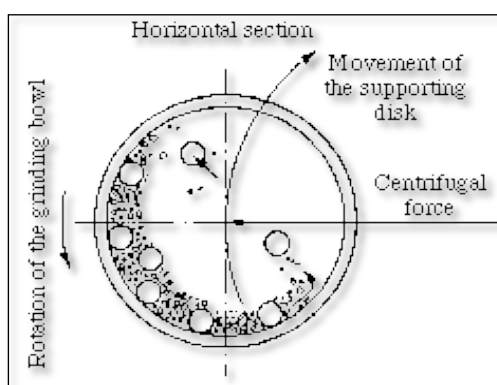


Figure 3-5 Diagram of ball milling<sup>153</sup>.

## 3.2 Analysis of Sample Morphology and Structure

### 3.2.1 X-ray diffraction (XRD)

X-ray diffraction (XRD) is a versatile, non-destructive technique that reveals detailed information about the chemical composition and crystallographic structure of the materials. XRD used in this study was mainly for detecting the phase transformation of the materials during mechanical milling, dehydrogenation, and for the analysis of crystallite size. A XTra diffractometer (Thermo ARL, the United States) was used for powder X-ray diffraction. The source was Cu  $K_{\alpha}$  ( $\lambda=1.554056\text{\AA}$ ) radiation from a conventional water-cooled X-ray tube. The scan range was from  $2\theta = 10^{\circ}$  to  $80^{\circ}$  and the scan rate was  $1.2^{\circ}/\text{min}$  with a step size of  $0.02^{\circ}$ . In order to avoid exposure to air, the XRD samples were prepared in the glove box and a sample holder covered with an airtight plastic dome which had a negligible effect on diffraction patterns was used. The nanograin (crystallite) size of phases residing in the

milled powders was calculated from the broadening of their respective XRD peaks. Since the Bragg peak broadening in an XRD pattern is due to a combination of grain refinement (nanograin/crystallite) and lattice strains, it is customary to use computing techniques by means of which one can separate these two contributions. The crystallite size was obtained from Scherrer formula:

$$D = K\lambda / (B \cos\theta) \quad \text{Equation 3-1}$$

Where D is the averaged dimension of crystallites; K is the Scherrer constant, a somewhat arbitrary value that falls in the range 0.87-1.0 (it is usually assumed to be 1);  $\lambda$  is the wavelength of X-ray; and B is the integral breadth of a reflection (in radians  $2\theta$ ) located at  $2\theta$ . B is often calculated relative to a reference solid (with crystallite size  $>500$  nm) added to the sample:  $B^2 = B_s^2 - B_r^2$ . The program JADE 5.0 was used to evaluate the diffraction patterns.

### **3.2.2 Scanning Electron Microscopy (SEM) and Transmission Electron Microscopy (TEM)**

The scanning electron microscope (SEM) uses a focused beam of high-energy electrons to generate a variety of signals at the surface of solid specimens. The signals that derive from electron-sample interactions reveal information about the sample including external morphology, chemical composition, and crystalline structure and orientation of materials making up the sample. All the samples were coated with an ultrathin coating of gold by vacuum sputter coating. The coating of gold increases signal and surface resolution, especially with samples of low atomic number. The improvement in resolution arises because backscattering and secondary electron emission near the surface are enhanced and thus an image of the surface is formed.

Backscattered electrons (BSE) consist of high-energy electrons originating in the electron beam, which are reflected, or back-scattered, out of the specimen interaction volume by

elastic scattering interactions with specimen atoms. Since heavy elements (high atomic number) backscatter electrons more strongly than light elements (low atomic number), they appear brighter in the image. BSE were used to detect contrast between areas with different chemical compositions in this study. A JEOL (Japan) thermionic SEM was used for the image analyses.

Transmission Electron Microscopy (TEM) was employed to further examine the particle size and particle distribution of samples. It exploits the very small wavelengths of high-energy electrons to probe solids at the atomic scale. A Jeol JEM 2100 TEM in the 200kV class analysis has been developed to achieve the highest image quality and analytical performance with a probe size under 0.2 nm. For TEM observation, a dilute suspension of sample powder was dropped onto a TEM grid, and dried.

The particle sizes of the powder mixtures were calculated from the SEM and TEM images as the equivalent circle diameter,  $ECD = \frac{1}{2} \left( \frac{4A}{\pi} \right)^{1/2}$ , where A represents the projected particle area, using the *Image Tool v.3.00 software*.

### **3.3 Analysis of Hydrogen Sorption Properties: Intelligent Gravimetric Analyzer -Mass Spectrometry (IGA-MS)**

Thermogravimetry (TG) measurements for dehydrogenation and gas sorption were carried out using the IGA-003 supplied by Hidden Analytical Ltd, Figure 3-6. The IGA apparatus is an ultrahigh vacuum system which allows the adsorption-desorption isotherms and the corresponding kinetics of gas and vapor sorption on materials. The system consists of a fully computerized microbalance which constantly measures the mass of specimen as the test proceed, Results are displayed as a mass loss or gain as a function of temperature and time. By analysis of IGA results, the hydrogen sorption kinetics and storage capacities of the materials at different temperatures can be obtained. The method of differential

thermogravimetry (DTG) analysis, which was calculated from TG data, was used for thermal investigations of analytical precipitates. The peak of DTG curve means that the maximum rate of weight loss recorded by TG. There is good agreement of the onset temperature and the peak temperature of the materials between the DTG and MS curves.



Figure 3-6 Intelligent Gravimetric Analyzer (IGA-003) combined with Mass Spectrometer.

Desorption was performed from 20 to 500 °C under 1 bar Helium pressure at a heating rate of 10 °C/min and He flow rate of 150 ml/min. Hydrogen absorption was measured at hydrogen pressure of 8 bar with H<sub>2</sub> flow rate of 150 ml/min and isothermal temperature of 300 °C for 120 min with heating rate of 10 °C/min. Impurity gas absorption was measured using 80 % H<sub>2</sub> and 20 % CO<sub>2</sub> gas mixture at 8 bar and 300 °C for 120 min. The gas sorption procedure for all the sample (shown in Figure 3-7) was to start from the desorption because MgH<sub>2</sub>, as the basic synthetic material, need to be dehydrogenated, and then was gas adsorption process. After a circle of sorption, some materials run the second circle for further analyses. The system need to be purged by He 3 times when every new sample is loaded into the IGA instrument. The IGA provided a highly sensitive measurement with precise temperature and pressure control for automated measurements of adsorption and

desorption isotherms. With a typical sample size of 20~50 mg, the error in the hydrogen absorption and desorption processes due to instrumental limitations is (0.02 wt % absolute).

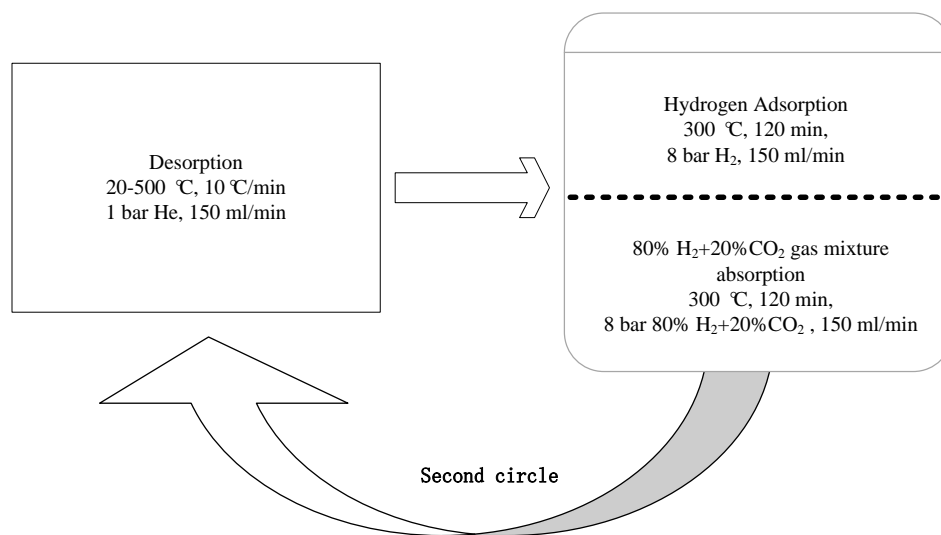


Figure 3-7 Gas sorption procedure in IGA-MS

MS (Mass Spectrometry) is an analytical technique for the determination of the elemental composition of a sample or molecule. The technique has both qualitative and quantitative uses. These include identifying unknown compounds, determining the isotopic composition of elements in a molecule, and determining the structure of a compound by observing its fragmentation. The technique employs chemical fragmentation of a sample into ions and measurements of two properties, charge and mass, of the resulting chemical compounds. The ratio of charge-to-mass of the chemicals or molecules is calculated by passing them through electric and magnetic fields in a mass spectrometry.

MS instruments consist of three modules: an ion source, which can convert gas phase sample molecules into ions (or in the case of electrospray ionization, move ions that exist in solution into the gas phase); a mass analyzer, which sorts the ions by their masses to charge ration

within a varying electromagnetic field; and a detector, which measures the quantity of each indicator providing data for calculating the abundances of each ion present.

The sample gas, liberated from the IGA reactor during thermal desorption, is introduced into the mass spectrometer via a pipe connecting the IGA to the MS (Figure 3-6). The MS analysis software includes two kinds of scan: BAR scan, is used to detect the unknown compounds during the scanning, these mass values need to be matched to the library database to determine the product. MID scan, is designed to detect the already supposed compounds by setting up the mass of possible molecules before running the experiment along with their mass spectrum and their mass evolution during the experiment as a function of time. In this study, MID method was used to investigate the gaseous species released from IGA reactor during sorption process.

There are several methods (proposed by Chan and Balke<sup>154</sup>, Friedmam<sup>155</sup>, Freeman and Carroll<sup>156</sup>, and Chang<sup>157</sup>) for calculating kinetic parameters which depend not only on the experimental conditions but also on the mathematical treatment of the data<sup>64</sup>. In this study, The Chan and Balke<sup>154</sup> method is used to evaluate the **activation energy E** based on the DTG analysis. For many kinetic processes, a rate of reaction may be expressed as a product of a temperature-dependent function,  $k(T)$ , and a composition- or conversion-dependent term,  $f(x)$ :

$$r = \frac{dX}{dt} = k(T)f(x) \quad \text{Equation 3-2}$$

Where T is absolute temperature (in K); X is conversion and  $r$  is the rate of change of conversion or composition per unit time (t). The temperature-dependent term in Equation 3-2 is the reaction rate constant, which is assumed to obey the usual Arrhenius relationship:

$$k(T) = A \exp\left(-\frac{E}{RT}\right) \quad \text{Equation 3-3}$$

Where E is the activation energy of the kinetic process, A is the pre-exponential factor, and R is the universal gas constant (8.314 J/ mol/K). The conversion-dependent function,  $f(x)$ , is generally very complicated. A particular term is usually valid only for a limited range of experimental conditions. However, if it is assumed that a simple  $n$ th-order kinetic relationship holds for the conversion-dependent term such that

$$f(X) = (1 - X)^n \quad \text{Equation 3-4}$$

and that the quantity (1-X) can be replaced by W, the weight fraction remaining in a TG run, then:

$$r = -\frac{dW}{dt} = AW^n \exp\left(-\frac{E}{RT}\right) \quad \text{Equation 3-5}$$

Or

$$\ln r = \ln\left(-\frac{dW}{dt}\right) = \ln A + n \ln W - \frac{E}{RT} \quad \text{Equation 3-6}$$

Published methods of deriving kinetic parameters from TG data centre around Equation 3-6. They involve either a single thermogram or multiple thermograms with different constant heating rates. The constant heating rate method for determining the rate equation parameters is used in this study.

In the work, the order of reactions  $n$ , including dehydrogenation and hydrogenation, is 1 (a first-order reaction), then Equation 3-6 becomes:

$$\ln r = \ln \left( -\frac{dW}{dt} \right) = \ln A + \ln W - \frac{E}{RT} \quad \text{Equation 3-7}$$

$$\ln \left( -\frac{dW}{dt} \right) - \ln W = E \left( -\frac{1}{RT} \right) + \ln A$$

$$\ln \left( \frac{-\frac{dW}{dt}}{W} \right) = E \left( -\frac{1}{RT} \right) + \ln A \quad \text{Equation 3-8}$$

If we assume that the activation energy  $E$  is constant over a specific temperature range, then the slope over this range of a plot of  $\ln \left( \frac{-\frac{dW}{dt}}{W} \right)$  versus  $\left( -\frac{1}{RT} \right)$  should be equal to the activation energy  $E$ .

## CHAPTER 4      EXPERIMENTAL RESULTS AND DISCUSSIONS

### 4.1    Particle Size and Grain Size Effects on Sorption Properties of MgH<sub>2</sub>

The development of nanograins occurs during hydride powder processing by mechanical (ball) milling, which is the principal process used to induce a nanostructure<sup>46</sup>. Particle size reduction by mechanical milling improves MgH<sub>2</sub> dehydrogenation properties due to a shortened hydrogen diffusion path. It is reported that the desorption temperature of MgH<sub>2</sub> decreases rapidly with decreasing mean particle size to nanometric value ~338 nm, resulting in the reduction of the onset and peak desorption temperatures by as much as 70 and 40 °C, respectively<sup>158</sup>. The objective of this section is to explore the effect of cryogenic milling and ball milling on particle & grain size, and understand in more depth the role of particle size and grain size on the reduction of desorption temperature.

#### 4.1.1 Structural characterizations of MgH<sub>2</sub> powder produced by cryogenic milling and ball milling

The XRD pattern of the as-received MgH<sub>2</sub> shows the only major peaks of β-MgH<sub>2</sub>. Cryogenic milling for 8 h and longer durations of ball-milling resulted in the appearance of XRD peaks arising from the γ- MgH<sub>2</sub> phase, as shown in Figure 4-1. The metastable γ- MgH<sub>2</sub> is a high pressure polymorphic form of β-MgH<sub>2</sub> and is commonly observed to appear after ball milling of MgH<sub>2</sub>. The high pressure required to transform β-MgH<sub>2</sub> into γ- MgH<sub>2</sub> is provided during milling through the localized on-contact impacting action of the impactor and steel balls on the MgH<sub>2</sub> powder particles in the vial (Figure 3-3 and Figure 3-4). It is suggested that the formation of γ-MgH<sub>2</sub>, as a metastable high-pressure phase, has a positive effect on hydrogen desorption as a result of a rearrangement in the cation and anion substructures, which destabilises β-MgH<sub>2</sub> reducing the desorption temperature<sup>71, 159</sup>. The XRD peaks of MgH<sub>2</sub> broadened with milling time, indicating a decrease of crystallite size,

compared with the as-received powders. Table 4-1 shows the estimates of nanograin size of the  $\beta$ -MgH<sub>2</sub> phase according to Equation 3-1. The grain size of the as-received MgH<sub>2</sub> is of the order of  $65 \pm 5$  nm, which correlates very well with the grain size reported by Kojima *et al*<sup>160</sup> and Varin *et al*<sup>161</sup>. After cryogenic milling for 8 h, a decrease of  $\beta$ -MgH<sub>2</sub> grain size of  $\sim 25 \pm 3$  nm occurred. It has been suggested that the presence of liquid nitrogen during cryomilling has several advantages, such as decreased oxygen contamination<sup>21</sup> and enhanced deformation during milling<sup>162</sup>. Cryogenic milling in particular offers an effective solution for achieving fine powders by enhancing the brittleness and reducing the tensile strength of the materials<sup>162</sup>. At the same time broadened and less intense XRD peaks of  $\gamma$ -MgH<sub>2</sub> did not allow us to make any meaningful estimate of  $\gamma$ -MgH<sub>2</sub> grain size. However, based on the extent of the  $\gamma$ -MgH<sub>2</sub> peak broadening, it can be concluded with reasonable certainty that the grain size of the  $\gamma$ -MgH<sub>2</sub> phase is not larger than that of  $\beta$ -MgH<sub>2</sub> counterpart. With a further 60 h ball milling, the grain size of MgH<sub>2</sub> is only reduced slightly to  $20 \pm 3$  nm with the appearance of MgO due to the presence of oxygen in the glove box and the high reactivity of magnesium. The  $\gamma$ -MgH<sub>2</sub> peak is enhanced, which indicates more  $\beta$ -MgH<sub>2</sub> phase is transformed to  $\gamma$ -MgH<sub>2</sub> with increased milling time.

The morphology and microstructure of the as-received MgH<sub>2</sub>, 8 h cryomilled MgH<sub>2</sub>, and 60 h ball-milled MgH<sub>2</sub> after 8 h cryomilling were further investigated by scanning electron microscope (SEM), shown in Figure 4-2. The average particle sizes and the range of particle sizes were calculated according to the SEM images. The average particle size of MgH<sub>2</sub> is reduced to about  $\sim 190 \pm 20$  nm after 8 h of cryomilling (Figure 4-2b). Some of the particles become smaller and others are aggregated to relatively bigger particles after further ball milling for 60 h milling, shown in Figure 4-2c. SEM images and the mean particle sizes figure illustrate the slight increase of the mean particle sizes of MgH<sub>2</sub> after a further 60 h. Compared with the cryomilled powder, due to the agglomeration of fine particles and

perhaps cold weld of some particles during 60 h milling, it is also noticed that the range of particle sizes is broadened because of the formation of smaller particles and the aggregation of fine particles, Figure 4-2 d. A smaller particle size or grain size enhances hydrogen absorption/desorption, because it shortens the diffusion path of hydrogen through the bulk area, and enlarges the grain boundaries and active surface area<sup>15</sup>.

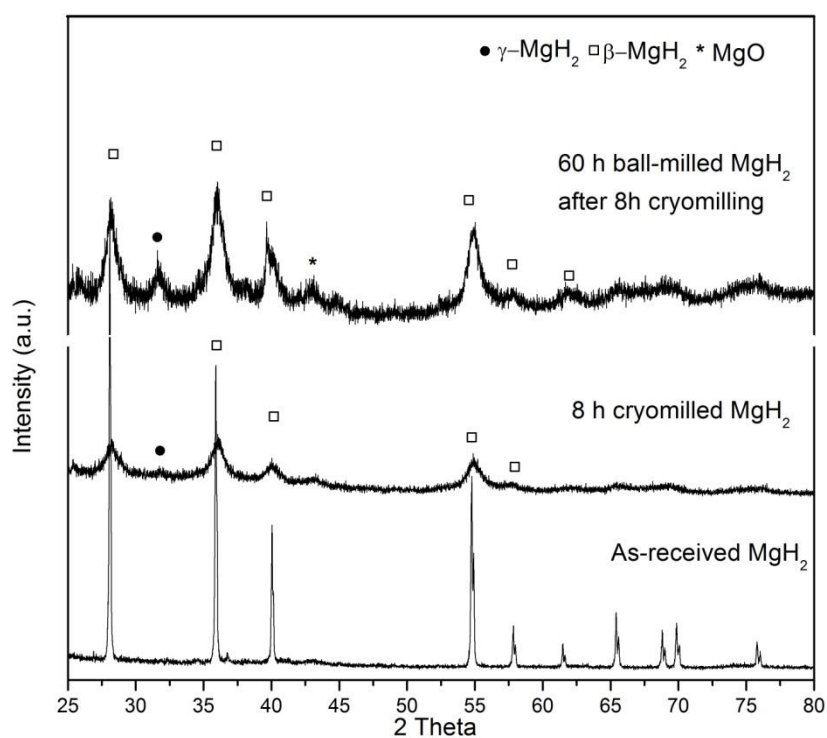


Figure 4-1 X-ray diffraction patterns of the as-received MgH<sub>2</sub>, 8 h cryomilled MgH<sub>2</sub> and 60 h ball-milled MgH<sub>2</sub> after 8 h cryomilling.

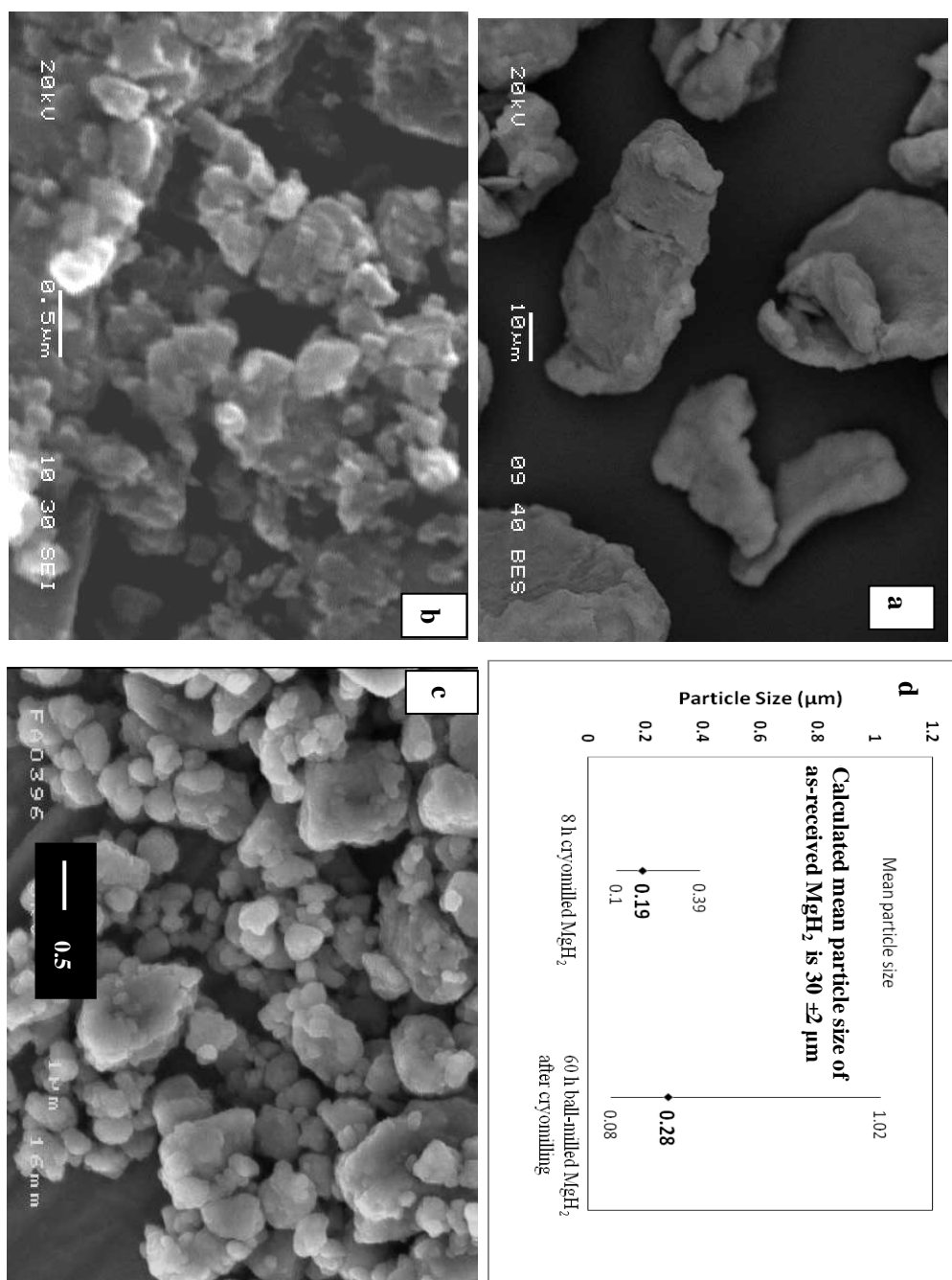


Figure 4-2 SEM images of (a) as-received  $\text{MgH}_2$ , (b) 8 h cryomilled  $\text{MgH}_2$ , (c) 60 h ball-milled  $\text{MgH}_2$  after cryomilling; and (d) particle sizes of them.

### 4.1.2 Dehydrogenation of $\text{MgH}_2$ by cryogenic milling and ball milling

Figure 4-3 and Figure 4-4 show the thermogravimetric (TG) and derivative thermogravimetric (DTG) curves of hydrogen desorption of the cryomilled and cryomilled followed by ball-milled  $\text{MgH}_2$  for different hours. The total relative weight loss of as-received  $\text{MgH}_2$  and cryomilled  $\text{MgH}_2$  for 8 h is about  $7 \pm 0.02$  wt. % and  $7.2 \pm 0.02$  wt. %, respectively. The extra  $0.2 \pm 0.02$  wt. % is due to the more thorough desorption of nanosized  $\text{MgH}_2$  particles. The weight loss of dehydrogenation of 60 h ball-milled  $\text{MgH}_2$  is  $6 \pm 0.02$  wt. % due to the formation of an insignificant amount of  $\text{MgO}$  during cryomilling detected from the XRD patterns, or small amount of hydrogen released during high energy milling at room temperature.

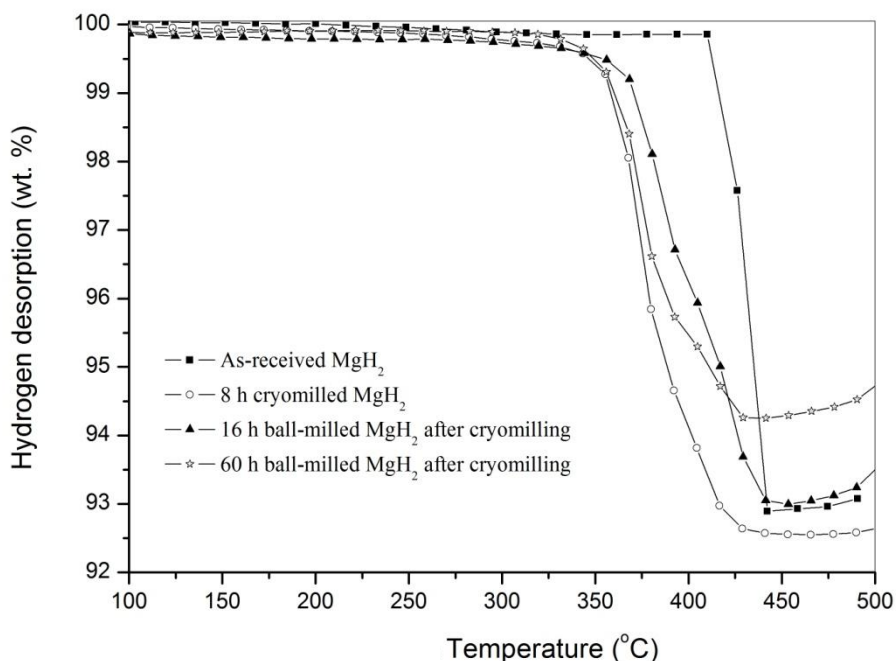


Figure 4-3 Thermogravimetry (TG) curves of cryomilled and ball-milled  $\text{MgH}_2$  at the heating rate of 10 K/min and 1 bar helium pressure.

DTG curves of dehydrogenation for the milled mixtures are calculated to identify the onset and peak desorption temperatures, as previously explained in Chapter 3. A single

endothermic hydrogen desorption peak with the maximum at  $\sim 434$  °C characterises hydrogen desorption from as-received  $\text{MgH}_2$  (the calculated mean particle size is around  $31 \mu\text{m}$ , as shown in Table 4-1). The 8 h cryomilled  $\text{MgH}_2$  starts to decompose at  $320$  °C and reaches the peak at temperature  $362$  °C (seen Table 4-1). It is also investigated a peak doublet/shoulder on the right hand side appears after cryomilling, which suggesting an overlap of low-temperature and high-temperature desorption peaks. Two research groups, Varin *et al* and Czujko *et al* reported that such a two-step hydrogen desorption may occur owing to the existence of two fractions of powder particles: small and large, which could desorb at lower and higher ranges of differential scanning calorimetry (DSC) temperatures, respectively<sup>163</sup>. The existence of smaller and larger fractions of particle sizes is well supported by the SEM and particle sizes range from Figure 4-2, as discussed earlier in this chapter. However, an alternative explanation can be based on the findings of Schimmel *et al.*<sup>164</sup>, who reported that in a ball-milled nanostructure of  $\text{MgH}_2$ , there may exist a substoichiometric nanostructure,  $\text{MgH}_x$  phase (where  $x < 2$ ). Such a hydrogen deficient phase is likely to exhibit much faster diffusion of hydrogen due to the large concentration of vacancies and could desorb at lower temperatures than the stoichiometric  $\beta\text{-MgH}_2$ , giving rise to a shoulder or even peak doublet (Figure 4-4). Furthermore, this could occur with dual-phase ( $\beta\text{-MgH}_2$  and  $\gamma\text{-MgH}_2$ ) powders. The low-temperature peak in a doublet could correspond to the desorption from the  $\gamma\text{-MgH}_2$  hydride due to the lower desorption temperature for  $\gamma\text{-MgH}_2$  and the high-temperature peak would correspond to the desorption from  $\beta\text{-MgH}_2$ , as reported by Gennari *et al*<sup>73</sup>.

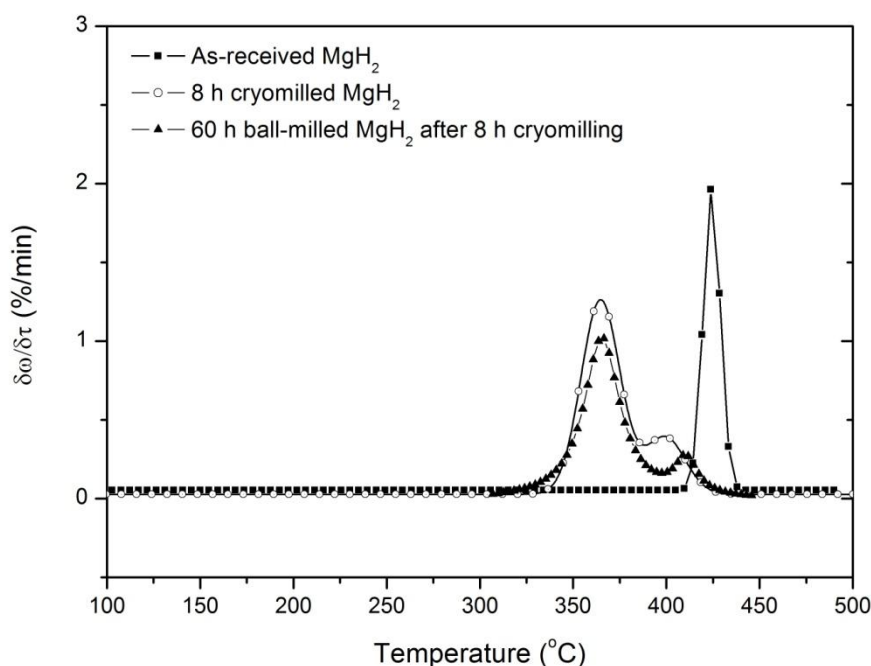


Figure 4-4 Derivative thermogravimetric (DTG) curves of cryomilled and further ball-milled  $\text{MgH}_2$ , derived from Figure 4-3.

The starting desorption temperature of 8 h cryomilled  $\text{MgH}_2$  is 320 °C much lower compared to that of the as-received  $\text{MgH}_2$  ( $T_{\text{onset}}=418$  °C,  $T_{\text{peak}}=434$  °C), which is due to the effect of milling on particle and grain size reduction. After a further 60 h ball-milling of cryomilled  $\text{MgH}_2$ , the onset temperature is only slightly reduced to 305 °C due to the smaller grain size of  $\text{MgH}_2$ , although the formation of  $\gamma$ -  $\text{MgH}_2$  is more prevailing in ball-milled  $\text{MgH}_2$  than that in cryomilled sample. There is no difference in peak temperature between cryomilled  $\text{MgH}_2$  and further 60 h ball-milled  $\text{MgH}_2$ . This indicates that the factor of refined nano particle size and grain size within the particles are responsible for a substantial reduction of hydrogen desorption temperature of  $\text{MgH}_2$ .

From the slope of the fitted line, the overall activation energy ( $E'$ ) of  $\text{H}_2$  desorption of the samples is obtained, as shown in Figure 4-5. The activation energy of desorption is as high as  $235 \pm 10$  kJ/mol for as-received  $\text{MgH}_2$ . When as-received  $\text{MgH}_2$  is cryogenically milled

for 8 hours, the value is decreased to  $200 \pm 9$  kJ/mol. Further ball milling to 60 h after cryomilling doesn't reduce the activation energy further. The desorption kinetics can be improved greatly by cryogenic milling. The lower activation energy also facilitates the reduction of the desorption temperature.

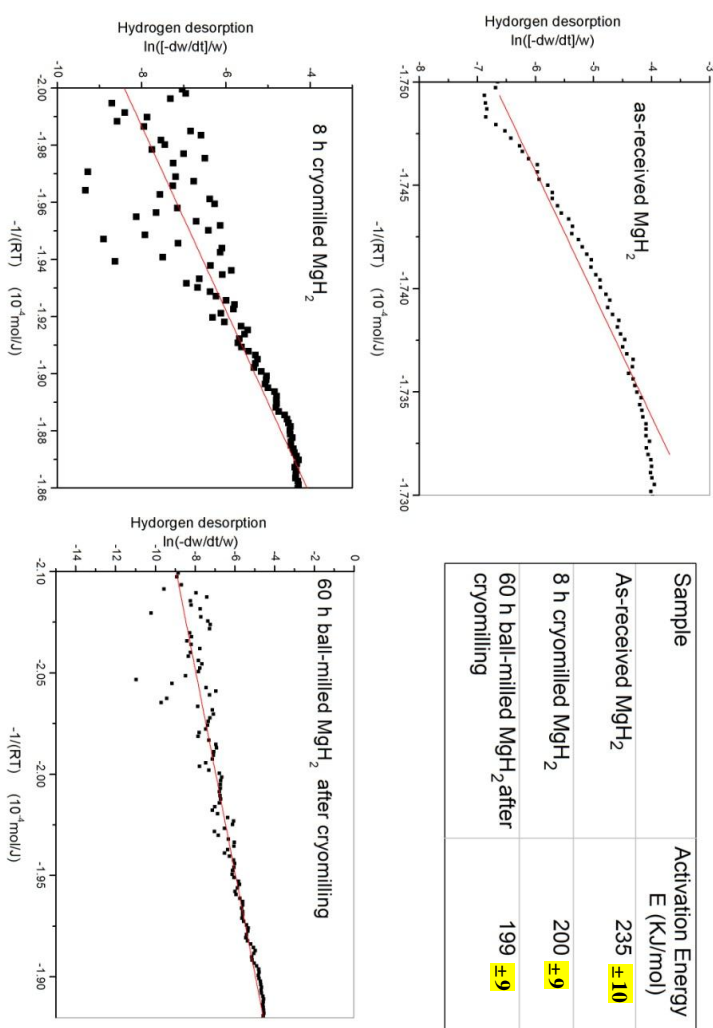


Figure 4-5 Kinetic plots and activation energy of the MgH<sub>2</sub> samples, based on Figure 4-4 and Equation 3-8

### 4.1.3 Hydrogenation of MgH<sub>2</sub> by cryogenic milling and subsequent ball milling

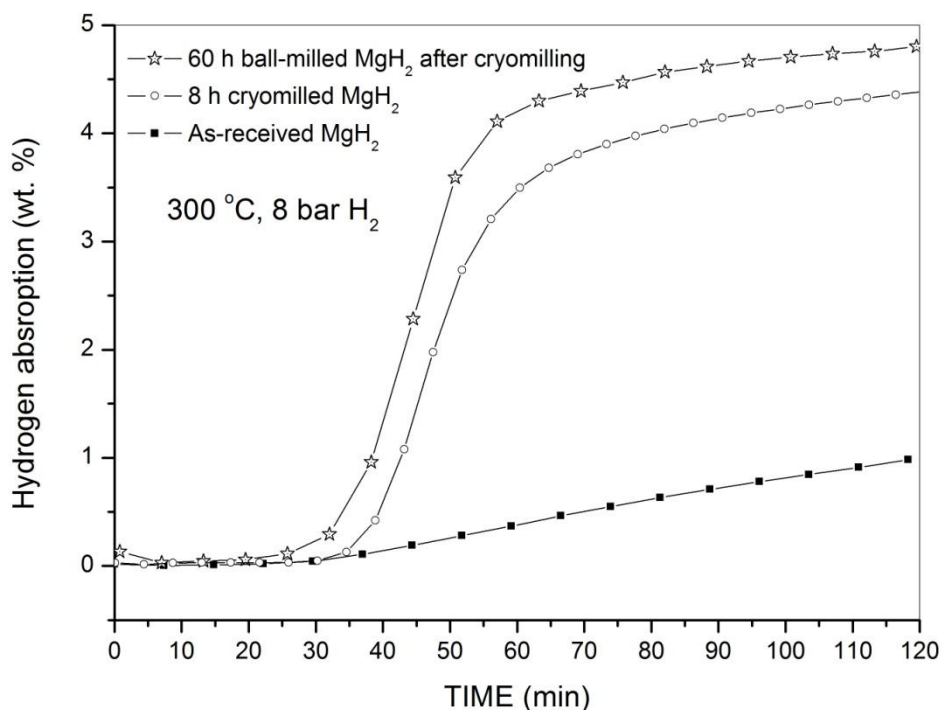


Figure 4-6 Hydrogen absorption curves of the cryomilled and ball-milled MgH<sub>2</sub>, measured under 8 bar H<sub>2</sub> pressure at 300 °C.

The hydrogen absorption kinetics of the dehydrogenated MgH<sub>2</sub> samples were measured within 8 bars H<sub>2</sub> pressure at 300 °C, Figure 4-6. The hydrogen uptake is very slow for the as-received MgH<sub>2</sub> after dehydrogenation. However, about 4 wt. % of hydrogen is adsorbed in 60 min for dehydrogenated cryomilled-MgH<sub>2</sub>. After cryomilling and ball-milling, H<sub>2</sub> absorption of the dehydrogenated sample is 5 ± 0.02 wt. % in 60 min, also the absorption rate is enhanced to 0.10 ± 0.0001 Δwt. %/min due to the ball milling process (Table 4-1). The relatively lower maximum weight percentage of H<sub>2</sub> uptake of dehydrogenated milled-MgH<sub>2</sub> is probably due to slow kinetics and slight oxidation of the samples during milling.

Table 4-1 Estimates of grain size (crystallite size), particle size of  $\beta$ -MgH<sub>2</sub> from XRD and SEM analysis, and TG-DTG desorption temperature ( $T_{\text{Onset}}$  is onset temperature of desorption,  $T_{\text{Peak}}$  is peak temperature of desorption.)

Sample	As-received MgH <sub>2</sub>	8 h cryomilled MgH <sub>2</sub>	60 h ball-milled MgH <sub>2</sub> after cryomilling
<b>Grain Size of <math>\beta</math>-MgH<sub>2</sub> (nm)</b>	65 ± 5	25 ± 3	20 ± 3
<b>Mean particle size (<math>\mu\text{m}</math>)</b>	30 ± 2	0.19 ± 0.02	0.28 ± 0.02
<b><math>T_{\text{Onset}}</math> (°C)</b>	418	320	305
<b><math>T_{\text{Peak}}</math> (°C)</b>	434	362	360
<b>E' (KJ/mol)*</b>	235 ± 10	200 ± 9	199 ± 9
<b>Absorption Rate (wt. %/min)</b>	0.008 ± 0.00004	0.06 ± 0.0001	0.10 ± 0.0001

\* Activation energy calculated from Equation 3-8.

#### 4.1.4 Summary

Continuous refinement of the powder particle and nano-grain (crystallite) size of as-received MgH<sub>2</sub> was achieved by cryogenic milling and subsequent ball milling. The microstructure of MgH<sub>2</sub> powders after ball-milling showed obvious dual phases ( $\beta$ -MgH<sub>2</sub> +  $\gamma$ -MgH<sub>2</sub>), where  $\beta$ -MgH<sub>2</sub> as the main peak of MgH<sub>2</sub> in XRD pattern has nanometric size grains (crystallites). Cryogenic milling is effective in reducing the grain sizes and particle sizes. The smallest mean powder particle size achieved in this work after 8 h cryogenic milling was 190 nm.

The onset and peak temperatures of H<sub>2</sub> desorption of the MgH<sub>2</sub> were substantially reduced by cryogenic milling for 8 h due to the smaller and more uniform nano particles achieved by cryomilling in the presence of liquid nitrogen.

The hydrogen absorption property of dehydrogenated MgH<sub>2</sub> was enhanced by cryogenic milling and ball-milling. The absorption of dehydrogenated MgH<sub>2</sub> after cryomilling and ball-milling increased greatly to 4 ± 0.02 wt. % in 60 min compared to that of dehydrogenated as-received MgH<sub>2</sub> (< 0.5 wt. %) at 300 °C and 8 bar hydrogen pressure. Further ball-milling increased slightly the rate of hydrogen absorption of dehydrogenated MgH<sub>2</sub>.

## 4.2 Effects of TiC Nanoparticles on Hydrogen Sorption of MgH<sub>2</sub>

The hydrogen sorption properties of MgH<sub>2</sub> may be improved by transition metals, oxides and fluorides<sup>13, 16, 165</sup>. Transition-metal compounds have attracted considerable interest as effective catalysts, due to the high affinity of transition-metal cation for hydrogen<sup>18, 107</sup>. For example, the addition of small quantities of Nb<sub>2</sub>O<sub>5</sub> significantly improves both the absorption and desorption kinetics of MgH<sub>2</sub><sup>19, 20</sup>. Comparative studies based on various transition-metal oxides emphasise that the appropriate chemical interaction between catalyst and host hydride is essential for realising high catalytic activity, suggesting the functionality of the contact anion in tailoring the activity of the transition-metal cation<sup>20</sup>. Titanium-based compounds have been successfully used to improve sorption kinetics in several hydrogen storage systems, exhibiting a high affinity of Ti cation for hydrogen even at moderate temperatures. For example, titanium halides are exceptionally effective in reducing the kinetic barrier to dehydrogenation of alkaline alanates<sup>21, 22, 107</sup>. It has also been found that the temperature for hydrogen release from MgH<sub>2</sub> can be greatly reduced by doping it with Ti-containing agents (e.g. TiF<sub>3</sub> and TiC)<sup>16, 23</sup>. The interactions between the hydrides and the Ti-containing agents weaken the Mg–H bonds and thus facilitate the recombination of hydrogen atoms to the hydrogen molecules. The aim of this part of the project is to gain further understanding of the influences of TiC with cryomilling and ball-milling on hydrogen sorption properties of MgH<sub>2</sub>.

### 4.2.1 Structural characterizations of milled mixtures of MgH<sub>2</sub> and TiC

Figure 4-7 presents the XRD patterns of the (MgH<sub>2</sub> + 2 mol. % TiC) mixtures milled for different hours. After cryomilling and ball milling of MgH<sub>2</sub> with TiC nanoparticles, the main phases that appear are only the parent materials, MgH<sub>2</sub> and TiC. The Fe phase was detected in the ball-milled samples was from the collision of milling vial and balls. There is no new compound formed from the mixture. The metastable orthorhombic  $\gamma$ -MgH<sub>2</sub> is detected

simultaneously with  $\beta$ -MgH<sub>2</sub> from 16 h ball-milled (MgH<sub>2</sub>+ 2% TiC) pre-cryomilled for 8 h. The formation of  $\gamma$ -MgH<sub>2</sub> during high energy ball milling of MgH<sub>2</sub> was investigated earlier in chapter 4.1. The XRD peaks of MgH<sub>2</sub> broaden with milling time, indicating the decrease of crystallite size, compared with the as-received powders. From the XRD patterns of the dehydrogenated (MgH<sub>2</sub> + 2%TiC) mixture cryomilled for 8 h and further ball-milled for 60 h, Figure 4-7, only Mg and TiC peaks are detected in the dehydrogenated mixture. There is no reaction between TiC and Mg/MgH<sub>2</sub>. TiC retains its original form during milling and after dehydrogenation, TiC is known to be a very stable compound with a formation enthalpy of  $-190.4 \pm 17.0$  kJ/mol based on direct reaction from Ti and C powders<sup>20</sup>.

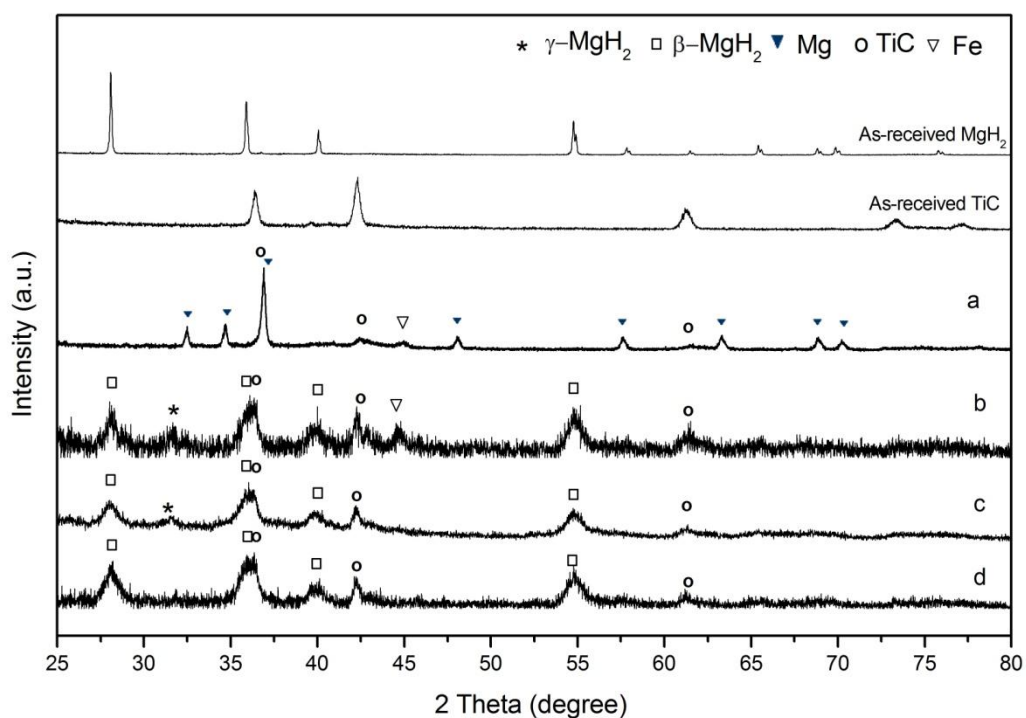


Figure 4-7 X-ray diffraction patterns of the as-received MgH<sub>2</sub>, TiC and the milled (MgH<sub>2</sub>+2mol.% TiC) mixtures. (a) Dehydrogenated (MgH<sub>2</sub>+2%TiC) after cryomilling and 60 h ball milling, (b) (MgH<sub>2</sub>+2%TiC) ball milled for 60 h after cryomilling, (c) (MgH<sub>2</sub>+2%TiC) ball milled for 16 h after cryomilling, (d) (MgH<sub>2</sub>+2%TiC) cryomilled for 8h.

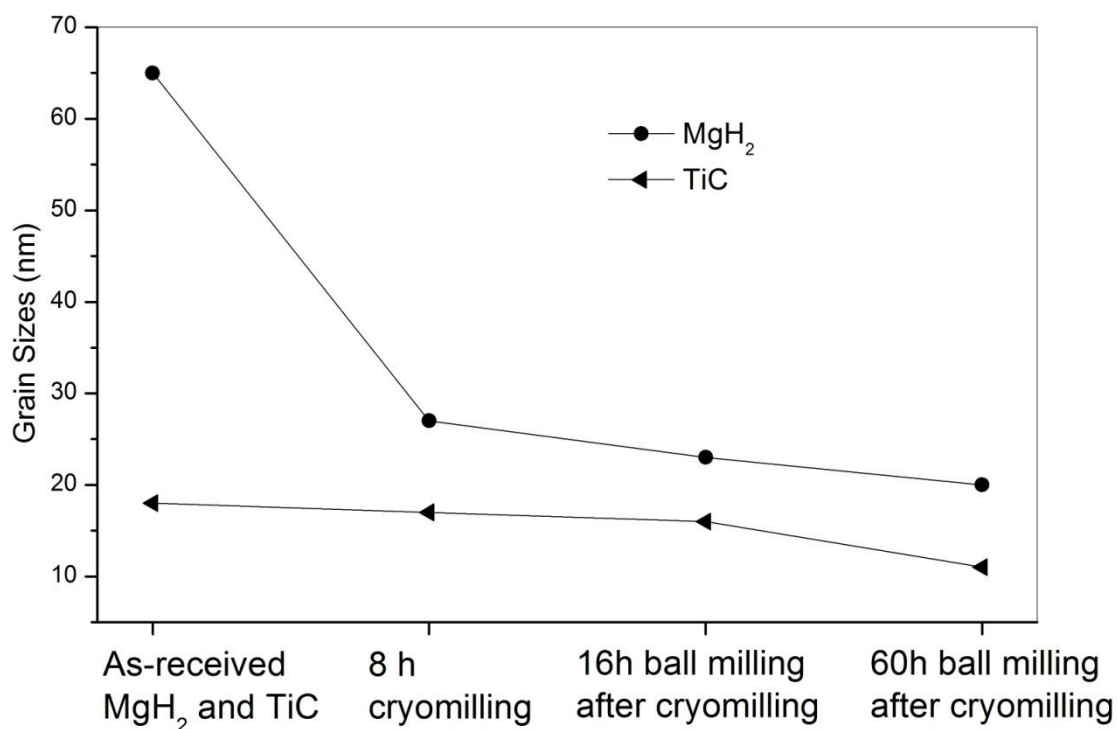


Figure 4-8 Grain sizes of MgH<sub>2</sub> and 2%TiC before and after milling, calculated from XRD patterns of the as-received MgH<sub>2</sub>, TiC and the milled (MgH<sub>2</sub>+2%TiC) mixtures.

Figure 4-8 shows the estimates of the nanograin size of the as-received MgH<sub>2</sub> calculated based on XRD pattern is of the order of  $65 \pm 5$  nm. After 8 h cryogenic milling, the grain size of MgH<sub>2</sub> is decreased greatly to  $25 \pm 3$  nm. It has been suggested that the presence of liquid nitrogen during cryomilling has several advantages, such as decreased oxygen contamination<sup>166</sup> and enhanced deformation during milling<sup>162</sup>. With a further 60 h ball milling, the grain size of MgH<sub>2</sub> is only reduced slightly to  $20 \pm 3$  nm. Furthermore, the grain size of TiC is decreased to  $10 \pm 1$  nm with a further 60 h ball-milling, compared with the initial size of  $18 \pm 3$  nm. Therefore, the cryogenic milling process is very effective in reducing the crystallite size of MgH<sub>2</sub>, and further high energy ball milling only reduces the grain size to some extent. Cryogenic milling provides significant improvements to surface residual stresses and the effectiveness of grinding forces mainly due to a substantial

temperature reduction in grinding zone and a decrease in magnitude of tensile residual stress for all the materials<sup>148</sup>. However, the grain size of TiC does not decrease greatly after 8 h cryomilling ( $17 \pm 3$  nm) due to its very low content in the mixture (2 mol %) and original small grain size ( $18 \pm 3$  nm) which is more difficult to reduce further by cryogenic milling.

The morphology and microstructure of the mixtures were further investigated by scanning electron microscope (SEM), shown in Figure 4-9. The average particle sizes and the range of particle sizes were calculated according to the SEM images, in Figure 4-10. Figure 4-9b shows the particle morphology of the as-received TiC, indicating an agglomeration or cluster of nanometer-scaled TiC particles. The average particle size of the mixture is reduced to about ~ 200 nm after 8 h of cryomilling (Figure 4-9c and Figure 4-10). Some of the particles become smaller and others are aggregated to relatively bigger particles after ball milling to 16 h and 60 h, Figure 4-9d&e. Figure 4-10 also illustrates the slight increase of the mean particle sizes of ( $\text{MgH}_2 + 2\% \text{TiC}$ ) mixture after further 16 h and 60 h ball-milling.

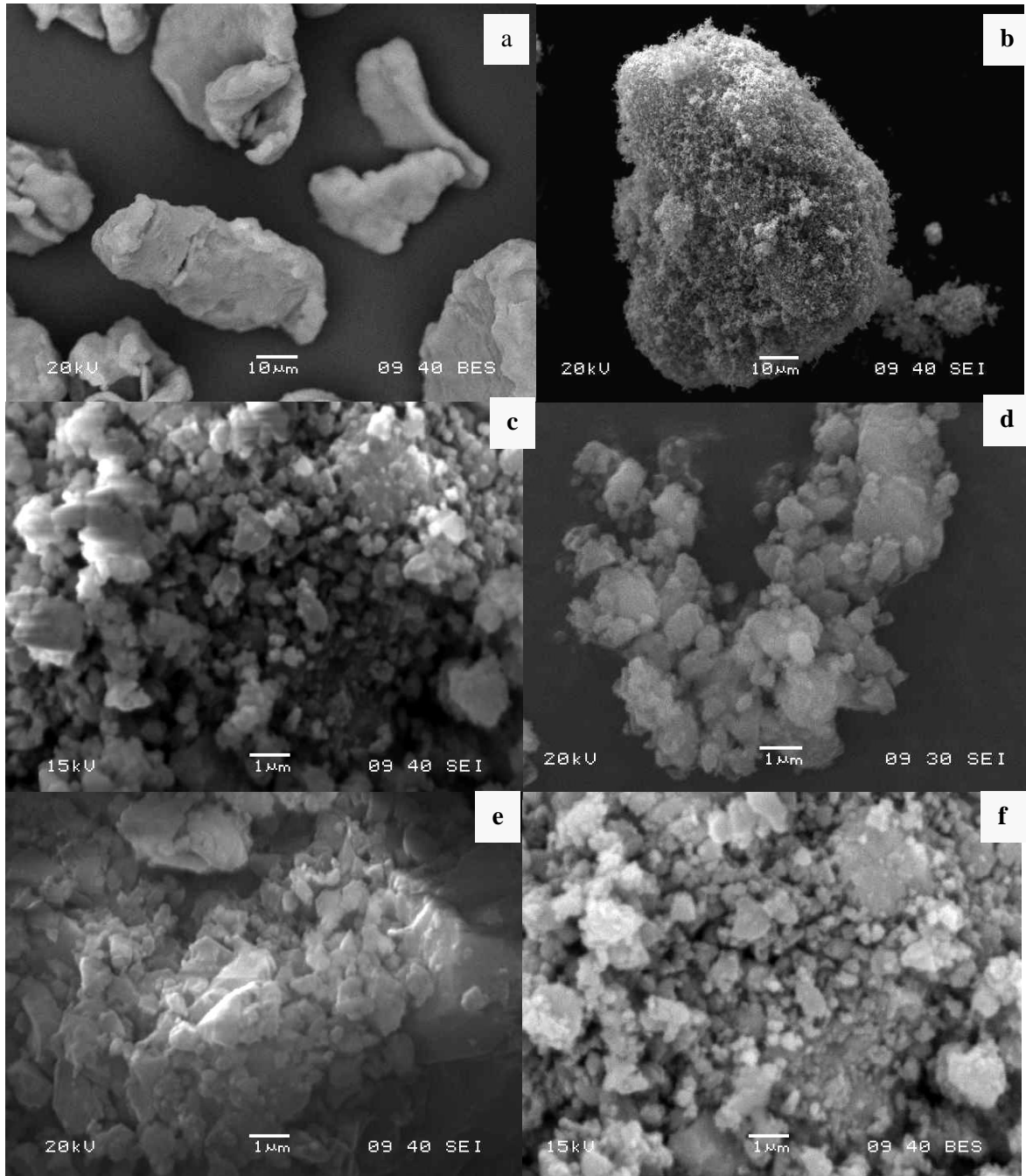


Figure 4-9 SEM micrograph of (a) as-received MgH<sub>2</sub>, (b) as-received TiC, (c) (MgH<sub>2</sub>+2%TiC) cryomilled for 8 h, (d) (MgH<sub>2</sub>+2%TiC) ball milled for 16 h after cryomilling, (e) (MgH<sub>2</sub>+2%TiC) ball milled for 60h after cryomilling and (f) Back Scattering Electron (BSE) image of (MgH<sub>2</sub>+2%TiC) cryomilled for 8h.

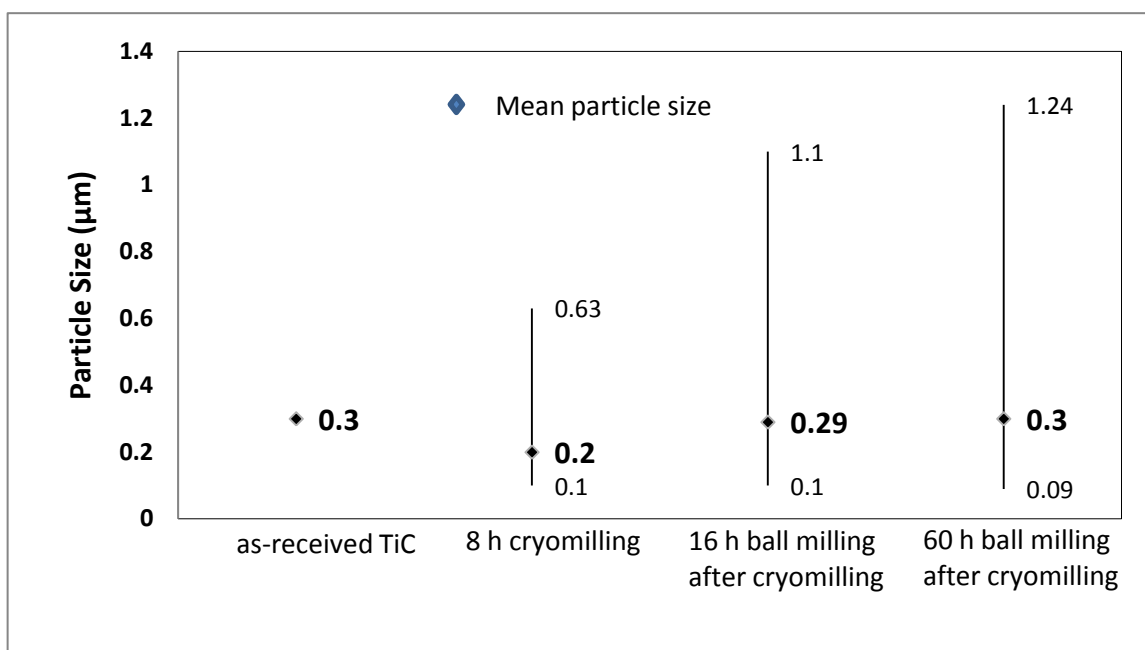


Figure 4-10 Mean particle sizes of the milled ( $\text{MgH}_2+2\%\text{TiC}$ ) mixtures, calculated from SEM images Figure 4-9.

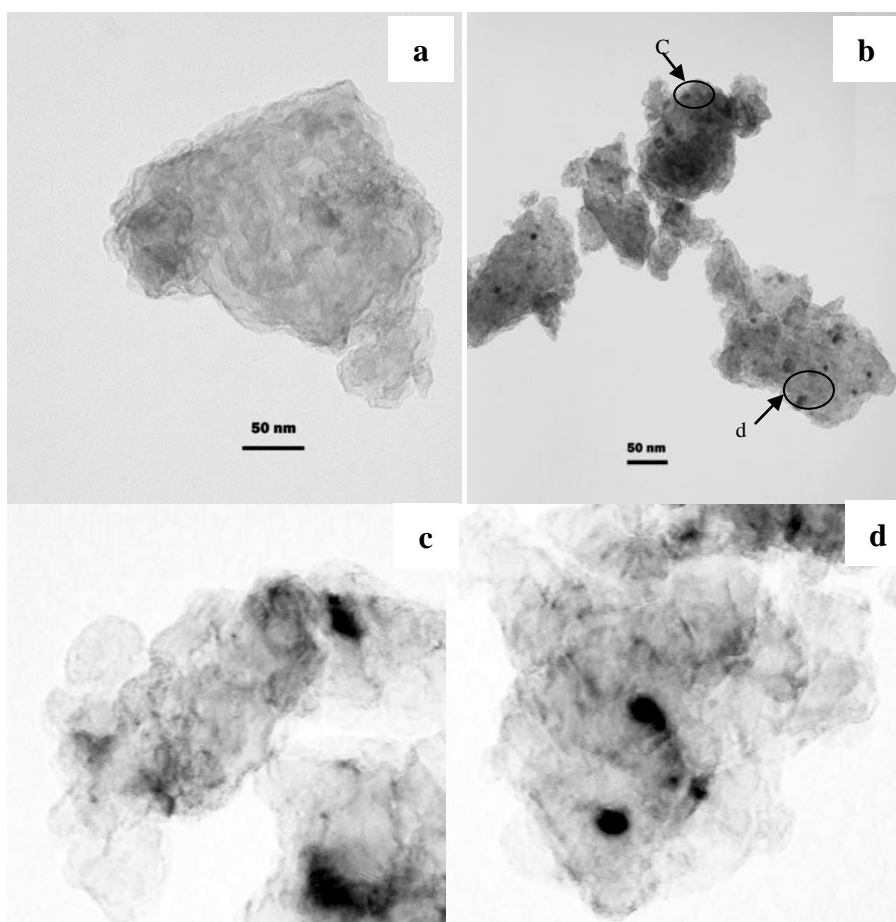


Figure 4-11 TEM images of the samples cryomilled for 8 h and further ball milled for 60 h: (a)  $\text{MgH}_2$  and (b) ( $\text{MgH}_2+\text{TiC}$ ) mixture (c)&(d) partial enlarged view from b.

From the back-scattered electron (BSE) image of the ( $\text{MgH}_2+2\%\text{TiC}$ ) cryomilled for 8h, Figure 4-9f, the BSE signals for the heavier element or the compound containing heavier element should be observed as much brighter spots. However, the contrast between the elements is not recognized. Therefore, it is concluded that the distribution of nano-sized TiC particles in the mixture ( $<100\text{nm}$ ) cannot be detected by the SEM-BSE analysis with a resolution in the micrometer scale.

TEM was performed to identify how the TiC particles are distributed on the surface of  $\text{MgH}_2$  in a nanometer scale. Figure 4-11 shows the TEM images of the  $\text{MgH}_2$  cryomilled for 8 h and the ( $\text{MgH}_2+\text{TiC}$ ) mixture cryomilled for 8 h and further ball-milled for 60 h, where the average size of the large particles is estimated to be about 200-400 nm in diameter. There are many much darker small particles distributed on the large particles, from Figure 4-11 b. By comparing Figure 4-11 a and Figure 4-11 b, the large bright particles are identified as  $\text{MgH}_2$  and the tiny dark particles as TiC. The particle size of TiC is estimated to be 10 ~ 20 nm. The Figure 4-11 c and d are partial enlarged images from Figure 4-11 b, which clearly reveal the grain boundaries and TiC particles. From the above observations, the nano-sized TiC particles are either distributed on the surface of  $\text{MgH}_2$  particles or inserted between grains of  $\text{MgH}_2$ , which enhances the interaction between  $\text{MgH}_2$  and TiC which could act as an effective catalyst or nucleation sites for  $\text{H}_2$  sorption, hence lead to fast kinetics.

### 4.2.2 Dehydrogenation of milled mixtures of MgH<sub>2</sub> and TiC

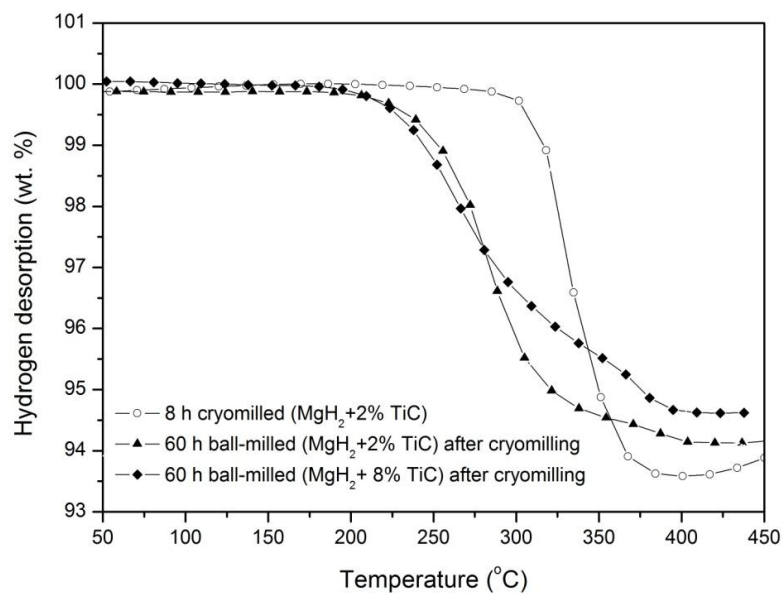


Figure 4-12 Thermogravimetric (TG) curves of the MgH<sub>2</sub> milled with TiC, measured at 1 bar He pressure with a heating rate of 10 K/min.

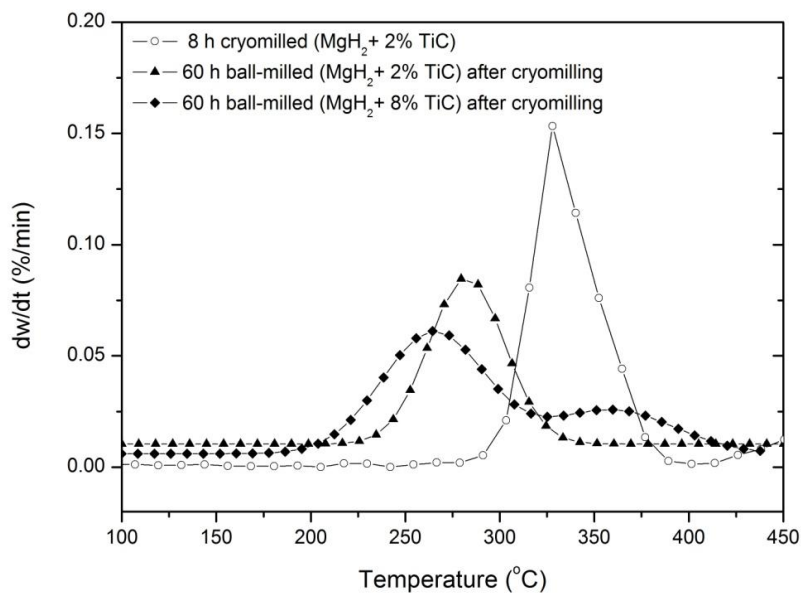


Figure 4-13 Derivative thermogravimetric (DTG) curves of the MgH<sub>2</sub> milled with TiC, derived from Figure 4-12.

Table 4-2 Onset & Peak desorption temperatures and absorption rates of the MgH<sub>2</sub> catalyzed by TiC.

Sample	As-received MgH <sub>2</sub>	cryomilled (MgH <sub>2</sub> + 2%TiC)	60 h ball-milled (MgH <sub>2</sub> + 2%TiC) after cryomilling	60 h ball-milled (MgH <sub>2</sub> + 8%TiC) after cryomilling
Grain Size (nm) of MgH <sub>2</sub>	65 ± 5	27 ± 3	23 ± 3	20 ± 3
Mean Particle Size (µm)	30 ± 2	0.2 ± 0.02	0.29 ± 0.02	0.3 ± 0.02
T <sub>Onset</sub> ( °C)	418	280	190	175
T <sub>Peak</sub> ( °C)	434	332	275	264
E' (KJ/mol)*	235 ± 10	157	104	89
Absorption Rate (wt. %/min)	0.008 ± 0.00004	0.08 ± 0.0001	0.12 ± 0.0001	–

\* Activation energy calculated from Equation 3-8.

Figure 4-12 and Figure 4-13 show the thermogravimetric (TG) and derivative thermogravimetric (DTG) curves of hydrogen desorption of the mixtures, respectively. The total relative weight loss of as-received MgH<sub>2</sub> and (MgH<sub>2</sub>+2 % TiC) is about 7 ± 0.02 wt. % and 6.5 ± 0.02 wt. %, respectively. The 0.5 ± 0.02 wt. % loss is due to the addition of TiC since the theoretical capacity of H<sub>2</sub> storage is 7.3 ± 0.02 wt. % for (MgH<sub>2</sub>+2 mol% TiC) and 7.6 ± 0.02 wt. % for pure MgH<sub>2</sub>. 8 mol % TiC was mixed with MgH<sub>2</sub> following the same synthesized process of (MgH<sub>2</sub>+2 mol% TiC) mixture. 5.5 ± 0.02 wt. % of hydrogen is released from 60 h ball-milled (MgH<sub>2</sub>+ 8 mol% TiC) mixture after 8 h cryomilling owing to 6.4 ± 0.02 wt. % theoretical H<sub>2</sub> capacity. The difference between the observed value and the theoretical value of hydrogen releasing is due to the formation of MgO during the long time milling.

DTG curves of dehydrogenation for the milled mixtures are calculated to identify the onset and peak desorption temperatures. For 8 h cryomilled samples, (MgH<sub>2</sub>+ 2 mol% TiC) mixture starts H<sub>2</sub> desorption at 280 °C (lower than onset temperature of cryomilled MgH<sub>2</sub>, 320 °C), the peak temperature is decreased to 332 °C from 362 °C (the peak temperature of cryomilled MgH<sub>2</sub> without TiC). After a further 60 h ball-milling of cryomilled (MgH<sub>2</sub>+2 mol% TiC), the onset temperature is reduced to 190 °C due to the smaller grain size and enhanced

interaction between TiC and MgH<sub>2</sub>. For the 60 h ball-milled MgH<sub>2</sub> without TiC, the onset temperature was 305 °C, Figure 4-4. The 8 mol% TiC-doped MgH<sub>2</sub> shows a lower onset and peak temperature, 175 °C and 264 °C, respectively. Thus the hydrogen desorption temperature decreases with increasing TiC content. The catalytic effect of TiC is particularly important in reducing the decomposition temperature of MgH<sub>2</sub>, being more marked in the starting desorption temperature.

The overall activation energy ( $E'$ ) of H<sub>2</sub> desorption of the samples is obtained according to Equation 3-8, as shown in Table 4-2. The activation energy of desorption is as high as  $235 \pm 10$  kJ/mol for as-received MgH<sub>2</sub>. When 2 mol % TiC nanoparticles are added, the value is decreased to  $157 \pm 9$  kJ/mol after 8 h cryomilling. With further ball milling for 60 h after cryomilling, the activation energy falls as low as  $104 \pm 6$  kJ/mol. Thus the desorption kinetics can be improved greatly by the catalytic action of TiC nanoparticles. Milled MgH<sub>2</sub> with a content of 8 mol % TiC requires less activation energy of  $89 \pm 5$  kJ/mol to release hydrogen, shown in Figure 4-14 and Table 4-2. TiC is shown to be an effective catalyst for hydrogen desorption of MgH<sub>2</sub>.

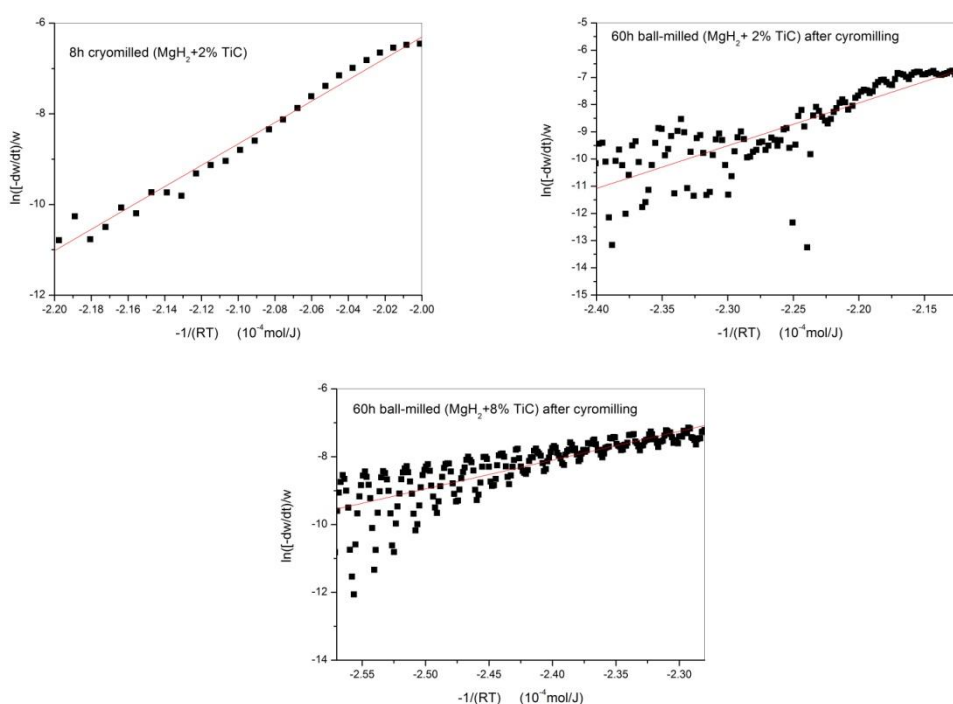


Figure 4-14 Kinetic plots and activation energy of cryomilled and ball-milled (MgH<sub>2</sub>+ 2 %TiC) and ball-milled

### 4.2.3 Hydrogenation of milled mixtures of $\text{MgH}_2$ and TiC

The hydrogen absorption kinetics of the dehydrogenated  $\text{MgH}_2$  and ( $\text{MgH}_2 + 2 \text{ mol. \% TiC}$ ) mixtures were measured under 8 bars  $\text{H}_2$  pressure at 300 °C, Figure 4-15. The hydrogen uptake is very slow for the as-received  $\text{MgH}_2$  after dehydrogenation. However, about 4 wt. % of hydrogen is absorbed in 60 min after cryomilling of  $\text{MgH}_2$ . The mixture of ( $\text{MgH}_2 + 2 \text{ mol \% TiC}$ ) after cryomilling and ball-milling shows faster  $\text{H}_2$  absorption with  $5 \pm 0.02 \text{ wt. \% H}_2$  uptake in 50 min. It was also found that the absorption rate increased to  $0.12 \pm 0.0001 \text{ wt. \% / min}$  due to the milling process and the addition of the catalyst TiC (Table 4-2). The relatively lower maximum weight percentage of  $\text{H}_2$  uptake of cryomilled  $\text{MgH}_2$  and ( $\text{MgH}_2 + 2 \text{ mol \% TiC}$ ) is probably due to slow kinetics and slight oxidation of the samples during milling.

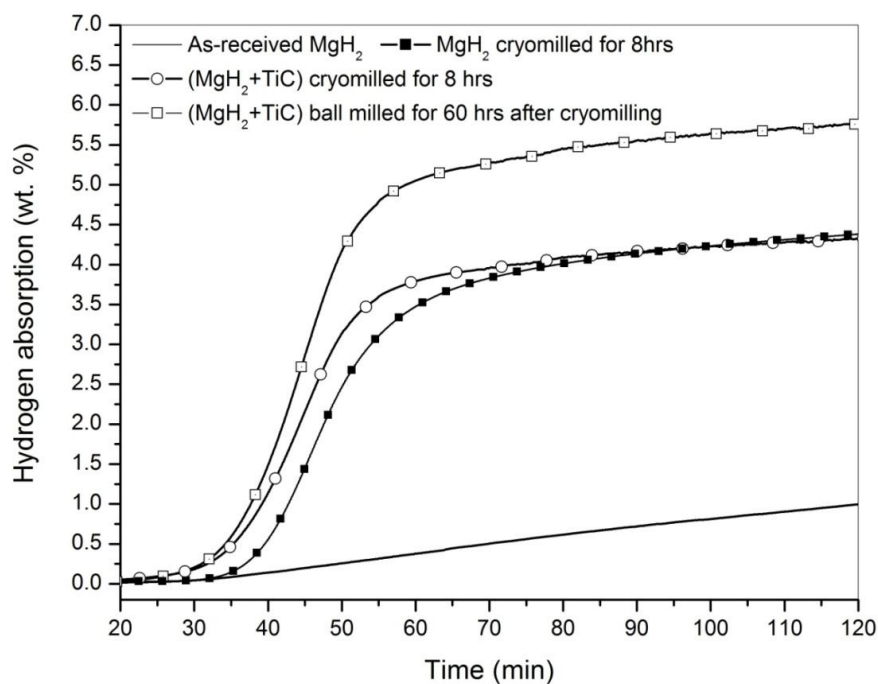


Figure 4-15 Hydrogen absorption curves of the  $\text{MgH}_2$  catalyzed with and without TiC, measured under 8 bar  $\text{H}_2$  pressure at 300 °C.

#### 4.2.4 Summary

Hydrogen storage properties of  $\text{MgH}_2$  catalysed with 2 mol % and 8 mol % TiC by cryomilling and ball-milling were investigated respectively. The crystallite sizes decreased with increasing milling time. TiC, which is a very stable compound at the testing temperature and pressure ( $< 500\text{ }^\circ\text{C}$ , 1 bar), retains its original form during milling and after dehydrogenation. From SEM-BSE and TEM observations, the nano-sized TiC particles were either distributed on the surface of  $\text{MgH}_2$  particles or inserted between grains of  $\text{MgH}_2$ , which enhanced the interaction between  $\text{MgH}_2$  and TiC.

The desorption temperatures and activation energy of the milled  $\text{MgH}_2$  were reduced by the addition of 2 mol% TiC. It was also found that a better desorption performance in terms of temperature and kinetics was recorded with the addition of 8 mol % TiC. TiC shows an effective catalytic property for  $\text{H}_2$  sorption of  $\text{Mg}/\text{MgH}_2$ , which is stable during  $\text{H}_2$  uptake and release with no reaction with Mg or  $\text{MgH}_2$ . Based on the microstructural observations and hydrogen sorption property analysis, it is concluded that the reduction of nano particle size has an positive effect on hydrogen storage properties of  $\text{MgH}_2$ , but TiC as a catalyst is crucially important for the enhancement of hydrogen sorption of  $\text{Mg}/\text{MgH}_2$ .

### 4.3 Effects of $\text{Mo}_2\text{C}$ Nanoparticles on Hydrogen Sorption Properties of $\text{MgH}_2$

More recently, early transition metal carbides have attracted much attention for displaying catalytic properties similar to those of noble metals<sup>167</sup>. It is reported that the increase of effect on hydrogen absorption property seems related to the increase of atomic number (Z) of the transition element<sup>168</sup>. Since TiC shows promising catalytic effect on the hydrogen storage properties of  $\text{MgH}_2$ ,  $\text{Mo}_2\text{C}$  with high thermal stability and low cost is selected as another alternative catalyst for hydrogen storage of  $\text{MgH}_2$  because of the atomic number of molybdenum in the periodic table is larger than titanium. The effect of Mo, W, Nb, etc. on

hydrogen storage properties of metal hydrides has been investigated by K. Iwase *et al.*<sup>169</sup>. Their results indicated that Mo additive delayed the formation of AB<sub>5</sub>-hydride, in accordance with increased hydrogen absorption capacity. The findings together with high thermal stability and low cost, make Mo<sub>2</sub>C an interesting additive to modify the sorption properties of MgH<sub>2</sub>.

The aim of the study is following this point to evaluate the influence of Mo<sub>2</sub>C on hydrogen sorption of MgH<sub>2</sub>, in comparison with the results of TiC in previous section 4.2.

#### 4.3.1 Structural characterizations of milled mixtures of MgH<sub>2</sub> and Mo<sub>2</sub>C

XRD patterns of the samples obtained by milling of MgH<sub>2</sub> with 2 mol % Mo<sub>2</sub>C are shown in Figure 4-16. There were no addition of diffraction peaks detected which suggested new phases or products resulting from cryomilling and ball-milling of (MgH<sub>2</sub>+ Mo<sub>2</sub>C), shown in Figure 4-16b and c. The two main components of β-MgH<sub>2</sub> and Mo<sub>2</sub>C were observed in the milled mixtures. The Fe phase was detected in the ball-milled samples was from the collision of milling vial and balls, which was also found in the MgH<sub>2</sub> and (MgH<sub>2</sub>+ TiC) powders after 60 h ball milling. After a further 60 h ball-milling, γ-MgH<sub>2</sub> was formed, shown in Figure 4-16c. As discussed earlier in section 4.1, a 60 h ball-milling led to broadening of peaks of β-MgH<sub>2</sub>, with the grain size becoming a few nanometers and further reduced with increasing milling. The XRD pattern of the dehydrided 60 h ball-milled (MgH<sub>2</sub>+ Mo<sub>2</sub>C) showed the Mg phase and Mo<sub>2</sub>C phase. There was no reaction during dehydrogenation of (MgH<sub>2</sub>+ Mo<sub>2</sub>C).

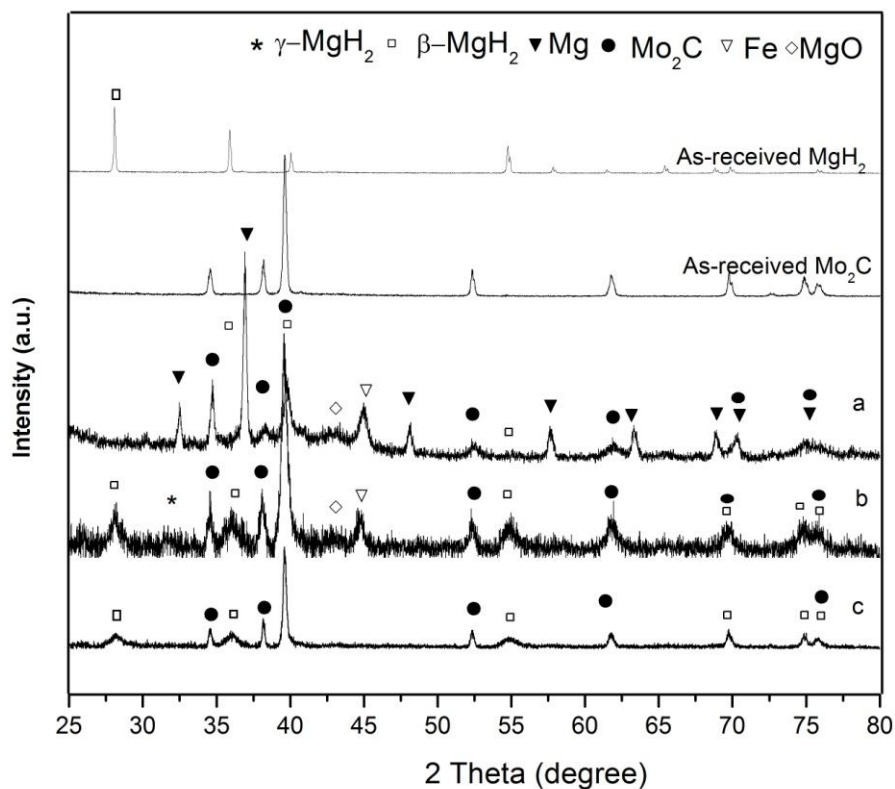


Figure 4-16 XRD patterns of the as-received  $\text{MgH}_2$ ,  $\text{Mo}_2\text{C}$  and milled ( $\text{MgH}_2 + \text{Mo}_2\text{C}$ ) mixtures. (a) Dehydrogenated ( $\text{MgH}_2 + \text{Mo}_2\text{C}$ ) after cryomilling and 60 h ball-milling, (b) ( $\text{MgH}_2 + \text{Mo}_2\text{C}$ ) ball milled for 60 h after cryomilling, (c) ( $\text{MgH}_2 + \text{Mo}_2\text{C}$ ) cryomilled for 8 h.

Figure 4-17 shows estimates of the nanograin size of as-received  $\text{MgH}_2$  and  $\text{Mo}_2\text{C}$  calculated from XRD patterns to be of the order of 65 nm and 30 nm. After 8 h cryogenic milling, the grain size of  $\text{MgH}_2$  has decreased greatly to  $27 \pm 3$  nm. Following a further 60 h ball milling, the grain size of  $\text{MgH}_2$  was only reduced slightly to  $20 \pm 3$  nm. The grain size of  $\text{Mo}_2\text{C}$  was decreased from  $31 \pm 3$  nm to  $18 \pm 3$  nm during 60 h ball milling. It can be seen that the grain size of  $\text{MgH}_2$  with or without  $\text{Mo}_2\text{C}$  is similar, which is only relevant to the duration time of cryomilling and ball-milling, comparing with the results from section 4.1 (Table 4-1).

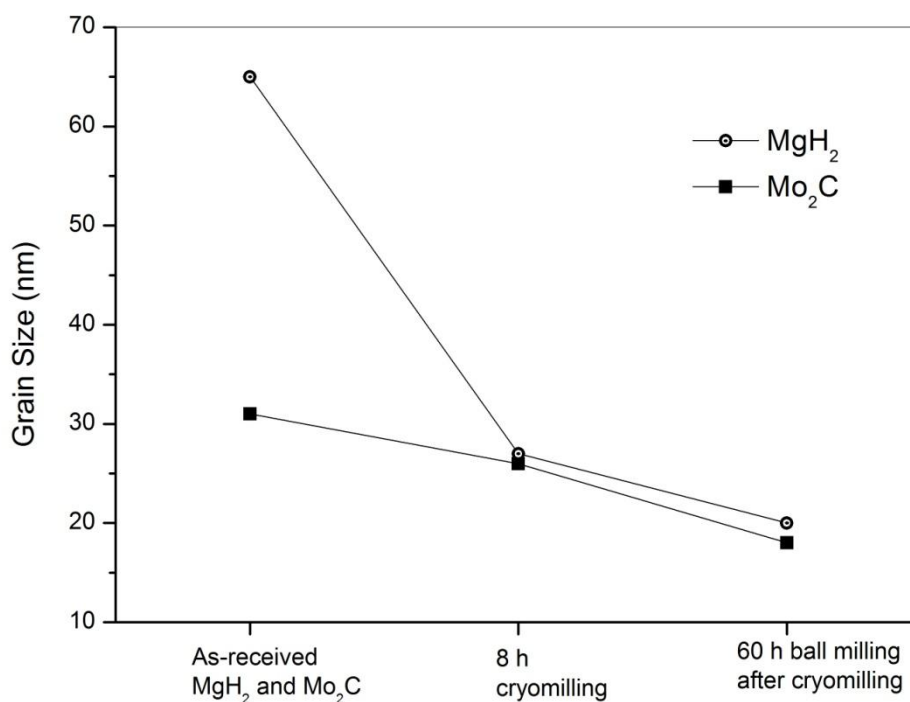


Figure 4-17 Grain sizes of MgH<sub>2</sub> and Mo<sub>2</sub>C before and after milling, calculated from XRD patterns of the as-received MgH<sub>2</sub>, Mo<sub>2</sub>C and the milled (MgH<sub>2</sub>+ Mo<sub>2</sub>C) mixtures.

The as-received Mo<sub>2</sub>C particles have a platelet-like shape with the mean size of ~1.3 μm in diameter, seen in Figure 4-18 and Figure 4-19. After 8 h cryomilling, the average particle size of the (MgH<sub>2</sub>+Mo<sub>2</sub>C) is reduced to about 440 nm with irregular morphology. As shown in Figure 4-19, the particle size distribution after 60 h ball-milling becomes broader compared with that of only 8 h cryomilling. The smaller particle size range could reach to 60 nm.

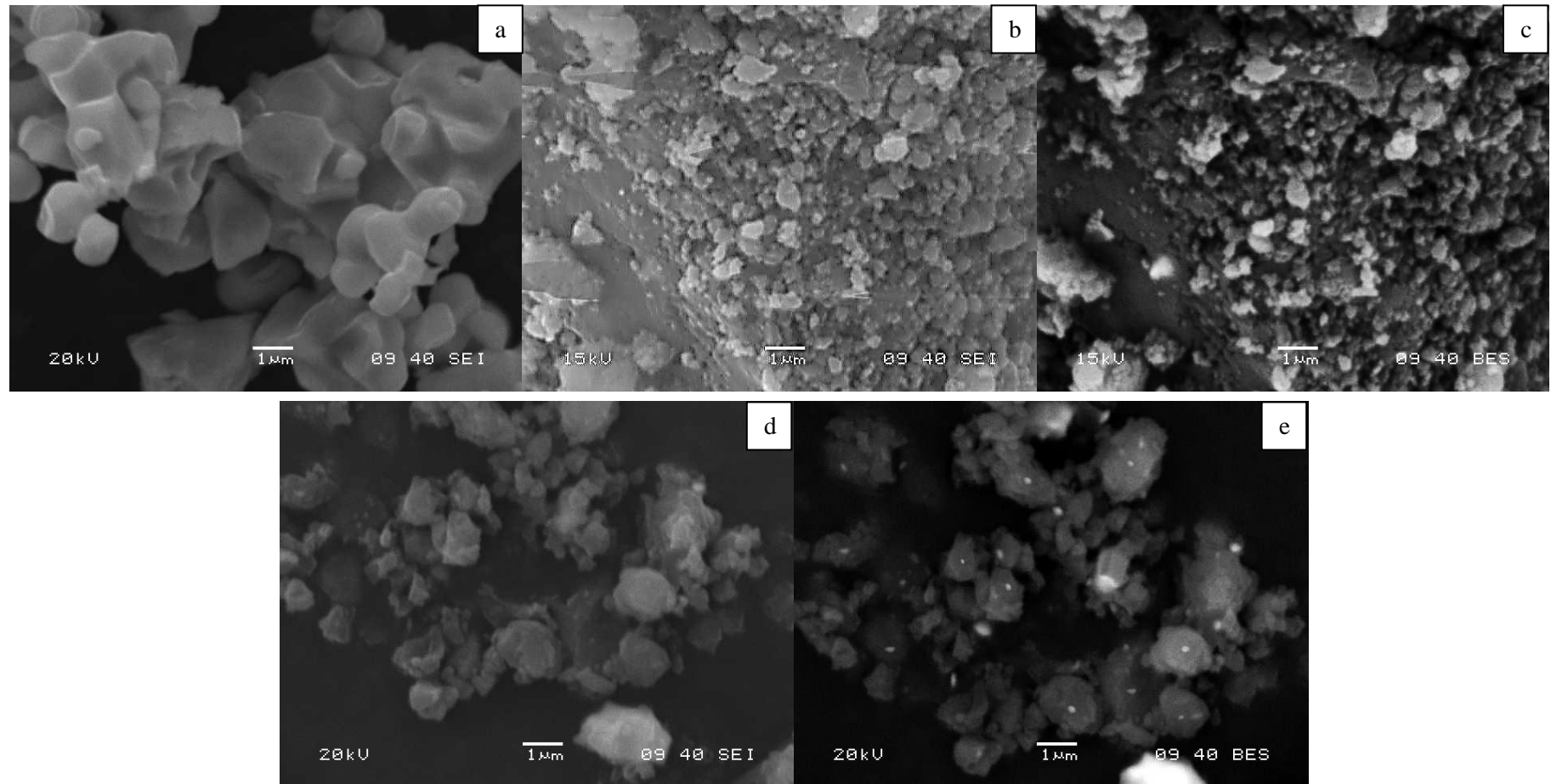


Figure 4-18 SEM micrographs of (a) as-received  $\text{Mo}_2\text{C}$ , (b) 8 h cryomilled ( $\text{MgH}_2+2\text{mol}\% \text{Mo}_2\text{C}$ ), (c) BSE of cryomilled ( $\text{MgH}_2+2\text{mol}\% \text{Mo}_2\text{C}$ ), (d) 60 h ball-milled ( $\text{MgH}_2+2\text{mol}\% \text{Mo}_2\text{C}$ ) after cryomilling, and (e) BSE of ball-milled ( $\text{MgH}_2+2\text{mol}\% \text{Mo}_2\text{C}$ )

From a back-scattered electron (BSE) image of the ( $\text{MgH}_2 + \text{Mo}_2\text{C}$ ) cryomilled for 8 h, in Figure 4-18 c, the bright small particles were distributed over the dark particles, which can also be observed in the BSE image of 60 h ball-milled ( $\text{MgH}_2 + \text{Mo}_2\text{C}$ ) after 8 h cryomilling, Figure 4-18(g). The bright particles/area are the distribution of  $\text{Mo}_2\text{C}$  particles, because the BSE signals for heavier element or compound containing the heavier element should have brighter images. Mo has a much larger atomic number than Mg. The observation indicates that the  $\text{Mo}_2\text{C}$  particles homogeneously distribute in such a micrometer scale range on the surface of  $\text{MgH}_2$ .

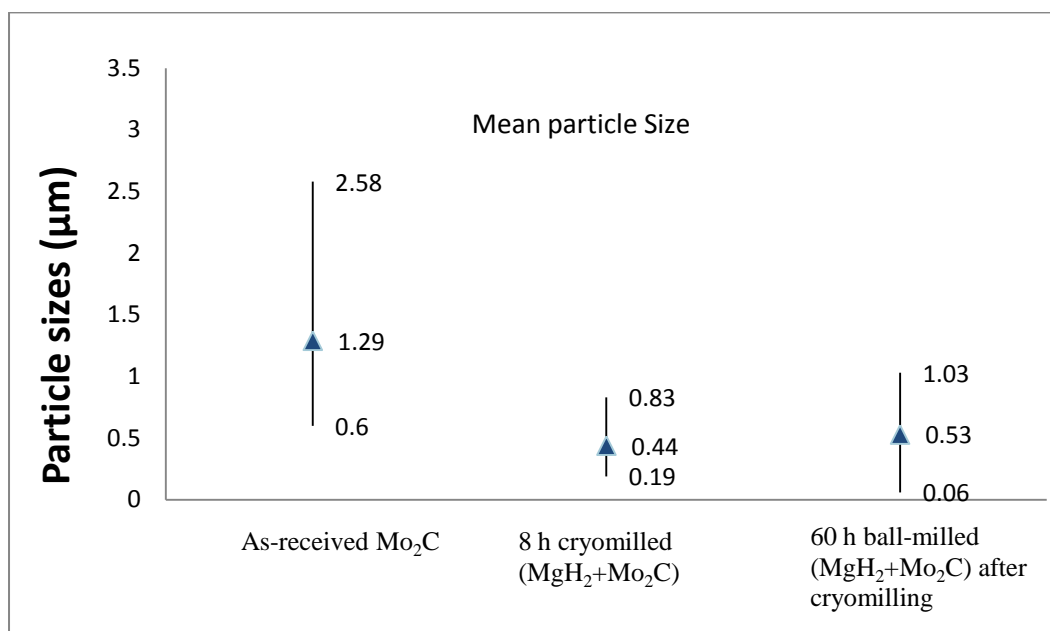


Figure 4-19 Mean particle sizes of the milled ( $\text{MgH}_2 + \text{Mo}_2\text{C}$ ), calculated from the SEM images Figure 4-18.

### 4.3.2 Dehydrogenation of milled mixtures of $\text{MgH}_2$ and $\text{Mo}_2\text{C}$

The TG and DTG curves show  $6 \pm 0.02$  % weight loss of cryomilled ( $\text{MgH}_2 + \text{Mo}_2\text{C}$ ) and 60 h ball-milled ( $\text{MgH}_2 + \text{Mo}_2\text{C}$ ), with the starting desorption temperature of  $320$  °C and  $300$  °C respectively, as shown in Figure 4-20, Figure 4-21 and Table 4-3. Comparing with the onset temperatures of the cryomilled  $\text{MgH}_2$  ( $320$  °C) and 60 h ball-milled  $\text{MgH}_2$  after cryomilling ( $305$  °C), the desorption temperature of milled ( $\text{MgH}_2 + \text{Mo}_2\text{C}$ ) mixture show almost no

reduction. Therefore  $\text{Mo}_2\text{C}$  didn't have an obvious effect on the dehydrogenation temperature of  $\text{MgH}_2$ . From Table 4-3, it is indicated that the activation energy of ( $\text{MgH}_2 + \text{Mo}_2\text{C}$ ) ball milled for 60 h after cryomilling is  $167 \pm 9$  kJ/mol, lower than that of 60 h ball-milled  $\text{MgH}_2$  (199 kJ/mol, Table 4-1) and higher than that of 60 h ball-milled ( $\text{MgH}_2 + 2\% \text{TiC}$ ) (104 kJ/mol, Table 4-2). It is in accordance with desorption onset temperature of ( $\text{MgH}_2 + \text{Mo}_2\text{C}$ ),  $\text{MgH}_2$  and ( $\text{MgH}_2 + 2\% \text{TiC}$ ), which are 300 °C, 305 °C and 190 °C respectively.

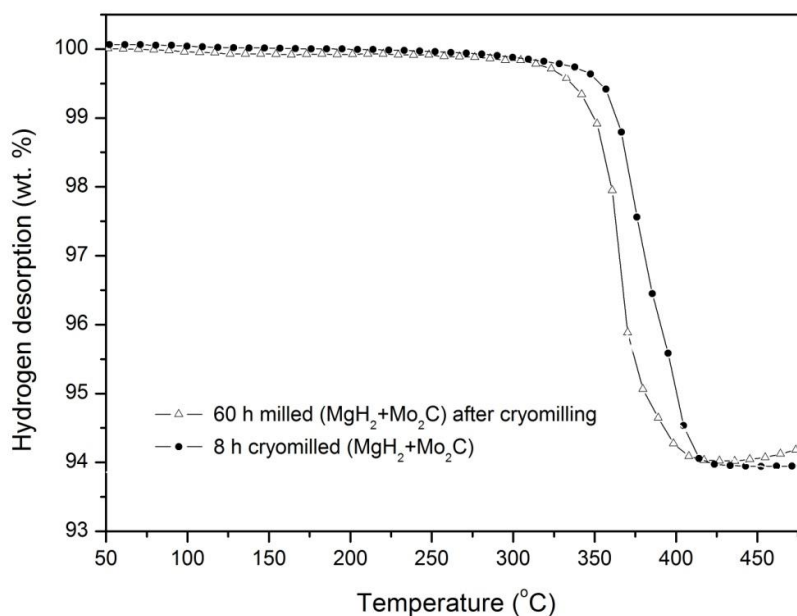


Figure 4-20 Thermogravimetric (TG) curves of  $\text{MgH}_2$  milled with  $\text{Mo}_2\text{C}$ , measured at 1 bar He pressure with a heating rate of 10 K/min.

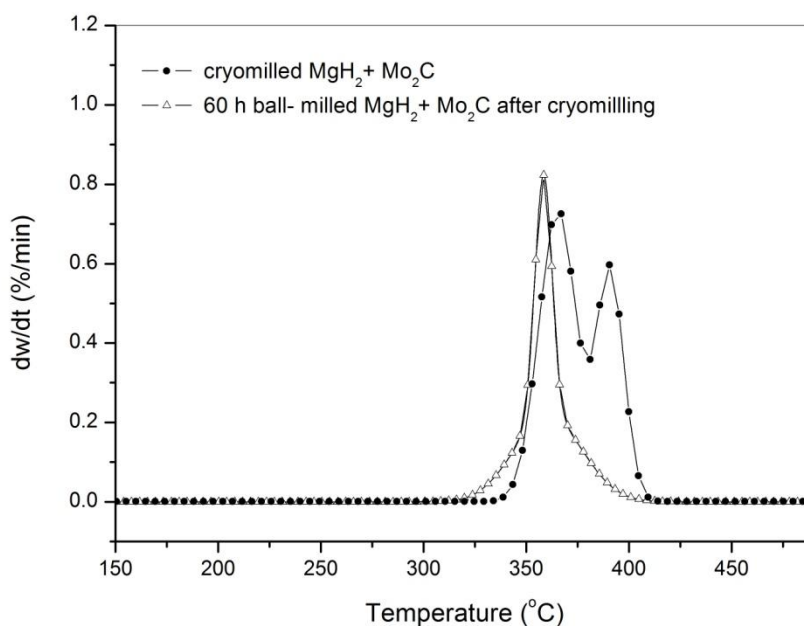


Figure 4-21 Derivative thermogravimetric (DTG) curves of the  $\text{MgH}_2$  milled with  $\text{Mo}_2\text{C}$ , derived from Figure 4-20.

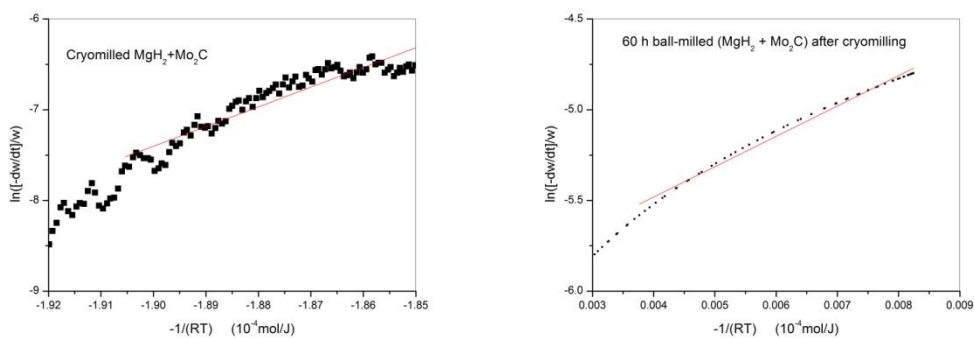


Figure 4-22 Kinetic plots and activation energy of cryomilled and ball-milled ( $\text{MgH}_2 + \text{Mo}_2\text{C}$ ), based on Figure 4-21 and Equation 3-8.

Table 4-3 Onset & Peak desorption temperatures and absorption rates for the  $\text{MgH}_2$  catalyzed with  $\text{Mo}_2\text{C}$ .

Sample	cryomilled ( $\text{MgH}_2 + \text{Mo}_2\text{C}$ )	60 h ball-milled ( $\text{MgH}_2 + \text{Mo}_2\text{C}$ ) after cryomilling
$T_{\text{Onset}}$ (°C)	320	300
$T_{\text{Peak}}$ (°C)	360	358
$E'$ (KJ/mol)	$217 \pm 10$	$167 \pm 9$

<b>Absorption Rate</b>	$0.074 \pm 0.0001$ (40-60 min)	$0.074 \pm 0.0001$ (40-60 min)
<b>(<math>\Delta</math> wt. %/min)</b>	$0.021 \pm 0.0001$ (60-180 min)	$0.023 \pm 0.0001$ (60-180 min)

### 4.3.3 Hydrogen absorption of milled mixtures of $\text{MgH}_2$ and $\text{Mo}_2\text{C}$

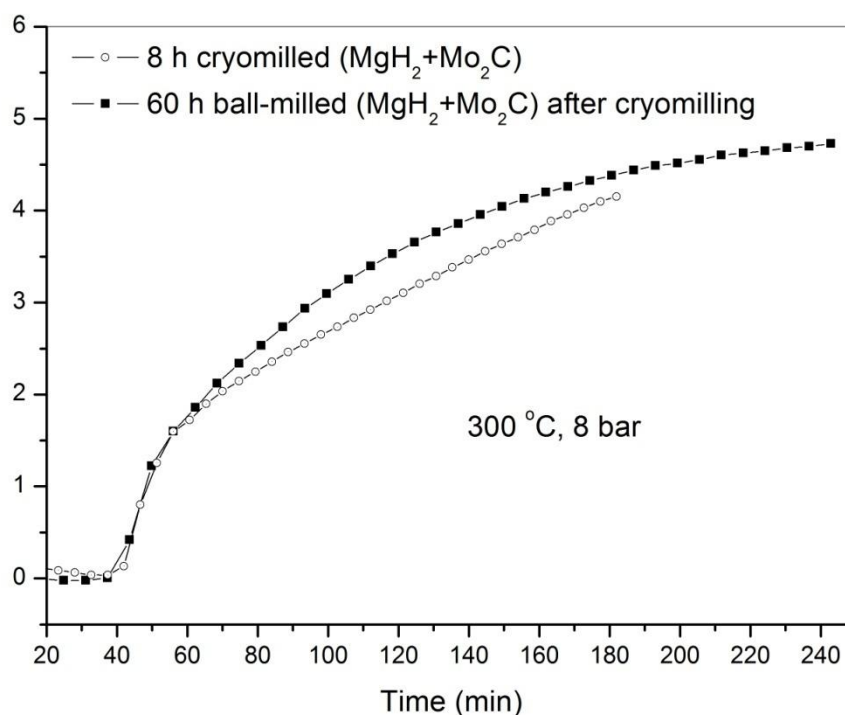


Figure 4-23 Hydrogen absorption of  $\text{MgH}_2$  catalyzed by  $\text{Mo}_2\text{C}$ , measured under 8 bar  $\text{H}_2$  pressure at 300 °C.

Figure 4-23 shows the hydrogen absorption of  $(\text{MgH}_2+\text{Mo}_2\text{C})$  mixture. The dehydrided 8 h cryomilled  $(\text{MgH}_2+\text{Mo}_2\text{C})$  can absorb  $4.1 \pm 0.02$  wt. % hydrogen in 180 min at 300 °C at 8 bar  $\text{H}_2$  pressure, which included two steps: hydriding with the speed of  $0.074 \pm 0.0001$  wt.%/min from 40 min to 60 min, and then the decreased rate of  $0.021 \pm 0.0001$  wt.%/min from 60 min to 180 min ( in Table 4-3). The absorption curve was continuously increasing after 180 min, which indicates that the hydrogenation was incomplete in 180 min due to slow absorption kinetics. The absorption rate was slightly improved for dehydrided 60 h ball-milled  $(\text{MgH}_2+\text{Mo}_2\text{C})$  after cryomilling. The adsorption reached a certain value of  $4.5 \pm 0.02$  wt. % in 240 min.  $\text{Mo}_2\text{C}$  has little effect on improving the absorption kinetics of

Mg/MgH<sub>2</sub> under the present testing conditions. Furthermore, it can be observed the absorption rate of dehydrided ball-milled (MgH<sub>2</sub>+Mo<sub>2</sub>C) is lower than that of 60 h ball-milled MgH<sub>2</sub> ( $0.1 \pm 0.0001 \Delta\text{wt. \%}/\text{min}$ , Table 4-1) because the Mo<sub>2</sub>C particles were dispersed on the surface of Mg/MgH<sub>2</sub> particles to block the interaction between Mg and H.

#### 4.3.4 Summary

XRD results indicate that no reaction happened during milling and dehydrogenation of (MgH<sub>2</sub>+Mo<sub>2</sub>C). The grain sizes of MgH<sub>2</sub> and Mo<sub>2</sub>C are decreased greatly after 8 h cryomilling.

SEM-BSE characterizations showed that some micro-scaled Mo<sub>2</sub>C particles of less than  $500 \pm 20$  nm were distributed onto MgH<sub>2</sub> particles.

Comparing the TG and DTG results of MgH<sub>2</sub> with Mo<sub>2</sub>C, the onset and peak temperatures have not been reduced, which is coinciding with the results of the activation energy. The absorption kinetics of dehydrided MgH<sub>2</sub> doped with Mo<sub>2</sub>C is even lower than that dehydrided MgH<sub>2</sub> without Mo<sub>2</sub>C under the same milling process and conditions. Thus it is concluded that the Mo<sub>2</sub>C shows no catalytic effect on hydrogen sorption of MgH<sub>2</sub>.

#### 4.4 Effects of Ni Nanoparticles on Hydrogen Desorption Properties of 60 h Ball-milled (MgH<sub>2</sub> +TiC or Mo<sub>2</sub>C)

Nickel (Ni) is a very effective catalyst to improve hydrogen sorption kinetics of MgH<sub>2</sub><sup>18, 170-173</sup>. Hanada et al. have suggested that nanoparticles transition-metal such as Fe, Co, Cu and Ni can enhance the kinetics dramatically<sup>174</sup>. After milling with 2 mol% Ni nanoparticles for a short time of 15 min under a slow milling speed of 200 rpm, a large amount of hydrogen ( $6.5 \pm 0.02$  wt%) was desorbed in the temperature range 423 to 523 K at a heating rate of 5 K/min under He gas flow.

In this section, 60 h ball-milled ( $\text{MgH}_2 + 2 \text{ mol.}\% \text{TiC/Mo}_2\text{C}$ ) after 8 h cryomilling was mixed with 2 mol.% Ni nanoparticles for 15 min to investigate the synergetic effect of the addition on hydrogen sorption of the mixture.

#### 4.4.1 Structural characterizations of ( $\text{MgH}_2 + \text{TiC/Mo}_2\text{C} + 2 \text{ mol.}\% \text{Ni}$ ) mixtures

Figure 4-24 presents the XRD patterns of prepared samples. After mixing, the 60 h ball-milled ( $\text{MgH}_2 + \text{TiC/Mo}_2\text{C}$ ) with Ni nanoparticles, the main phases were not changed. There was no new compound, such as  $\text{Mg}_2\text{NiH}_4$ , formed during the short milling time. The Ni peaks were well presented in the XRD patterns. Determined by the Sherrer equation, the crystallite sizes of  $\text{MgH}_2$ ,  $\text{TiC/Mo}_2\text{C}$  and Ni nanoparticles in the mixtures are almost the same as those of the 60 h ball-milled samples without mixing with Ni due to the mild milling condition.

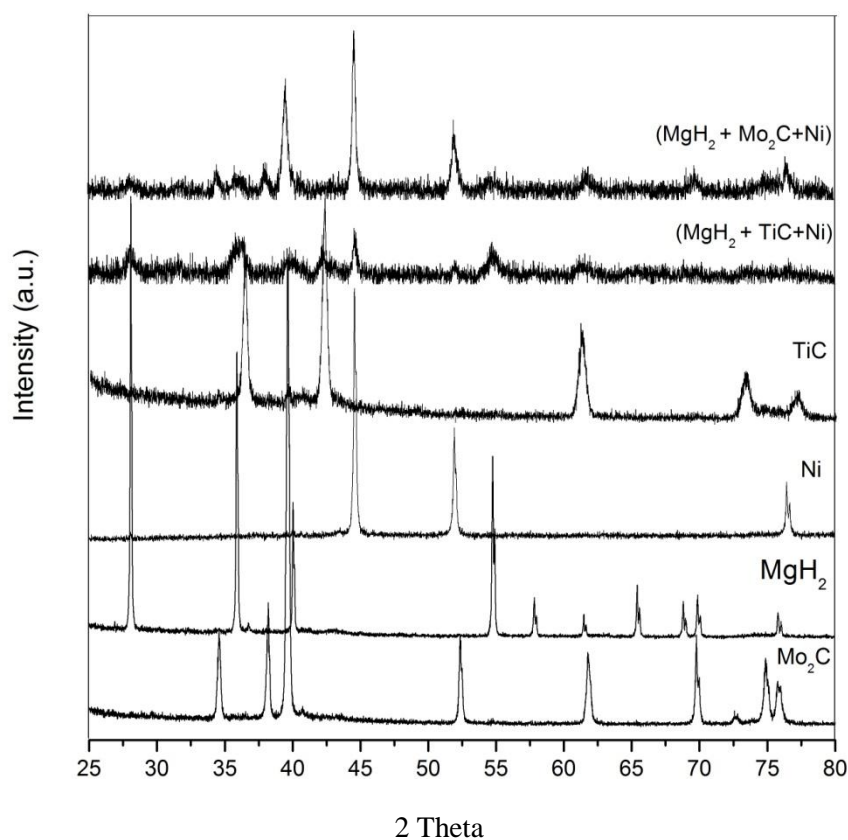


Figure 4-24 XRD patterns of the as-received  $\text{MgH}_2$ ,  $\text{TiC}$ ,  $\text{Mo}_2\text{C}$ ,  $\text{Ni}$ ,  $(\text{MgH}_2 + \text{Mo}_2\text{C} + \text{Ni})$  and  $(\text{MgH}_2 + \text{TiC} + \text{Ni})$

Figure 4-25 shows that the particle size and morphology of the ( $\text{MgH}_2+\text{Mo}_2\text{C}+\text{Ni}$ ) remained almost the same as the 60 h ball-milled ( $\text{MgH}_2+\text{Mo}_2\text{C}$ ) after cryomilling, as discussed in section 4.3. From

Figure 4-26 and Figure 4-27, the mean particle size of the 60 h ball-milled ( $\text{MgH}_2+\text{TiC}+\text{Ni}$ ) increased slightly. From the BSE image of the ( $\text{MgH}_2+\text{TiC}+\text{Ni}$ ), the Ni could not be investigated due to the very small size of Ni nanoparticles.

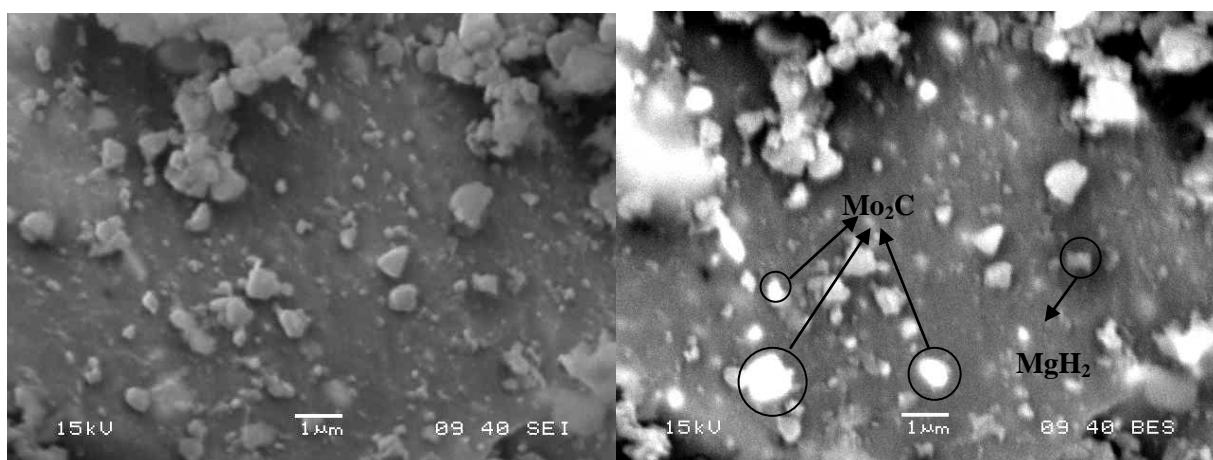


Figure 4-25 SEM-BSE images of ( $\text{MgH}_2+\text{Mo}_2\text{C}+\text{Ni}$ )

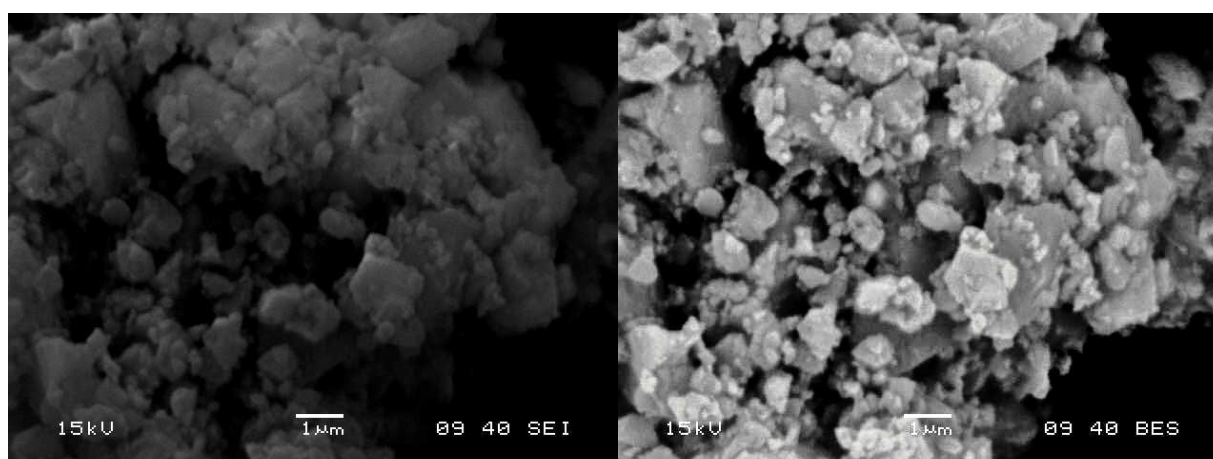


Figure 4-26 SEM-BSE images of ( $\text{MgH}_2+\text{TiC}+\text{Ni}$ )

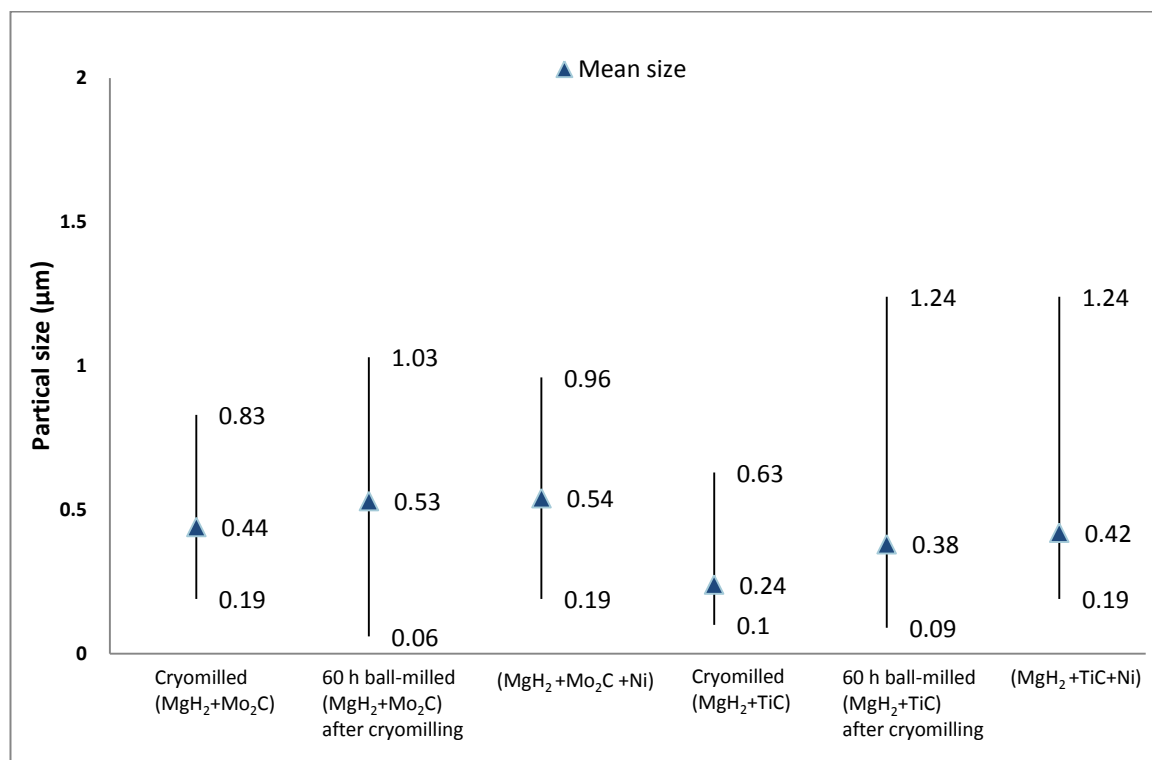


Figure 4-27 Comparison of mean particle size of the milled samples

#### 4.4.2 Dehydrogenation of milled mixtures of MgH<sub>2</sub> and catalysts

The hydrogen desorption performance of the samples was investigated by thermal analysis at 10 k/min from room temperature to 500 °C under helium atmosphere, as seen in Figure 4-28. The temperatures corresponding to desorption peaks are presented in DTG curves of the mixtures, Figure 4-29. The starting desorption temperature of the 60 h ball-milled MgH<sub>2</sub> with Ni for 15 min without carbides is 195 °C, similar to that of (MgH<sub>2</sub>+TiC+Ni), 190 °C, whereas the onset temperature of (MgH<sub>2</sub>+Mo<sub>2</sub>C+Ni) is higher, 240 °C. The peak temperatures of (MgH<sub>2</sub>+TiC+Ni), (MgH<sub>2</sub>+Ni) and (MgH<sub>2</sub>+ Mo<sub>2</sub>C+Ni) are 282 °C, 301 °C and 328 °C respectively. From Figure 4-12 and Figure 4-13, the onset and peak temperature of 60 h ball-milled (MgH<sub>2</sub>+2% TiC) without Ni are 190 °C and 275 °C respectively, which are slightly lower than (MgH<sub>2</sub>+ TiC+Ni). The possible reasons are: firstly, the mean particle size of (MgH<sub>2</sub>+TiC+Ni) is 0.42 ± 0.02 µm, slightly bigger than that of (MgH<sub>2</sub>+TiC), 0.38 ± 0.02 µm; in addition, it is suggested that the Ni nanoparticles were dispersed on the surface

of  $\text{MgH}_2$  with the short milling process. The catalytic effect on the inner phase transformation and growth is limited. According to the discussion in section 4.2, some TiC nanoparticles are inserted into the inner space or grain boundary of  $\text{MgH}_2$  particles. It proves that TiC is a very effective catalyst on improving the hydrogen desorption kinetics of  $\text{MgH}_2$ , and possibly have better performance than Ni in terms of efficiency and stability.

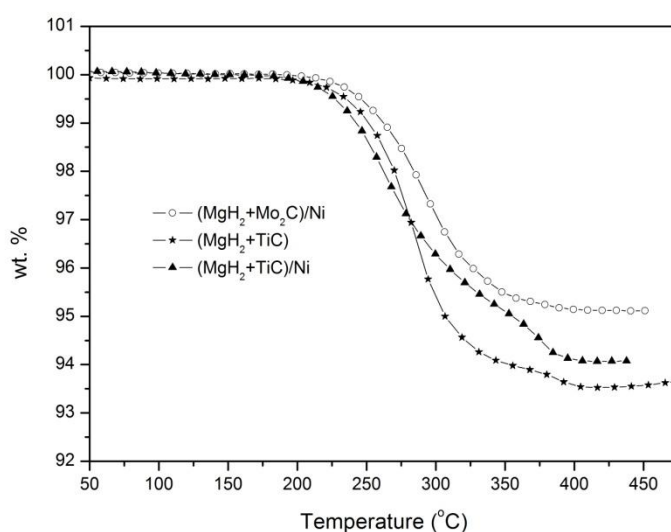


Figure 4-28 TG curves of the milled samples with Ni

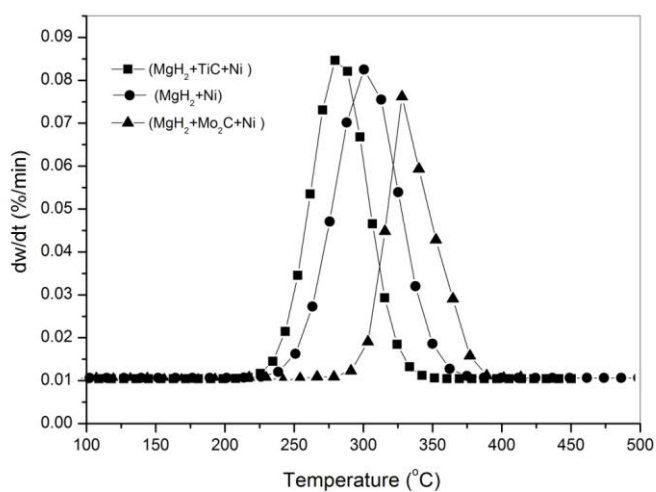


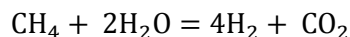
Figure 4-29 DTG curves of the milled samples with Ni, derived from Figure 4-28

#### 4.4.3 Summary

Mixing of 60 h ball-milled ( $\text{MgH}_2 + \text{Mo}_2\text{C}$ ) with Ni for 15 min reduces the hydrogen desorption temperature of  $\text{MgH}_2$ . However, the 60 h ball-milled ( $\text{MgH}_2 + \text{TiC}$ ) without Ni has more effective catalysis on hydrogen desorption of  $\text{MgH}_2$  than ( $\text{MgH}_2 + \text{TiC} + \text{Ni}$ ), because 60 h ball-milled ( $\text{MgH}_2 + \text{TiC}$ ) get the finer nanoparticle size of catalysts and the TiC nanoparticles are inserted into the grain boundary or inner space of  $\text{MgH}_2$ . Experimental results show that TiC has better performance in improving hydrogen desorption kinetics of  $\text{MgH}_2$ .

## 4.5 Effects of Selected Gas Mixture of (H<sub>2</sub> + CO<sub>2</sub>) on Hydrogen Sorption of MgH<sub>2</sub>

One of the current common hydrogen production methods is steam re-forming of natural gas<sup>175, 176</sup>, which can be represented by the following reaction



Hydrogen produced during this process is accompanied by about 20% CO<sub>2</sub> and some CO. To obtain pure hydrogen for fuel cell application, H<sub>2</sub> separation and purification are usually required steps. So far, both the storage and use of hydrogen involve pure hydrogen, which is generally produced via a very expensive separation/purification process. A low cost and high tolerant material is required for hydrogen storage or purification.

In order to evaluate possible effects of impurities on hydrogen sorption of Mg, a preliminary study was carried out using a gas mixture of (80 % H<sub>2</sub> + 20 % CO<sub>2</sub>) to charge a dehydrogenated MgH<sub>2</sub> with and without transition metal carbides at a pressure of 8bar and temperature of 300 °C in IGA coupled with mass-spectrometry (MS). It is interesting to see how the transition metal carbides influence the selectivity and kinetics of the sorption process from the gas mixture.

The samples were prepared by cryomilled and ball-milled. 80 % H<sub>2</sub> + 20 % CO<sub>2</sub> gas mixture is considered as the model product of the steam reforming of natural gas<sup>177</sup>. Before charging the samples with the standard gas mixture, MgH<sub>2</sub> or doped MgH<sub>2</sub> was dehydrogenated fully to Mg. Figure 4-30 shows TG-Mass spectrometry (MS) curves of H<sub>2</sub> + CO<sub>2</sub> absorption of the empty sample holder to compare with the sorption of samples. There was no weight change during the blank test. Whereas it was found that the mass spectrometry curves of three gases, H<sub>2</sub>O, CH<sub>4</sub> and CO were increasing with time, which means there are impurities gases H<sub>2</sub>O, CH<sub>4</sub> and CO existing in the original H<sub>2</sub> + CO<sub>2</sub> gas mixture.

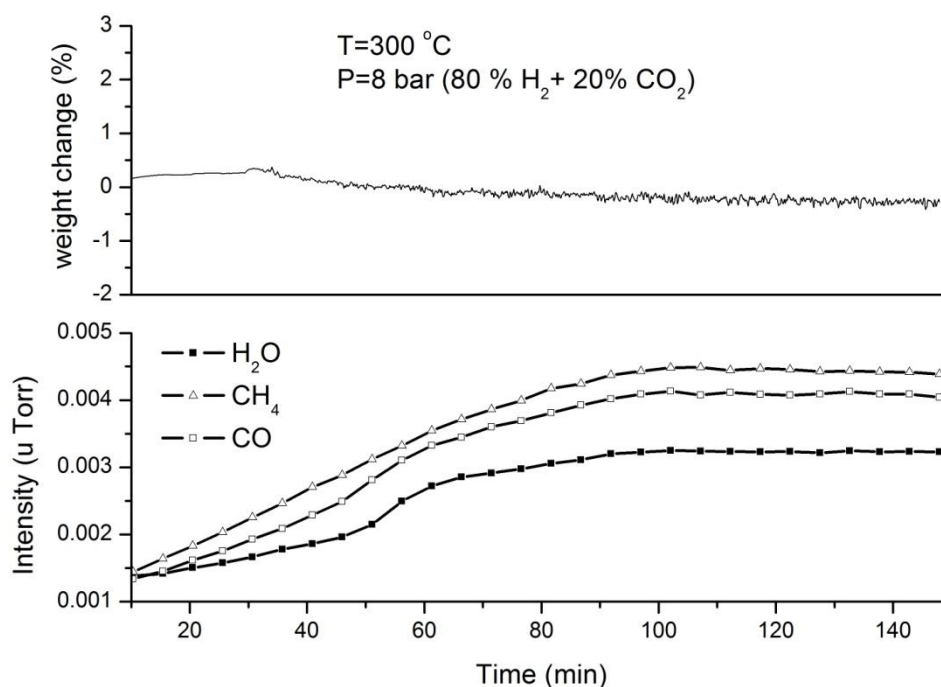


Figure 4-30 TG-MS of the empty sample holder, measured at 300 °C under 8 bar H<sub>2</sub>+CO<sub>2</sub> pressure.

#### 4.5.1 (H<sub>2</sub> + CO<sub>2</sub>) absorption of dehydrogenated cryomilled MgH<sub>2</sub>

The (H<sub>2</sub> + CO<sub>2</sub>) absorption behavior of the dehydrogenated cryomilled MgH<sub>2</sub> from 80% H<sub>2</sub> + 20% CO<sub>2</sub> gas mixture is shown in Figure 4-31. The maximum of absorption was more than 8 wt % in 120 min, which even exceeded the theoretical hydrogen storage capacity of Mg (7.6 wt %). Thus, the reactions between dehydrated cryomilled MgH<sub>2</sub> and 80% H<sub>2</sub> + 20% CO<sub>2</sub> gas mixture at 300 °C were further studied due to its over-absorption. There are three possible reactions proposed as follows.



Higher temperature over 600 °C or catalyst (e.g. Pt) is required for the reaction between H<sub>2</sub> and CO<sub>2</sub> (Equation 4-1). The reaction doesn't contribute to the weight gain of the sample,

and there are no peaks occurred along the CO and H<sub>2</sub>O traces from mass spectrometry analysis. The reaction between H<sub>2</sub> and CO<sub>2</sub> (Equation 4-1) is not possible under the present experimental conditions. The hydrogenation process of Mg (Equation 4-2) should happen at 300 °C under around 6.4 bar H<sub>2</sub> partial pressure. The weight gain is over 7.6 wt %- the theoretical value. Thus the third reaction (Equation 4-3) definitely happened. From Equation 4-3, it has been calculated that the weight gain can be theoretically increased to 71.4 wt %, if the reaction is carried out fully. But the surface of Mg/MgH<sub>2</sub> particles could be covered by MgCO<sub>3</sub> which stopped the inner Mg/MgH<sub>2</sub> interacting with the gases further. The reaction rate decreased greatly after 40 min, as shown in Figure 4-31. The CO, H<sub>2</sub>O and CH<sub>4</sub> traces from the mass spectrometry analysis could be from the original flow gas of (H<sub>2</sub>+ CO<sub>2</sub>). MgO is always existing as an impurity in the Mg/MgH<sub>2</sub> samples and easy to react with CO<sub>2</sub>. The interaction of CO<sub>2</sub> with MgO was studied by several research groups<sup>178-181</sup>. The formation of magnesium carbonate from the reaction between CO<sub>2</sub> and MgO was detected by XPS, UPS, LEED.

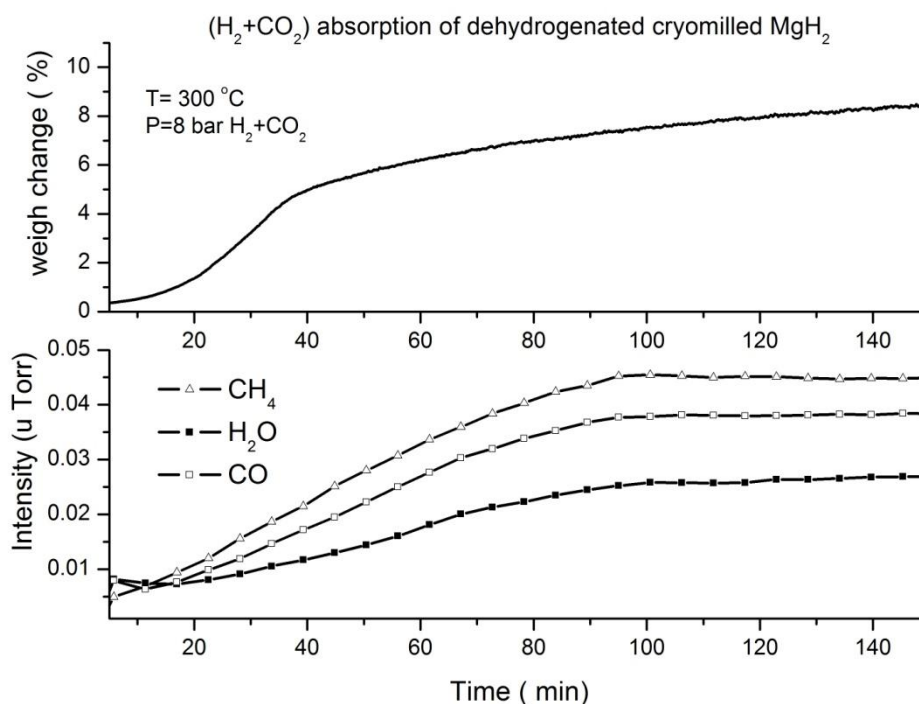


Figure 4-31 TG-MS of the dehydrogenated cryomilled-MgH<sub>2</sub>, measured at 300 °C under 8bar H<sub>2</sub>+CO<sub>2</sub> pressure. After (80 % H<sub>2</sub> + 20 % CO<sub>2</sub>) absorption of dehydrogenated cryomilled-MgH<sub>2</sub>, the sample was decomposed with the temperature range from room temperature to 500 °C at 1 bar helium pressure. The TG-MS curves are shown in Figure 4-32. The starting desorption temperature is about 360 °C, which is the same as that of cryomilled-MgH<sub>2</sub>. The 1.5 % weight loss of dehydrogenated cryomilled-MgH<sub>2</sub> after (H<sub>2</sub>+CO<sub>2</sub>) absorption is corresponding to the dehydrogenation of MgH<sub>2</sub>. MgO and MgCO<sub>3</sub> are stable from room temperature up to 500 °C in helium gas, which didn't have any weight loss. The ~ 6.5 % weight difference between absorption and desorption processes is due to the formation of MgO and MgCO<sub>3</sub>. The reason that no peak of water appeared in MS curves is that H<sub>2</sub>O further reacted with magnesium to form Magnesium hydroxide and hydrogen. The reason that there is no peak of H<sub>2</sub> in the MS analysis (Figure 4-32) is possibly due to the small quantity of hydrogen generated during the desorption, which is out of the detection range of MS.

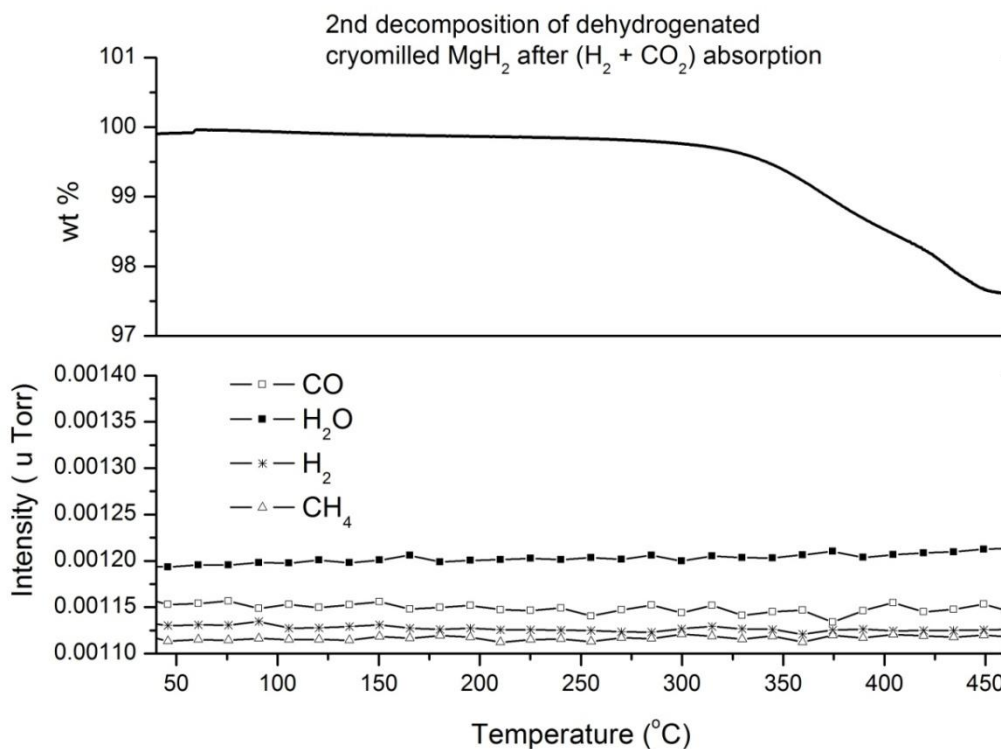


Figure 4-32 TG-MS of 2<sup>nd</sup> decomposition of dehydrogenated cryomilled  $\text{MgH}_2$  after  $\text{H}_2+\text{CO}_2$  absorption, measured at 1 bar helium pressure.

From XRD patterns of the samples, Figure 4-33a, the peaks of Mg, MgO,  $\text{MgH}_2$ , and  $\text{MgCO}_3$  was detected after  $(\text{H}_2+\text{CO}_2)$  absorption of dehydrogenated cryomilled- $\text{MgH}_2$ . The obvious peaks of Mg are due to the incomplete reaction, which can be concluded from the weight gain, 8 wt%, which is much less than the theoretical value of 71.4 wt%. After the second decomposition, the peaks of  $\text{MgH}_2$  were not detected and the main phases were Mg and  $\text{MgCO}_3$  (Figure 4-33b). This also demonstrated that  $\text{MgH}_2$  was dehydrogenated to Mg during heating. In conclusion, the possible reaction steps of the dehydrogenated cryomilled- $\text{MgH}_2$  with the (80%  $\text{H}_2$  + 20 %  $\text{CO}_2$ ) gas mixture at 300  $^\circ\text{C}$  are listed as follows. The calculated enthalpy changes show equation 4-2 and 4-4 are endothermic reactions or heat-absorbing processes, which mean the reactions need to absorb energy from the surroundings in the form of heat.

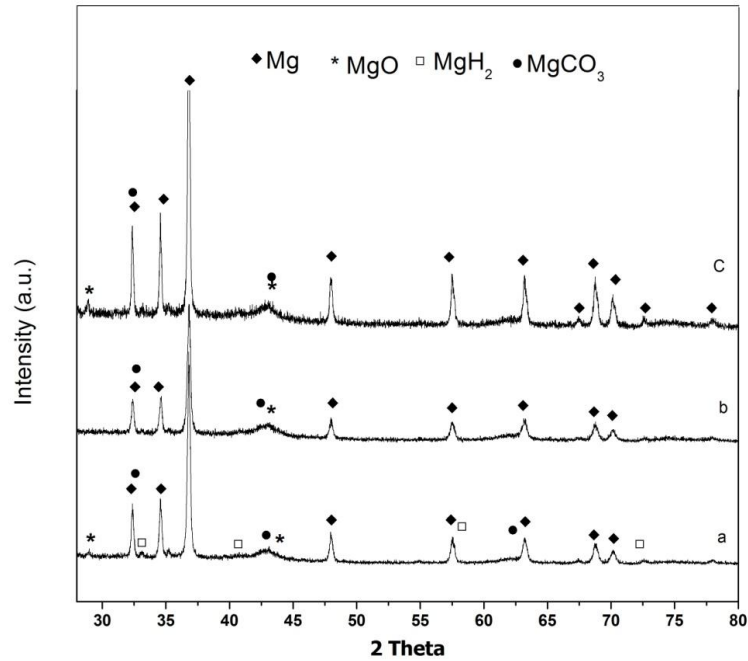
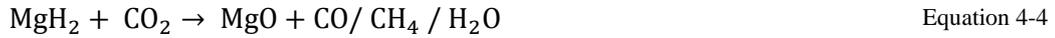


Figure 4-33 XRD patterns of the samples: a, ( $\text{H}_2 + \text{CO}_2$ ) absorption of dehydrogenated cryomilled- $\text{MgH}_2$ ; b, 2<sup>nd</sup> dehydrogenation of dehydrogenated cryomilled- $\text{MgH}_2$  after ( $\text{H}_2 + \text{CO}_2$ ) absorption; and c,  $\text{CO}_2$  absorption of dehydrogenated cryomilled- $\text{MgH}_2$

#### 4.5.2 ( $\text{H}_2 + \text{CO}_2$ ) absorption of dehydrogenated milled-( $\text{MgH}_2 + \text{TiC} / \text{Mo}_2\text{C}$ )

From Figure 4-34, the weight of dehydrogenated as-received  $\text{MgH}_2$  didn't increase after ( $\text{H}_2 + \text{CO}_2$ ) absorption at 300 °C and 8 bar gas pressure. The weight gain of dehydrogenated 60 h ball-milled ( $\text{MgH}_2 + \text{Mo}_2\text{C}$ ) after cryomilling was less than  $1.5 \pm 0.02$  wt%, whereas that of milled ( $\text{MgH}_2 + \text{TiC}$ ) was  $5.5 \pm 0.02$  wt% in 230 min, which were less than weight gain of dehydrogenated cryomilled  $\text{MgH}_2$ . Thus it indicates that cryomilled  $\text{MgH}_2$  after dehydrogenation has strong ability to absorb or react with 80 %  $\text{H}_2 + 20\%$   $\text{CO}_2$  gas mixture. TiC inserted in the inner space of grain boundaries of  $\text{MgH}_2$  particles, which enhanced  $\text{H}_2$

absorption rate of Mg and induced fast formation of  $\text{MgCO}_3$ , therefore stopped the interaction between  $\text{Mg}/\text{MgH}_2$  and  $\text{H}_2/\text{CO}_2$  molecules and decreased reaction rate.

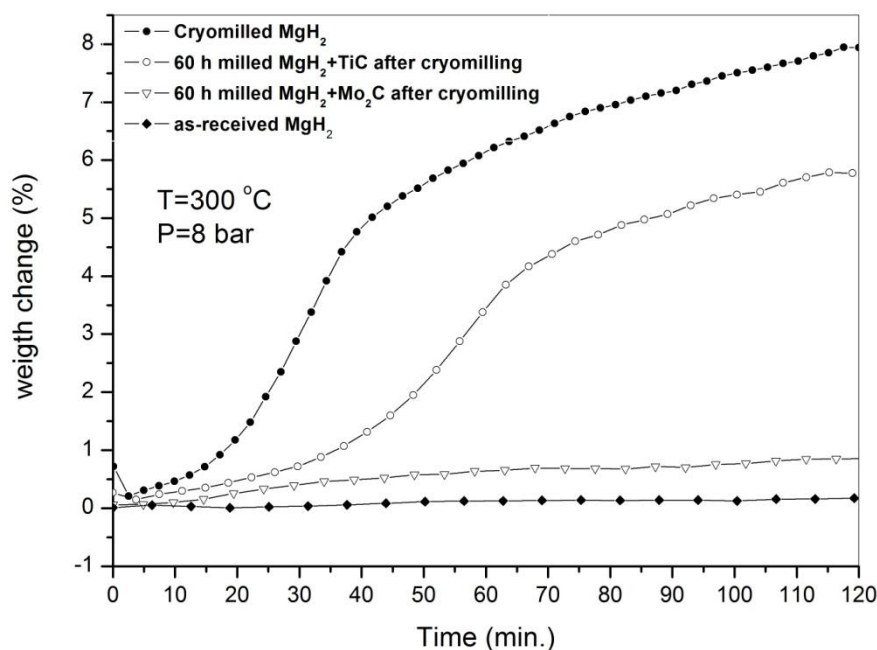


Figure 4-34 ( $\text{H}_2+\text{CO}_2$ ) absorption of dehydrogenated  $\text{MgH}_2$  with and without catalyst, measured at 300 °C under 8 bar ( $\text{H}_2 + \text{CO}_2$ ) pressure.

### 4.5.3 Interaction between $\text{Mg}/\text{MgH}_2$ and $\text{CO}_2$ gas

To confirm the reaction between  $\text{MgH}_2$  and  $\text{CO}_2$ , both the dehydrogenated cryomilled- $\text{MgH}_2$  and the cryomilled-  $\text{MgH}_2$  were subjected to a pure  $\text{CO}_2$  atmosphere at 300 °C and 8 bar  $\text{CO}_2$  pressure, shown in Figure 4-35 and Figure 4-36. The sample weight of the dehydrogenated cryomilled- $\text{MgH}_2$  almost increased  $0.8 \pm 0.02$  wt%. From XRD analysis, Figure 4-33c,  $\text{MgCO}_3$  and  $\text{MgO}$  are the new compounds formed during  $\text{CO}_2$  absorption of dehydrogenated cryomilled  $\text{MgH}_2$  adsorbed at 8 bar  $\text{CO}_2$  atmosphere. The reaction of  $\text{CO}_2$  with  $\text{Mg}$  was studied by XRS and EELS<sup>182, 183</sup>. A mechanism for the carbonate formation observed above 100 K was put forward. It is suggested that dissociative absorption of oxygen takes place,

followed by the chemisorptions of  $\text{CO}_2$  at oxygen sites. The reaction can be presented as follows:



This is an endothermic reaction with  $\Delta H_{298} = 272.8 \text{ kJ/mol}$ . Also, the  $\text{MgO}$  easily reacts with  $\text{CO}_2$  under the experimental conditions to form  $\text{MgCO}_3$ , Equation 4-5, which has been detected by XRD.

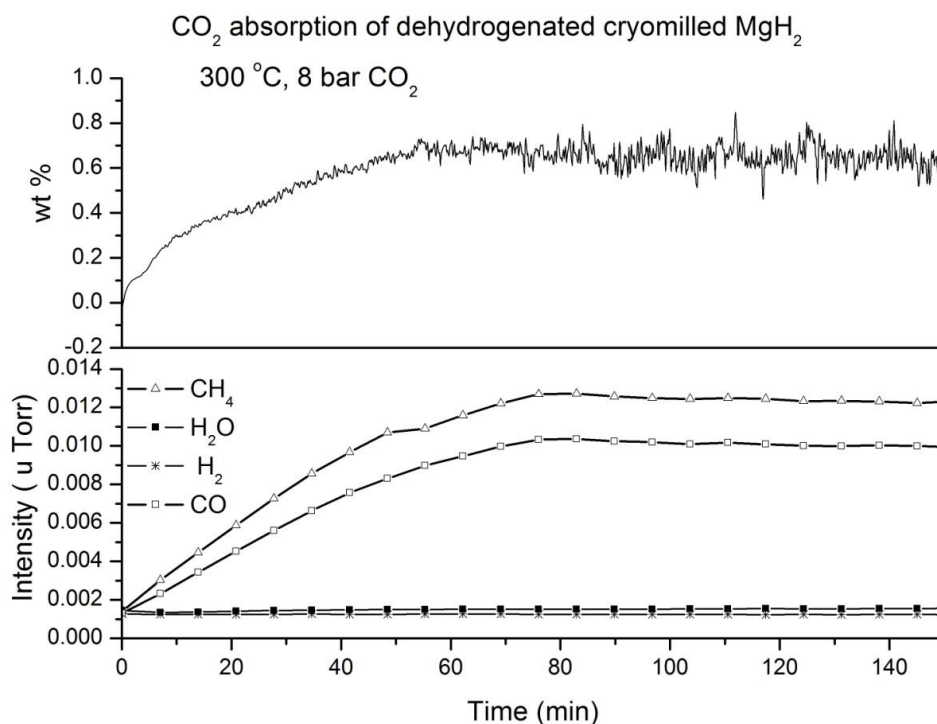


Figure 4-35 TG-MS of  $\text{CO}_2$  absorption of dehydrogenated cryomilled- $\text{MgH}_2$ , measured at  $300 \text{ }^\circ\text{C}$  under 8 bar  $\text{CO}_2$  pressure.

From Figure 4-36, the weight of cryomilled- $\text{MgH}_2$  increased to 5 wt% during the  $\text{CO}_2$  absorption process, which is much higher than that of dehydrogenated cryomilled- $\text{MgH}_2$  (0.8 wt %). Thus  $\text{MgH}_2$  can absorb  $\text{CO}_2$  more easily than  $\text{Mg}$ . From the above, it can be confirmed that the main reaction steps of dehydrogenated cryomilled- $\text{MgH}_2$  with  $(\text{H}_2 + \text{CO}_2)$

gas mixture are hydrogenation of Mg to form  $\text{MgH}_2$ , and then the reaction between  $\text{MgH}_2$  and  $\text{CO}_2$  to form  $\text{MgO}$  and gas mixtures. In the main reaction steps, the side reactions happened, such as Equation 4-5 and the reaction between  $\text{MgO}$  and  $\text{H}_2\text{O}$ .

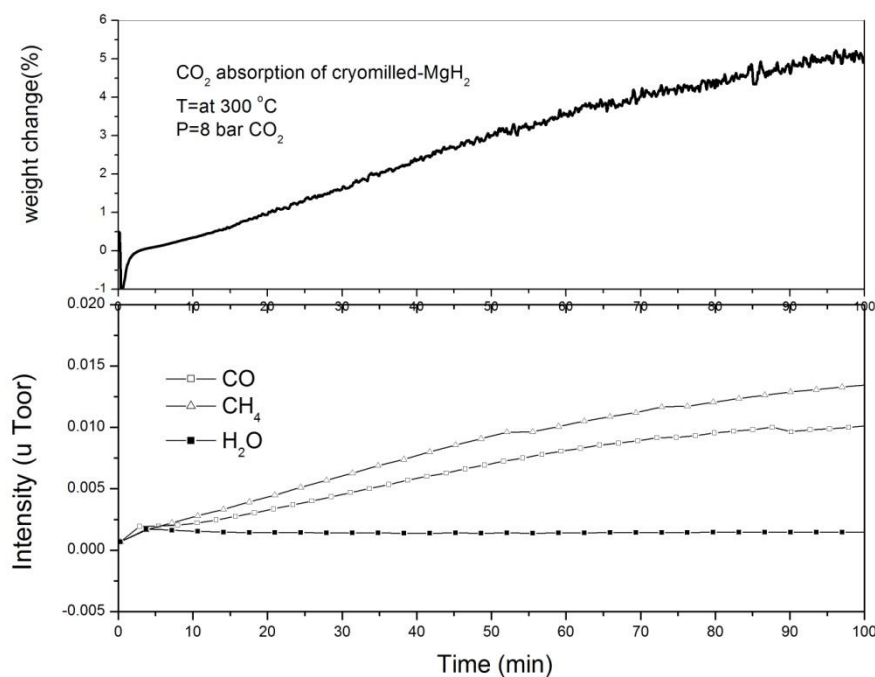


Figure 4-36 TG-MS of  $\text{CO}_2$  absorption of cryomilled- $\text{MgH}_2$ , measured at 300 °C under 8 bar  $\text{CO}_2$  pressure.

#### 4.5.4 Summary

The reactions of Mg (from dehydrogenated  $\text{MgH}_2$ ) with (80%  $\text{H}_2$  + 20%  $\text{CO}_2$ ) gas mixture at 300 °C have been proved to occur and is rather complex. Magnesium preferentially reacts with  $\text{H}_2$  due to the high content of  $\text{H}_2$  in mixture gas. Then  $\text{MgH}_2$  reacts with  $\text{CO}_2$  to form gas mixtures, such as  $\text{CO}$  and  $\text{H}_2\text{O}$  etc. and  $\text{MgO}$ , which makes further reaction with  $\text{CO}_2$  to form  $\text{MgCO}_3$ . Reaction mechanisms need to be studied further in the future work.

## CHAPTER 5 GENERAL DISCUSSION

### 5.1 The Effect of Milling Conditions on Microstructure and Hydrogen Sorption Properties of Magnesium Hydride.

Magnesium hydride ( $\text{MgH}_2$ ) shows great potential as a material for reversible hydrogen storage because it is abundant, inexpensive, environmentally benign, easy to handle and possesses a sufficient hydrogen storage capacity (7.6 wt %). It is well known that a breakthrough in the magnesium hydride technology has been achieved by using the high-energy mechanical (ball) milling technique to prepare nanocrystalline hydride powders<sup>77, 159</sup>. Milling of  $\text{MgH}_2$  instead of pure Mg produces nanocrystalline powders with larger surface areas beneficial to the hydrogen sorption process<sup>30</sup>. Nanocrystalline magnesium hydride exhibits fast absorption and desorption kinetics at 300 °C when compared with its non-milled counterpart<sup>95</sup>. This behavior has been attributed to the faster diffusion of hydrogen along grain boundaries and the higher number of heterogeneous nucleation sites for hydrogen during absorption or the pure magnesium phases during desorption. Unfortunately, the slow hydrogenation/dehydrogenation kinetics and the high desorption temperatures remain problematic. To overcome these problems further research is needed.

In my work, there are two types of millings, cryogenic milling and high energy ball milling, which are used for the engineering of  $\text{MgH}_2$  in its nanocrystalline form in combination with different additives. The microstructural and hydriding/dehydriding properties of nanocrystalline  $\text{MgH}_2$  prepared by cryogenic milling and ball milling have been investigated in the present work.

The estimates for the nanograin size of the as-received  $\text{MgH}_2$ , calculated based on XRD patterns<sup>184</sup>, is of the order of  $65 \pm 5$  nm. After 8 h cryogenic milling, the grain size of  $\text{MgH}_2$  has decreased greatly to  $25 \pm 3$  nm. It has been suggested that the presence of liquid nitrogen during cryomilling has several advantages. For example, decreased oxygen

contamination<sup>185</sup> and enhanced deformation during milling<sup>162</sup>. In particular cryogenic milling offers an effective solution for achieving fine powders by enhancing the brittleness of the materials and reducing their tensile strength for materials<sup>22</sup>. With a further 60 h ball milling, the grain size of MgH<sub>2</sub> is only reduced slightly to 20 ± 3 nm. Therefore, the cryogenic milling process is very effective in reducing crystalline size of MgH<sub>2</sub> and further high energy ball milling only reduces the grain size by a nominal extent. Cryogenic milling provides significant process improvements in terms of the surface residual stresses and the effectiveness of grinding forces mainly due to substantial temperature reductions in the grinding zone, and a decrease in the magnitude of tensile residual stresses for all the materials<sup>186</sup>. Despite this, peaks of the  $\gamma$ -MgH<sub>2</sub>, which is known as a high-pressure orthorhombic phase, are observed in the ball-milled samples.

The 8 h cryogenically milled MgH<sub>2</sub> presents more granular surfaces as compared to the further 60 h ball-milled MgH<sub>2</sub>. The cryomilled MgH<sub>2</sub> has irregular shapes resembling the popcorn structure and agglomerate together, which is typical for small particles, as seen in Figure 4-2. The nanoparticle size distributions show the long time ball-milled powders appear more heterogeneous, containing a large number of larger and smaller particles, presumably formed by the clustering and cold-welding of small particles (Figure 4-2, Figure 4-9 and Figure 4-18). The particle size distribution after 60 h ball-milling becomes broader compared with that of only 8 h cryomilling. This is explained by the continuous welding and fracture of particles caused by the collision with milling media balls<sup>187</sup>. These results are in good agreement with the results reported by Varin et al.<sup>188</sup> and Reule et al.<sup>189</sup>, who also observed a propensity for the clustering and cold-welding of commercial MgH<sub>2</sub> into larger particles during milling for durations longer than 10 h.

The desorption and absorption curves of MgH<sub>2</sub> after cryogenic milling and ball milling were compared to the as-received MgH<sub>2</sub> powder. The 8 h cryogenic milling leads to a visible

enhancement of both desorption and absorption kinetics. The pronounced differences are observed in the desorption kinetics profile (Figure 4-3 and Figure 4-4). There is a significant release of hydrogen under the pressure of 1 bar by all the cryomilled  $\text{MgH}_2$  samples at 320 °C and ball-milled  $\text{MgH}_2$  samples at 305 °C, while the desorption of as-received  $\text{MgH}_2$  starts at 418 °C, Table 5-1. The absorption kinetics of as-received  $\text{MgH}_2$  is much lower than the cryomilled and ball-milled samples. Previous reports have confirmed that the milling process is specially suited to the fabrication of nanocrystalline hydrides exhibiting very fast hydrogen sorption properties. It could be concluded that the most likely explanation for these findings is that milling has the effect of reducing the particle and crystallite size, increasing the specific surface area of the material. This hypothesis would match the results as there were no pronounced differences in the hydrogen desorption and absorption kinetics between the 8 h cryomilled  $\text{MgH}_2$  and further 60 h ball-milled  $\text{MgH}_2$  after cryomilling. Both the materials had very similar particle and grain sizes compared with those of the as-received  $\text{MgH}_2$ .

Reducing the particle size and grain size of  $\text{MgH}_2$  increases the kinetics of absorption while maintaining the hydrogen storage capacity. Cryogenic milling is effective in reducing the grain sizes and particle sizes. Unfortunately the decomposition of  $\text{MgH}_2$ , even in its nanocrystalline form, is not possible below 300 °C. This internal (material) drawback of  $\text{Mg}/\text{MgH}_2$  can be partially overcome by the addition of catalysts to further enhance the absorption and desorption kinetics of hydrogen.

Table 5-1 Hydrogen sorption parameters of all samples.

Sample	Grain Size of $\beta$ -MgH <sub>2</sub> (nm)	Mean particle size ( $\mu$ m)	T <sub>Onset</sub> (°C)	T <sub>Peak</sub> (°C)	E' (KJ/mol)*	Absorption Rate (wt. %/min)
As-received MgH <sub>2</sub>	65 ± 5	30 ± 2	418	434	235 ± 10	0.008 ± 0.00004
8 h cryomilled MgH <sub>2</sub>	25 ± 3	0.19 ± 0.02	320	362	200 ± 9	0.06 ± 0.0001
60 h ball-milled MgH <sub>2</sub> after cryomilling	20 ± 3	0.28 ± 0.02	305	360	199 ± 9	0.1 ± 0.0001
8 h cryomilled (MgH <sub>2</sub> + 2%TiC)	27 ± 3	0.2 ± 0.02	280	332	157 ± 9	0.08 ± 0.0001
60 h ball-milled (MgH <sub>2</sub> + 2%TiC) after cryomilling	23 ± 3	0.29 ± 0.02	190	275	104 ± 6	0.12 ± 0.0001
60 h ball-milled (MgH <sub>2</sub> + 8%TiC) after cryomilling	20 ± 3	0.3 ± 0.02	175	264	89 ± 5	–
8 h cryomilled (MgH <sub>2</sub> +Mo <sub>2</sub> C)	27 ± 3	0.44 ± 0.02	320	360	217 ± 10	0.074 ± 0.0001 (40- 60 min) 0.021 ± 0.0001 (60-180 min)
60 h ball-milled (MgH <sub>2</sub> +Mo <sub>2</sub> C) after cryomilling	18 ± 3	0.53 ± 0.02	300	358	167 ± 9	0.074 ± 0.0001 (40- 60 min) 0.023 ± 0.0001 (60-180 min)
(MgH <sub>2</sub> +2%Ni)	--	--	190	301	--	--
(MgH <sub>2</sub> +2%Mo <sub>2</sub> C+2%Ni)	--	0.54 ± 0.02	240	328	--	--
(MgH <sub>2</sub> +2%TiC+2%Ni)	--	0.42 ± 0.02	195	282	--	--

## 5.2 The Catalytic Mechanism of TiC on Hydrogen Sorption Properties of Magnesium Hydride

The phenomenon of mechanical milling helps to pulverize the particles of  $\text{MgH}_2$  into nanocrystalline phases and thus leads to lowering the activation energy of desorption<sup>159</sup>. The height of the activation energy barrier depends on the surface elements<sup>12</sup>. It can be concluded that the activation barrier has been drastically lowered by nanocatalyst doping, suggesting that the collision frequency between the  $\text{H}_2$  molecules and transition metal nanoparticles increases with decreasing particle sizes for  $\text{MgH}_2$  and the catalysts, shown in Table 4-1, Table 4-2 and Table 4-3. From the experimental results, two facts with regard to the thermal stability and the sorption kinetics can be extracted: (i) TiC nanoparticles reduce the temperature for hydrogen release from  $\text{MgH}_2$ , while  $\text{Mo}_2\text{C}$  does not. (ii) TiC enhances the hydrogen absorption kinetics of  $\text{Mg}/\text{MgH}_2$ ;  $\text{Mo}_2\text{C}$  shows almost no influence on that of  $\text{Mg}/\text{MgH}_2$ . These results indicate clearly that the catalytic behaviors are distinct from each other, depending not only on the hydrides, but also on the transition metal carbides present. A correlation among them is discussed below.

### 5.2.1 Analysis of hydrogen sorption of $\text{MgH}_2$ catalyzed by TiC

Recently, it has been reported that metallic Ti could catalytically improve the hydrogen storage property of Mg-based hydrides. There are two different mechanisms reported for the enhancement of the reaction kinetics of  $\text{MgH}_2$  with dopants. One believes the interactions between the hydrides and the Ti-containing agents weakens the Mg-H bonds and favors the recombination of hydrogen atoms toward the hydrogen molecules<sup>22, 190</sup>. Examples include the classic Ti-halides (e.g.  $\text{TiCl}_3$ ) reacting with  $\text{MgH}_2$  to form  $\text{TiH}_x$ , which acts as the catalyst responsible for hydrogen dissociation/recombination at the surface of hydride after ball milling and hydriding/dehydriding processes. The other opinion is that Ti or metallic Ti acts as a classic catalyst for hydrogen dissociation/recombination on the surface of reacting

solids<sup>191, 192</sup>. From XRD analysis, TiC didn't react with MgH<sub>2</sub> during the milling and dehydrogenation/hydrogenation processes. This means that TiC and MgH<sub>2</sub> maintain their original phase structures in different hydriding/dehydriding stages throughout, as shown from the XRD patterns in Figure 4-1, and Figure 4-7. These results prove that TiC had not reacted with MgH<sub>2</sub> in this study, and no TiH<sub>x</sub> or other alloy was formed during the ball milling and hydriding/dehydriding processes. Combining the results of the above-mentioned hydrogen sorption properties of MgH<sub>2</sub> catalyzed by TiC composite and the results of our previous investigation, we believe that TiC nanoparticles are existing stably and separately around the MgH<sub>2</sub> matrix as the catalytically active species for the reversible hydrogen storage of the composite. Because TiC powder is thermodynamically more stable than other Ti-chloride catalysts<sup>193, 194</sup>, utilization of this stable TiC catalyst can be identified as an effective way to catalytically enhance the hydrogen sorption properties of MgH<sub>2</sub> without generating any dead weight byproducts. This makes TiC's catalytic mechanism similar to that of TiN<sup>195</sup> and TiO<sub>2</sub><sup>196</sup>.

The dehydrogenation of magnesium hydride consists of the following steps: decomposition of the hydride phase to form the magnesium phase, diffusion of hydrogen atoms, and combination of hydrogen atoms into molecules around the TiC active sites and desorption of hydrogen molecules<sup>191, 197</sup>, as Figure 5-1. Similarly, the catalytic hydrogenation process in this system follows the reverse order of the above dehydrogenation reaction steps.

It is believed that the greatly reduced particle size in the ball-milled composite would increase the hydrogenation/dehydrogenation reaction activity sites and hence it would be beneficial to the enhancement of hydrogen storage kinetics as shown in Table 5-1. It also can be found that the mean particle size of 60 h ball-milled (MgH<sub>2</sub>+TiC) is larger than that of the 60 h ball-milled MgH<sub>2</sub> without TiC. This is because the TiC content of the (MgH<sub>2</sub>+TiC) composite is hard and brittle, and take longer to pulverize into fine particles.

The SEM and TEM images of the (MgH<sub>2</sub>+TiC) composite, Figure 4-9 and **Error! Reference source not found.**, show that some of TiC nanoparticles have been inserted into the MgH<sub>2</sub> grain boundaries. The onset and peak temperature of hydrogen desorption of the 60 h ball-milled (MgH<sub>2</sub>+TiC) is much lower than the 60 h ball-milled MgH<sub>2</sub> without TiC. This is due to the shorter hydrogen diffusion distance within the (MgH<sub>2</sub>+TiC) composite, making the diffusion of hydrogen atoms easier and quicker across MgH<sub>2</sub>. Likewise the activation energy of desorption for the (MgH<sub>2</sub>+TiC) decreased greatly. Throughout the 8 h cryogenic milling and a further 60 h ball milling MgH<sub>2</sub> mixed with the catalyst TiC to produce a favorable reactive composite with sufficient area for contacting hydrogen and a large amount of defects acting as reaction active sites. TiC active sites have a greater affinity for hydrogen than MgH<sub>2</sub>, which reduces the bond strength between Mg-H. In addition, Xiao et al. believe<sup>192</sup> that the smaller TiC particles inlaid on the surface of the larger matrix act not only as the catalytic active sites for the redox reaction of hydrogen but also as a source for hydrogen spillover, assisting hydrogen diffusion into the matrix. The spillover properties of noble metal catalyst have been proved by Xu et al<sup>197</sup>.

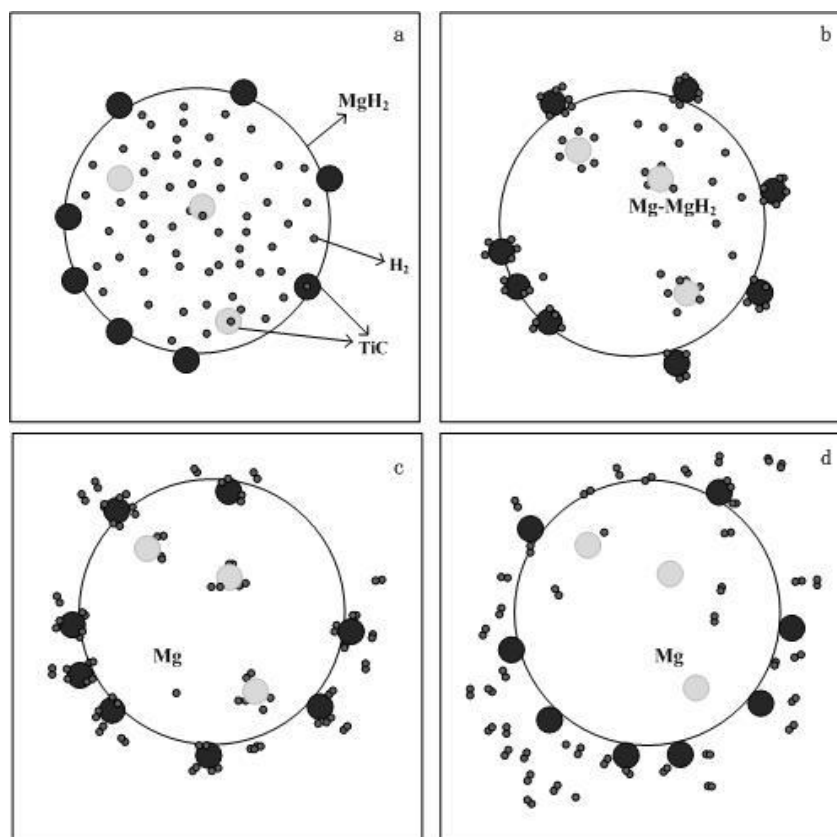


Figure 5-1 Scheme of the ( $\text{MgH}_2+\text{TiC}$ ) mixture in different states of dehydrogenation. (a) Milled  $\text{MgH}_2$  with TiC nanoparticles, (b) Decomposition of hydride phase to form magnesium phase, (c) Combination with hydrogen atoms into molecules, and (d) desorption of hydrogen molecules

From Figure 4-10 and Table 5-1, it is apparent there are no big differences between the sizes of the cryomilled and ball-milled nanoparticles of ( $\text{MgH}_2+\text{TiC}$ ). However, the hydrogen sorption properties and kinetics of 60 h milled ( $\text{MgH}_2+\text{TiC}$ ) are faster than 8 h cryomilled ( $\text{MgH}_2+\text{TiC}$ ). This is because the high energy ball milling for 60 h forces TiC nanoparticles into the inner space or grain boundaries of Mg/ $\text{MgH}_2$ . Consequently the catalytic effect on transformation and growth of the inner phase is improved.

In addition, compared with the as-received  $\text{MgH}_2$  sample, the onset and peak temperatures of hydrogen desorption decreased significantly from 418 °C to 190 °C and from 434 °C to 275 °C with 2 % TiC. The ( $\text{MgH}_2+8\%$  TiC) showed a slightly greater effect on hydrogen sorption than ( $\text{MgH}_2 + 2\%$  TiC), with an onset temperature of 175 °C and a peak

temperature of 264 °C. Whilst doping can lower the hydrogen desorption temperature, heavy doping can lower the hydrogen storage capacity, slow kinetics and increase the rate of hysteresis. Thus we can conclude that a low amount of TiC as a catalyst can improve the hydrogen sorption kinetics of MgH<sub>2</sub>, but a large amount of TiC could block the hydrogen diffusion and lower the hydrogen capacity. Ranjbar et al.<sup>15</sup> reported 2 wt % SiC doped MgH<sub>2</sub> shows the optimum desorption kinetics and too much SiC addition degraded the hydrogen absorption/desorption kinetics. Xie et al.<sup>139</sup> reported that the desorption kinetics enhance with increasing Ni nanoparticles when the quantity of catalyst is below 25 wt%. When the quantity of Ni nanoparticles exceeds 25 wt%, the improvement to the desorption kinetics is minor.

### 5.2.2 Structure of TiC to improve catalytic effect

TiC is a typical faceted crystal. Figure 5-2(a) shows its crystal structure. C atoms occupy the octahedral positions. If viewed along the axis perpendicular to the (111) planes, Ti and C atoms form a hexagonal shape as shown in Figure 5-2 (b). It has been reported that TiC has a simple-hexagonal structure<sup>198</sup>. Chien et al.<sup>199</sup> reported that stress induced the transformation of TiC from cubic to hexagonal structures. As reported by Chien<sup>200</sup>, sub-boundary defect structures in single crystal TiC were observed. Because high-energy ball milling is known to introduce a high number of crystal lattice defects into a material, we have investigated in chapter 4.2 that some TiC nanoparticles are inserted into the grain boundaries of MgH<sub>2</sub> nanoparticles. The microstructure of MgH<sub>2</sub> was changed by not only high-energy ball milling but also the addition of TiC. The increasing structural defects effectively expedite hydrogen diffusion, which is the control step in the hydrogen sorption processes<sup>20, 192, 197</sup>.

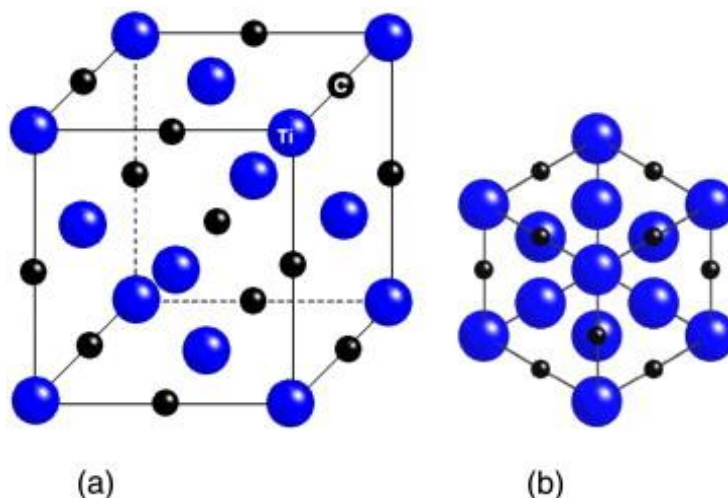


Figure 5-2 (a) Crystal structure of TiC, and (b) projection of Ti–C atoms along [111] direction. The smaller atoms are C atoms.<sup>151</sup>

Titanium alloys have a high affinity for hydrogen<sup>108</sup>. The research from Barkhordarian<sup>20</sup> indicates that strong transition-metal-hydrogen reaction energies will improve the catalytic activity on hydrogen sorption reactions. In our reaction system, the interaction between Ti ions and hydrogen atoms is due to the high affinity of Ti for the hydrogen. This attraction improves the hydrogen sorption kinetics of our materials.

### 5.2.3 Thermodynamic stability of TiC for catalysis

Barkhordarian et al.<sup>20</sup> proposed a transition metal compound, such as  $\text{Nb}_2\text{O}_5$ ,  $\text{V}_2\text{O}_5$  and  $\text{TiO}_2$ , as an effective catalyst and stated that the compound should have a low thermodynamic stability to allow a chemical interaction with the magnesium support. The enthalpies of formation for  $\text{TiCl}_3$  and  $\text{TiCl}_4$  are  $-240$  and  $-201$  kJ per Cl atom respectively, this makes  $\text{TiCl}_3$  more stable than  $\text{TiCl}_4$ . Therefore, Mg atoms will require less energy to change the electronic structure of the Ti in  $\text{TiCl}_4$  rather than  $\text{TiCl}_3$ <sup>20</sup>. However, if the stability is too low, like  $\text{Re}_2\text{O}_7$  ( $-180$  kJ/ mol), the compound reacts completely with magnesium and its catalytic activity is diminished. TiC is a stable compound with formation enthalpies of  $-190.4 \pm 17.0$

$\text{kJ/mol}^{201}$ , which is a optimum stability of the transition metal compounds that have higher catalytic activity, comparing  $\text{TiCl}_3$  and  $\text{Re}_2\text{O}_7$ .

#### 5.2.4 Summary

On the basis of the above discussion, the following mechanisms are proposed for the TiC catalyst influences upon the hydrogen sorption of  $\text{MgH}_2$ . During absorption, hydrogen molecules disassociate on the Ti ions of TiC resulting in the formation of a Ti-H bond. The Ti ions dissociate hydrogen molecules and pass hydrogen atoms to the surrounding magnesium atoms leading to the formation of  $\text{MgH}_2$ . In the case of desorption, Mg-H bonds are thermodynamically unstable, leading to dissociation from  $\text{MgH}_2$ . The Ti ions of TiC then form a bond with hydrogen atoms, they act as an intermediate state which allows easier recombination for hydrogen atoms toward the molecular state.

### 5.3 Effect of $\text{Mo}_2\text{C}$ and Ni on Hydrogen Sorption Properties of $\text{MgH}_2$

Comparing the particle size of ( $\text{MgH}_2 + 2\% \text{TiC}$ ), the particle size of both 8 h cryomilled ( $\text{MgH}_2 + \text{Mo}_2\text{C}$ ) and 60 h ball-milled ( $\text{MgH}_2 + \text{Mo}_2\text{C}$ ) after cryomilling is bigger,  $0.44 \pm 0.02 \mu\text{m}$  and  $0.53 \pm 0.02 \mu\text{m}$  respectively (Table 5-1). Most of the  $\text{Mo}_2\text{C}$  nanoparticles are dispersed on the surface on  $\text{MgH}_2$  in the milling process, seen in Figure 4-18. The catalytic effect on the inner phase transformation and growth is limited. L. Xie et al.<sup>139</sup> have suggested that one principle of choosing a catalyst is according to the catalysts ability for enhancing the combination of H atoms. It has been suggested that during the dissociation of a H molecule, the  $\sigma$  electron of hydrogen first donates to a vacant metal d orbital. Then the bond is stabilized by back-donation of electrons from the filled d orbital to the anti-bonding orbital  $\sigma^*$  of the  $\text{H}_2$ . Increasing the back-donation to  $\sigma^*$  facilitates to break the H-H bond to form H atoms. The combination of H atoms depends on the electron distribution and orbital structure of the transition metals<sup>202</sup>. The atomic number of Mo in periodic table is 42, bigger

than Ti (22) and Ni (28). The valence electrons of Ti and Ni are on 3d and 4s orbital (Table 5-2), which have a stronger nuclear attraction to H atoms than Mo. It can explain the catalytic effect of TiC and Ni on hydrogen sorption of Mg/MgH<sub>2</sub> than that of Mo<sub>2</sub>C.

It has been reported that Ni nanoparticles enhance the combination of hydrogen atoms to improve the desorption kinetics of MgH<sub>2</sub><sup>139</sup>. In the study, Ni, as an additive mixing, with 60 h ball-milled (MgH<sub>2</sub>+ Mo<sub>2</sub>C) for 15 min reduces the hydrogen desorption temperature of MgH<sub>2</sub>. However, the 60 h ball-milled (MgH<sub>2</sub>+TiC) without Ni has better performance on hydrogen desorption than (MgH<sub>2</sub>+TiC+Ni), shown in Table 5-1. It further confirms that TiC has a very effective catalyst on hydrogen sorption of MgH<sub>2</sub>.

Table 5-2 Atomic Structure of Ti, Ni and Mo<sup>203</sup>

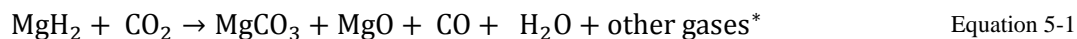
Element	atomic number	electron configuration	Valence Electrons
Ti	22	1s <sup>2</sup> 2s <sup>2</sup> p <sup>6</sup> 3s <sup>2</sup> p <sup>6</sup> d <sup>2</sup> 4s <sup>2</sup>	3d <sup>2</sup> 4s <sup>2</sup>
Ni	28	1s <sup>2</sup> 2s <sup>2</sup> p <sup>6</sup> 3s <sup>2</sup> p <sup>6</sup> d <sup>8</sup> 4s <sup>2</sup>	3d <sup>8</sup> 4s <sup>2</sup>
Mo	42	1s <sup>2</sup> 2s <sup>2</sup> p <sup>6</sup> 3s <sup>2</sup> p <sup>6</sup> d <sup>10</sup> 4s <sup>2</sup> p <sup>6</sup> d <sup>5</sup> 5s <sup>1</sup>	4d <sup>5</sup> 5s <sup>1</sup>

#### 5.4 Interaction of Mg/MgH<sub>2</sub> with (H<sub>2</sub>+CO<sub>2</sub>) Gas Mixture

Studies of the reactions of Mg/MgH<sub>2</sub> in a gas mixture of (H<sub>2</sub>+CO<sub>2</sub>) are rather scarce. Interaction between (80 % H<sub>2</sub>+ 20 % CO<sub>2</sub>) and Mg/MgH<sub>2</sub> at 8 bar pressure and 300 °C is reported in this work. From the results in Section 4.5, (80 % H<sub>2</sub>+ 20 % CO<sub>2</sub>) reacts with Mg can be equal to the reaction of CO<sub>2</sub> with MgH<sub>2</sub>, because the first step of sequenced reactions is hydrogenation of Mg.

It is well known that dissociative absorption of CO<sub>2</sub> occurs on a number of metals<sup>181, 204</sup>. In these cases, the presence of hydrogen anions at the surface promotes the deoxidization of CO<sub>2</sub> to form carbon monoxide and methane. It is suggested here that the reduction of CO<sub>2</sub> on MgH<sub>2</sub> occurs in three steps: initially, the CO<sub>2</sub> dissociates on the surface and (Mg-O) bonds are formed. The second step is the formation of methane based on the reaction of atomic

hydrogen with C ions. Finally, the interaction of CO<sub>2</sub> with MgO produces MgCO<sub>3</sub>. The content of MgH<sub>2</sub>, MgO and MgCO<sub>3</sub> formed during the reaction varies with different ratio of H<sub>2</sub>: CO<sub>2</sub> in the flow gas stream and the measurement pressure. Thus the reaction between MgH<sub>2</sub> and CO<sub>2</sub> can be presented as follows.



\* other gases to be further confirmed

Due to the interaction of Mg/MgH<sub>2</sub> with (H<sub>2</sub>+ CO<sub>2</sub>) mixed gas. Mg, as a H<sub>2</sub> storage media, cannot tolerate the CO<sub>2</sub> impurities in a hydrogen flow gas, seen Section 4.5. It is of interest to note that the reactions of CO<sub>2</sub> on MgH<sub>2</sub> are of great importance for several reasons: (i) CO<sub>2</sub> is of interest as a reactant in hydrocarbon synthesis. (ii) CO<sub>2</sub> is to a large extent responsible for the green house effect and therefore contributes to global warming; the reduction of CO<sub>2</sub> or, alternatively, its conversion into more valuable chemicals, such as hydrocarbons, methanol and others, is therefore of considerable interest. (iii) The activation of CO<sub>2</sub> at biological surfaces involves metal complexes.<sup>179, 181, 182</sup>

## CHAPTER 6 CONCLUSIONS AND FUTURE WORK

### 6.1 Conclusions

A systematic investigation was carried out on the sorption properties and structural stability of  $\text{MgH}_2$  modified by a range of mechanical milling conditions and chemical additions. The influences of cryogenic milling and ball milling on particle size and grain size, microstructure and phase composition of materials were characterized using X-Ray diffraction, SEM and TEM. The effects of selected transition metal carbides on dehydrogenation/hydrogenation of  $\text{MgH}_2$  were evaluated by TG and DTG. The findings are very useful in the development of new Mg-based hydrogen storage materials with rapid kinetics and lower desorption temperature, and the exploitation of an effective and stable catalyst to improve hydrogen sorption properties. The following conclusions were drawn from the investigation.

- 1) Cryogenic milling is very effective in reducing the grain and particle sizes of  $\text{MgH}_2$ . The smallest mean powder particle size achieved in this work by 8 h cryogenic milling was  $190 \pm 20$  nm.
- 2) The onset and peak desorption temperatures of  $\text{MgH}_2$  were substantially reduced to 320 and 362 °C, respectively, by 8 h cryogenic milling, due to smaller and more uniform nano-scaled particles achieved under the cryogenic condition. The hydrogen absorption of dehydrogenated  $\text{MgH}_2$  is also enhanced by both cryogenic milling and ball-milling.
- 3) Hydrogen sorption of  $\text{MgH}_2$  catalysed with 2 mol % and 8 mol % TiC by cryomilling and ball-milling was investigated. The formation of  $\gamma\text{-MgH}_2$  during high energy ball milling of  $\text{MgH}_2$  was observed from XRD patterns. The crystallite sizes of  $\text{MgH}_2$  decreased significantly after cryomilling. TiC, which is a very stable

compounds under the testing temperature and pressure ( $< 500$  °C, 1 bar He or 8 bar  $H_2$ ), and retained original form during milling and after dehydrogenation, there is no reaction found between Mg/MgH<sub>2</sub> and TiC. From SEM-BSE and TEM observations, the nanometer-sized TiC particles were either distributed on the surface of MgH<sub>2</sub> particles or inserted between grains of MgH<sub>2</sub>, which enhanced the interaction between MgH<sub>2</sub> and TiC.

- 4) TiC shows an effective catalyst for H<sub>2</sub> sorption of Mg/MgH<sub>2</sub>. It was also found that a higher TiC content of 8 mol % reduced the onset desorption temperature further to 175 °C, compared with 2 mol % TiC (190 °C). The Mo<sub>2</sub>C shows no catalytic effect on hydrogen sorption of MgH<sub>2</sub>.
- 5) A preliminary study of hydrogen sorption using a (H<sub>2</sub> + CO<sub>2</sub>) mixture strongly indicates that CO<sub>2</sub> poisons the hydrogen sorption process of Mg due to chemical reactions that generate solid phases and other gaseous species, such as MgO, MgCO<sub>3</sub>, CO, CH<sub>4</sub> and H<sub>2</sub>O.

## 6.2 Future Work

From the present findings, a number of issues should be investigated further, including the in-depth understanding of the current systems and development of new gas sorption systems.

In particular, the following lines of development should be pursued further:

- 1) The cyclability (stable H<sub>2</sub> storage capacity and microstructure upon cycling) of a hydrogen storage material is very important for reversible hydrogen charge/discharge in practical applications. The cyclic tests of the optimized materials, e.g. (MgH<sub>2</sub>+TiC) mixture, should be carried out in future investigation.
- 2) To synthesize MgH<sub>2</sub> with higher content of TiC to reduce the desorption temperature and improve the absorption kinetics further. The optimum TiC content

in  $\text{MgH}_2$  for lower desorption temperature, fast sorption kinetics and high capacity should be investigated.

- 3) To investigate the effect of other transition metal carbide, such as VC, WC and FeC, on hydrogen sorption properties of  $\text{MgH}_2$ .
- 4) To further study the reaction mechanism of  $\text{Mg}/\text{MgH}_2$  with  $\text{H}_2/\text{CO}_2$  mixture at different temperatures. The results should provide valuable information for gas separation in syngas stream and  $\text{CO}_2$  capture/storage, where  $\text{H}_2$  could be effectively stored in Mg catalyzed by transition metal carbide at one range of temperature,  $\text{CO}_2$  at another; it will be also interesting to study capture or separation of  $\text{H}_2$  from other gas mixtures, e.g.  $\text{H}_2/\text{CH}_4$ ,  $\text{H}_2/\text{CO}_2/\text{CO}$ .

## REFERENCES

1. Dresselhaus MS and Thomas IL, Alternative energy technologies. *Nature* **414**:332-337 (2001).
2. Sakintuna B, Lamari-Darkrim F and Hirscher M, Metal hydride materials for solid hydrogen storage: A review. *International Journal of Hydrogen Energy* **32**:1121-1140 (2007).
3. Metz B, Intergovernmental Panel on Climate Change: Special Report on CO<sub>2</sub> Capture and Storage (2005).
4. Raupach MR, Marland G, Ciais P, Canadell JG, Klepper G and Field CB, Global and regional drivers of accelerating CO<sub>2</sub> emissions. *Proceedings of the National Academy of Sciences* **104**:10288-10293 (2007).
5. Jain IP, Lal C and Jain A, Hydrogen storage in Mg: A most promising material. *International Journal of Hydrogen Energy* **35**:5133-5144 (2010).
6. Balema V, Hydrogen Storage Materials. *Material Matters* **2**:2 (2007).
7. Davis M, Balog F and Ogden J, National Hydrogen Energy Roadmap. United States Department of Energy, pp. available at: [http://www.hydrogen.energy.gov/pdfs/national\\_h2\\_roadmap.pdf](http://www.hydrogen.energy.gov/pdfs/national_h2_roadmap.pdf) (2002).
8. energy Usdo, A national vision of america's transition to a hydrogen economy- to 2030 and beyond. United states department of energy, pp. 35 (2002).
9. <http://www.energy.gov/>, <http://www.energy.gov/>.
10. [http://www.hydrogen.energy.gov/annual\\_progress09.html](http://www.hydrogen.energy.gov/annual_progress09.html).
11. [http://www1.eere.energy.gov/hydrogenandfuelcells/pdfs/freedomcar\\_targets\\_explanations.pdf](http://www1.eere.energy.gov/hydrogenandfuelcells/pdfs/freedomcar_targets_explanations.pdf).
12. Michael U. Niemann SSS, Ayala R. Phani, Ashok Kumar, D. Yogi Goswami, and Elias K. Stefanakos, Nanomaterials for Hydrogen Storage Applications: A Review. *Journal of Nanomaterials* **2008**:9 (2008).
13. Shang CX, Bououdina M, Song Y and Guo ZX, Mechanical alloying and electronic simulations of (MgH<sub>2</sub>+M) systems (M=Al, Ti, Fe, Ni, Cu and Nb) for hydrogen storage. *International Journal of Hydrogen Energy* **29**:73-80 (2004).
14. Varin RA, Czujko T and Wronski Z, Particle size, grain size and  $\gamma$ -MgH<sub>2</sub> effects on the desorption properties of nanocrystalline commercial magnesium hydride processed by controlled mechanical milling. *Nanotechnology*:3856 (2006).
15. Ranjbar A, Guo ZP, Yu XB, Wexler D, Calka A, Kim CJ and Liu HK, Hydrogen storage properties of MgH<sub>2</sub>-SiC composites. *Materials Chemistry and Physics* **114**:168-172 (2009).
16. Shin JH, Lee G-J, Cho YW and Lee KS, Improvement of hydrogen sorption properties of MgH<sub>2</sub> with various sizes and stoichiometric compositions of TiC. *Catalysis Today* **146**:209-215 (2009).
17. Ma L-P, Wang P, Dai H-B and Cheng H-M, Catalytically enhanced dehydrogenation of Li-Mg-N-H hydrogen storage material by transition metal nitrides. *Journal of Alloys and Compounds* **468**:L21-L24 (2009).
18. Liang G, Huot J, Boily S, Van Neste A and Schulz R, Catalytic effect of transition metals on hydrogen sorption in nanocrystalline ball milled MgH<sub>2</sub>-Tm (Tm=Ti, V, Mn, Fe and Ni) systems. *Journal of Alloys and Compounds* **292**:247-252 (1999).
19. Barkhordarian G, Klassen T and Bormann R, Fast hydrogen sorption kinetics of nanocrystalline Mg using Nb<sub>2</sub>O<sub>5</sub> as catalyst. *Scripta Materialia* **49**:213-217 (2003).

20. Barkhordarian G, Klassen T and Bormann R, Catalytic Mechanism of Transition-Metal Compounds on Mg Hydrogen Sorption Reaction. *The Journal of Physical Chemistry B* **110**:11020-11024 (2006).
21. Ping W, Xiang Dong K and Hui Ming C, Improved Hydrogen Storage of TiF<sub>3</sub>-Doped NaAlH<sub>4</sub>. *ChemPhysChem* **6**:2488-2491 (2005).
22. Kang X-D, Wang P and Cheng H-M, Advantage of TiF<sub>3</sub> over TiCl<sub>3</sub> as a dopant precursor to improve the thermodynamic property of Na<sub>3</sub>AlH<sub>6</sub>. *Scripta Materialia* **56**:361-364 (2007).
23. Zheng S, Fang F, Zhang J, Sun L, He B, Wei S, Chen G and Sun D, Study of the Correlation between the Stability of Mg-Based Hydride and the Ti-Containing Agent. *The Journal of Physical Chemistry C* **111**:14021-14025 (2007).
24. Fontes E and E.Nilsson, Modeling the fuel cell. *The Industrial Physicist* **7**:14 (2001).
25. B LW, H MN and H M, Primitive phase diagram for hydrogen. *Phys Lett* **56**:425-426 (1976).
26. RC W, Handbook of chemistry and physics, ed by Press C (1976).
27. Jain IP, Lal C and Jain A, Hydrogen storage in Mg: A most promising material. *International Journal of Hydrogen Energy* **35**:5133-5144 (2010).
28. Zuttel A, Materials for hydrogen storage. *Materials Today* **6**:24-33 (2003).
29. Ogden JM, Developing an infrastructure for hydrogen vehicles: a Southern California case study. *International Journal of Hydrogen Energy* **24**:709-730 (1999).
30. Schulz R, Huot J, Liang G, Boily S, Lalande G, Denis MC and Dodelet JP, Recent developments in the applications of nanocrystalline materials to hydrogen technologies. *Materials Science and Engineering A* **267**:240-245 (1999).
31. Darkrim FL, Malbrunot P and Tartaglia GP, Review of hydrogen storage by adsorption in carbon nanotubes. *International Journal of Hydrogen Energy* **27**:193-202 (2002).
32. Hirscher M, Becher M, Haluska M, von Zeppelin F, Chen X, Dettlaff-Weglikowska U and Roth S, Are carbon nanostructures an efficient hydrogen storage medium? *Journal of Alloys and Compounds* **356-357**:433-437 (2003).
33. Ockwig NW, Delgado-Friedrichs O, O'Keeffe M and Yaghi OM, Reticular Chemistry: Occurrence and Taxonomy of Nets and Grammar for the Design of Frameworks. *Accounts of Chemical Research* **38**:176-182 (2005).
34. Yaghi OM, O'Keeffe M, Ockwig NW, Chae HK, Eddaoudi M and Kim J, Reticular synthesis and the design of new materials. *Nature* **423**:705-714 (2003).
35. Rosseinsky MJ, Recent developments in metal-organic framework chemistry: design, discovery, permanent porosity and flexibility. *Microporous and Mesoporous Materials* **73**:15-30 (2004).
36. Bradshaw D, Prior TJ, Cussen EJ, Claridge JB and Rosseinsky MJ, Permanent Microporosity and Enantioselective Sorption in a Chiral Open Framework. *Journal of the American Chemical Society* **126**:6106-6114 (2004).
37. Eddaoudi M, Kim J, Rosi N, Vodak D, Wachter J, O'Keeffe M and Yaghi OM, Systematic Design of Pore Size and Functionality in Isoreticular MOFs and Their Application in Methane Storage. *Science* **295**:469-472 (2002).
38. Ferey G, Mellot-Draznieks C, Serre C and Millange F, Crystallized Frameworks with Giant Pores: Are There Limits to the Possible? *Accounts of Chemical Research* **38**:217-225 (2005).
39. Eddaoudi M, Li H and Yaghi OM, Highly Porous and Stable Metal-organic Frameworks: Structure Design and Sorption Properties. *Journal of the American Chemical Society* **122**:1391-1397 (2000).

40. Li H, Eddaoudi M, O'Keeffe M and Yaghi OM, Design and synthesis of an exceptionally stable and highly porous metal-organic framework. *Nature* **402**:276-279 (1999).
41. Rowsell JLC, Millward AR, Park KS and Yaghi OM, Hydrogen Sorption in Functionalized Metal-organic Frameworks. *Journal of the American Chemical Society* **126**:5666-5667 (2004).
42. Panella B and Hirscher M, Hydrogen Physisorption in Metal-Organic Porous Crystals. *Advanced Materials* **17**:538-541 (2005).
43. Panella B and Hirscher M, Hydrogen Adsorption in Metal-Organic Frameworks: Cu-MOFs and Zn-MOFs Compared. *Advanced Functional Materials* **16**:520-524 (2006).
44. Cheng S, Liu S, Zhao Q and Li J, Improved synthesis and hydrogen storage of a microporous metal-organic framework material. *Energy Conversion and Management* **50**:1314-1317 (2009).
45. Selvam P, Viswanathan B, Swamy CS and Srinivasan V, Magnesium and magnesium alloy hydrides. *International Journal of Hydrogen Energy* **11**:169-192 (1986).
46. Schlapbach L and Zuttel A, Hydrogen-storage materials for mobile applications. *Nature* **414**:353-358 (2001).
47. Bogdanovi B and Schwickardi M, Ti-doped alkali metal aluminium hydrides as potential novel reversible hydrogen storage materials. *Journal of Alloys and Compounds* **253-254**:1-9 (1997).
48. Orimo S-i, Nakamori Y, Eliseo JR and Jensen CM, Complex Hydrides for Hydrogen Storage. *Chemical Reviews* **107**:4111-4132 (2007).
49. Steinfeld A, Solar hydrogen production via a two-step water-splitting thermochemical cycle based on Zn/ZnO redox reactions. *International Journal of Hydrogen Energy* **27**:611-619 (2002).
50. Stan G and Cole MW, Hydrogen Adsorption in Nanotubes. *Journal of Low Temperature Physics* **110**:539-544 (1998).
51. Brunauer S, Emmett PH and Teller E, Adsorption of Gases in Multimolecular Layers. *Journal of the American Chemical Society* **60**:309-319 (1938).
52. Vincent B, Gregg R, Mildred D and Gang C, Size effects on the hydrogen storage properties of nanostructured metal hydrides: A review. *International Journal of Energy Research* **31**:637-663 (2007).
53. Song MY, Improvement in hydrogen storage characteristics of magnesium by mechanical alloying with nickel. *Journal of Materials Science* **30**:1343-1351 (1995).
54. Song MY, Ivanov EI, Darriet B, Pezat M and Hagenmuller P, Hydriding properties of a mechanically alloyed mixture with a composition Mg<sub>2</sub>Ni. *International Journal of Hydrogen Energy* **10**:169-178 (1985).
55. Song MY, Ivanov E, Darriet B, Pezat M and Hagenmuller P, Hydriding and dehydriding characteristics of mechanically alloyed mixtures Mg-xwt.%Ni (x = 5, 10, 25 and 55). *Journal of the Less Common Metals* **131**:71-79 (1987).
56. Song MY, Effects of mechanical alloying on the hydrogen storage characteristics of Mg-xwt% Ni (x = 0, 5, 10, 25 and 55) mixtures. *International Journal of Hydrogen Energy* **20**:221-227 (1995).
57. Bobet JL, Akiba E, Nakamura Y and Darriet B, Study of Mg-M (M=Co, Ni and Fe) mixture elaborated by reactive mechanical alloying -- hydrogen sorption properties. *International Journal of Hydrogen Energy* **25**:987-996 (2000).
58. Huot J, Tremblay ML and Schulz R, Synthesis of nanocrystalline hydrogen storage materials. *Journal of Alloys and Compounds* **356-357**:603-607 (2003).

59. Imamura H, Kusuhara M, Minami S, Matsumoto M, Masanari K, Sakata Y, Itoh K and Fukunaga T, Carbon nanocomposites synthesized by high-energy mechanical milling of graphite and magnesium for hydrogen storage. *Acta Materialia* **51**:6407-6414 (2003).
60. Oelerich W, Klassen T and Bormann R, Comparison of the catalytic effects of V, V<sub>2</sub>O<sub>5</sub>, VN, and VC on the hydrogen sorption of nanocrystalline Mg. *Journal of Alloys and Compounds* **322**:L5-L9 (2001).
61. Dehouche Z, Klassen T, Oelerich W, Goyette J, Bose TK and Schulz R, Cycling and thermal stability of nanostructured MgH<sub>2</sub>-Cr<sub>2</sub>O<sub>3</sub> composite for hydrogen storage. *Journal of Alloys and Compounds* **347**:319-323 (2002).
62. Yavari AR, LeMoulec A, de Castro FR, Deledda S, Friedrichs O, Botta WJ, Vaughan G, Klassen T, Fernandez A and Kwick A, Improvement in H-sorption kinetics of MgH<sub>2</sub> powders by using Fe nanoparticles generated by reactive FeF<sub>3</sub> addition. *Scripta Materialia* **52**:719-724 (2005).
63. W.M. M, Titanium Hydrides in Metal hydrides,, ed by W.M.Mueller, J.P.Blackledge and G.G.libowitz. Academic Press, New York, pp. 336 (1968).
64. Li Z, Jinghong M, Xinyuan Z and Borun L, Kinetics of thermal degradation of thermotropic poly(p-oxybenzoate-co-ethylene-2,6-naphthalate) by single heating rate methods. *Journal of Applied Polymer Science* **91**:3915-3920 (2004).
65. Dehouche Z, Goyette J, Bose TK, Huot J and Schulz R, Sensitivity of Nanocrystalline MgH<sub>2</sub>-V Hydride Composite to the Carbon Monoxide during a Long-Term Cycling. *Nano Letters* **1**:175-178 (2001).
66. Fan M-Q, Liu S-s, Zhang Y, Zhang J, Sun L-X and Xu F, Superior hydrogen storage properties of MgH<sub>2</sub>-10wt.% TiC composite. *Energy* **35**:3417-3421.
67. Stampfer JF, Holley CE and Suttle JF, The Magnesium-Hydrogen System1-3. *Journal of the American Chemical Society* **82**:3504-3508 (1960).
68. Ellinger FH, Holley CE, McInteer BB, Pavone D, Potter RM, Staritzky E and Zachariasen WH, The Preparation and Some Properties of Magnesium Hydride1. *Journal of the American Chemical Society* **77**:2647-2648 (1955).
69. Zachariasen WH, Holley CE and Stamper JFJ, Neutron diffraction study of magnesium deuteride. *Acta Crystallographica* **16**:352-353 (1963).
70. <http://upload.wikimedia.org/wikipedia/commons/a/a0/Magnesium-hydride-unit-cell-3D-balls.png>.
71. Bortz M, Bertheville B and Yvon K, Structure of the high pressure phase [gamma]-MgH<sub>2</sub> by neutron powder diffraction. *Journal of Alloys and Compounds* **287**:L4-L6 (1999).
72. Bastide J-P, Bonnetot B and Claudy P, Polymorphisme de l'hydrure de magnesium sous haute pression. *Materials Research Bulletin* **15**:1215-1224 (1980).
73. Gennari FC, Castro FJ and Urretavizcaya G, Hydrogen desorption behavior from magnesium hydrides synthesized by reactive mechanical alloying. *Journal of Alloys and Compounds* **321**:46-53 (2001).
74. Klyamkin S, Metal hydride compositions on the basis of magnesium as materials for hydrogen accumulation. *Russian Journal of General Chemistry* **77**:712-720 (2007).
75. Mushnikov N, Ermakov A, Uimin M, Gaviko V, Terent'ev P, Skripov A, Tankeev A, Soloninin A and Buzlukov A, Kinetics of interaction of Mg-based mechanically activated alloys with hydrogen. *The Physics of Metals and Metallography* **102**:421-431 (2006).
76. Dornheim M, Doppiu S, Barkhordarian G, Boesenberg U, Klassen T, Gutfleisch O and Bormann R, Hydrogen storage in magnesium-based hydrides and hydride composites. *Scripta Materialia* **56**:841-846 (2007).

77. Zaluska A and Zaluski L, Nanocrystalline magnesium for hydrogen storage. *Journal of Alloys and Compounds* **288**:217-225 (1999).
78. Manchester FD and Khatamian D, *Materials Science Forum* **31**:261-296 (2008).
79. Luz Z, Genossar J and Rudman PS, Identification of the diffusing atom in MgH<sub>2</sub>. *Journal of the Less Common Metals* **73**:113-118 (1980).
80. Vigeholm B, Jensen K, Larsen B and Pedersen, Elements of hydride formation mechanisms in nearly spherical magnesium powder particles. *Journal of the Less Common Metals* **131**:133-141 (1987).
81. Vigeholm B, Larsen B and Pedersen AS, Formation and decomposition of magnesium hydride. *Journal of the Less Common Metals* **89**:135-144 (1983).
82. Stioui M, Grayevsky A, Resnik A, Shaltiel D and Kaplan N, Macroscopic and microscopic kinetics of hydrogen in magnesium-rich compounds. *Journal of The Less-Common Metals* **123**:9-24 (1986).
83. Rydn J, Hjrvarsson B, Ericsson T, Karlsson E, Krozer A and Kasemo B, *Z Phys Chem* **1684**:1259 (1989).
84. Li Z, Liu X, Jiang L and Wang S, Characterization of Mg-20 wt% Ni-Y hydrogen storage composite prepared by reactive mechanical alloying. *International Journal of Hydrogen Energy* **32**:1869-1874 (2007).
85. Liu X, Huang Z, Jiang L and Wang S, Thermal stabilization and hydrogen storage properties of Mg-40 wt% Ti<sub>0.28</sub>Cr<sub>0.50</sub>V<sub>0.22</sub> composite prepared by mechanical milling. *International Journal of Hydrogen Energy* **32**:965-968 (2007).
86. Imamura H, Yoshihara K, Yoo M, Kitazawa I, Sakata Y and Ooshima S, Dehydriding of Sn / MgH<sub>2</sub> nanocomposite formed by ball milling of MgH<sub>2</sub> with Sn. *International Journal of Hydrogen Energy* **32**:4191-4194 (2007).
87. Liu D, Zhu Y and Li L, Mechanism of the high activity of Mg<sub>2</sub>NiH<sub>4</sub> produced by hydriding combustion synthesis based on the analysis of phase composition, particle characteristic and grain size. *International Journal of Hydrogen Energy* **32**:2455-2460 (2007).
88. Aguey-Zinsou KF, Ares Fernandez JR, Klassen T and Bormann R, Effect of Nb<sub>2</sub>O<sub>5</sub> on MgH<sub>2</sub> properties during mechanical milling. *International Journal of Hydrogen Energy* **32**:2400-2407 (2007).
89. Ha W, Lee HS, Youn JI, Hong TW and Kim YJ, Hydrogenation and degradation of Mg-10 wt% Ni alloy after cyclic hydriding-dehydriding. *International Journal of Hydrogen Energy* **32**:1885-1889 (2007).
90. Xie L, Shao HY, Wang YT, Li Y and Li XG, Synthesis and hydrogen storing properties of nanostructured ternary Mg-Ni-Co compounds. *International Journal of Hydrogen Energy* **32**:1949-1953 (2007).
91. Huang ZG, Guo ZP, Calka A, Wexler D and Liu HK, Effects of carbon black, graphite and carbon nanotube additives on hydrogen storage properties of magnesium. *Journal of Alloys and Compounds* **427**:94-100 (2007).
92. Loken S, Solberg JK, Maehlen JP, Denys RV, Lototsky MV, Tarasov BP and Yartys VA, Nanostructured Mg-Mn-Ni hydrogen storage alloy: Structure-properties relationship. *Journal of Alloys and Compounds* **446-447**:114-120 (2007).
93. Ma LP, Wang P and Cheng HM, Improving hydrogen sorption kinetics of MgH<sub>2</sub> by mechanical milling with TiF<sub>3</sub>. *Journal of Alloys and Compounds* **432** (2007).
94. Kwon S, Baek S, Mumm DR, Hong SH and Song M, Enhancement of the hydrogen storage characteristics of Mg by reactive mechanical grinding with Ni, Fe and Ti. *International Journal of Hydrogen Energy* **33**:4586-4592 (2008).
95. Polanski M, Bystrzycki J and Plocinski T, The effect of milling conditions on microstructure and hydrogen absorption/desorption properties of magnesium

- hydride ( $\text{MgH}_2$ ) without and with  $\text{Cr}_2\text{O}_3$  nanoparticles. *International Journal of Hydrogen Energy* **33**:1859-1867 (2008).
96. Rud AD, Lakhnik AM, Ivanchenko VG, Uvarov VN, Shkola AA, Dekhtyarenko VA, Ivaschuk LI and Kuskova NI, Hydrogen storage of the Mg-C composites. *International Journal of Hydrogen Energy* **33**:1310-1316 (2008).
  97. Luo Y, Wang P, Ma LP and Cheng HM, Hydrogen sorption kinetics of  $\text{MgH}_2$  catalyzed with  $\text{NbF}_5$ . *Journal of Alloys and Compounds* **453**:138-142 (2008).
  98. Li F, Jiang L, Du J, Wang S, Liu X and Zhan F, Investigations on synthesis and hydrogenation properties of Mg-20 wt% Ni-1 wt%  $\text{TiO}_2$  composite prepared by reactive mechanical alloying. *Journal of Alloys and Compounds* **452**:421-424 (2008).
  99. Gupta R, Agresti F, Russo SL, Maddalena A, Palade P and Principi G, Structure and hydrogen storage properties of  $\text{MgH}_2$  catalysed with  $\text{La}_2\text{O}_3$ . *Journal of Alloys and Compounds* **450**:310-313 (2008).
  100. Fu Y, Groll M, Mertz R and Kulenovic R, Effect of  $\text{LaNi}_5$  and additional catalysts on hydrogen storage properties of Mg. *Journal of Alloys and Compounds* **460**:607-613 (2008).
  101. Song MY, Yim CD, Bae JS, Mumm DR and Hong SH, Preparation by gravity casting and hydrogen-storage properties of Mg-23.5 wt.% Ni-(5, 10 and 15 wt.%)La. *Journal of Alloys and Compounds* **463**:143-147 (2008).
  102. Molinas B, Ghilarducci AA, Melnichuk M, Corso HL, Peretti HA, Agresti F, Bianchin A, Lo Russo S, Maddalena A and Principi G, Scaled-up production of a promising Mg-based hydride for hydrogen storage. *International Journal of Hydrogen Energy* **34**:4597-4601 (2009).
  103. Gu H, Zhu Y and Li L, Hydrogen storage properties of Mg-30 wt.%  $\text{LaNi}_5$  composite prepared by hydriding combustion synthesis followed by mechanical milling (HCS + MM). *International Journal of Hydrogen Energy* **34**:1405-1410 (2009).
  104. Patah A, Takasaki A and Szmyd JS, Influence of multiple oxide ( $\text{Cr}_2\text{O}_3\text{Nb}_2\text{O}_5$ ) addition on the sorption kinetics of  $\text{MgH}_2$ . *International Journal of Hydrogen Energy* **34**:3032-3037 (2009).
  105. Tonus F, Fuster V, Urretavizcaya G, Castro FJ and Bobet JL, Catalytic effect of monoclinic  $\text{WO}_3$ , hexagonal  $\text{WO}_3$  and  $\text{H}_{0.23}\text{WO}$  on the hydrogen sorption properties of Mg. *International Journal of Hydrogen Energy* **34**:3404-3409 (2009).
  106. Xie DH, Li P, Zeng CX, Sun JW and Qu XH, Effect of substitution of Nd for Mg on the hydrogen storage properties of  $\text{Mg}_2\text{Ni}$  alloy. *Journal of Alloys and Compounds* **478**:96-102 (2009).
  107. Ma L-P, Wang P and Cheng H-M, Hydrogen sorption kinetics of  $\text{MgH}_2$  catalyzed with titanium compounds. *International Journal of Hydrogen Energy* **In Press, Corrected Proof**.
  108. Lu J, Qin J, Lu W, Zhang D, Hou H and Li Z, Effect of hydrogen on microstructure and high temperature deformation of (TiB+TiC)/Ti-6Al-4V composite. *Materials Science and Engineering: A* **500**:1-7 (2009).
  109. Vigeholm B, Larsen B and Pedersen AS, Formation and decomposition of magnesium hydride. *Journal of The Less-Common Metals* **89**:135-144 (1983).
  110. Sholl DS, Using density functional theory to study hydrogen diffusion in metals: A brief overview. *Journal of Alloys and Compounds* **446-447**:462-468 (2007).
  111. Berlouis LEA, Cabrera E, Hall-Barientos E, Hall PJ, Dodd SB, Morris S and Imam MA, Thermal analysis investigation of hydriding properties of nanocrystalline Mg-

- Ni- and Mg-Fe-based alloys prepared by high-energy ball milling. *Journal of Materials Research* **16**:45-57 (2001).
112. Shang CX and Guo ZX, Structural and desorption characterisations of milled ( $\text{MgH}_2 + \text{Y}$ , Ce) powder mixtures for hydrogen storage. *International Journal of Hydrogen Energy* **32**:2920-2925 (2007).
113. Zaluska A, Zaluski L and Strm-Olsen JO, Synergy of hydrogen sorption in ball-milled hydrides of Mg and  $\text{Mg}_2\text{Ni}$ . *Journal of Alloys and Compounds* **289**:197-206 (1999).
114. Wagemans RWP, Van Lenthe JH, De Jongh PE, Van Dillen AJ and De Jong KP, Hydrogen storage in magnesium clusters: Quantum chemical study. *Journal of the American Chemical Society* **127**:16675-16680 (2005).
115. Huot J, Akiba E and Takada T, Mechanical alloying of MgNi compounds under hydrogen and inert atmosphere. *Journal of Alloys and Compounds* **231**:815-819 (1995).
116. Zaluska A, Zaluski L, Nanocrystalline magnesium for hydrogen storage. *Journal of Alloys and Compounds* **288**:217-225 (1999).
117. Segal VM, Reznikov VI, Drobyshevskiy AE and Kopylov VI, Plastic working of metals by simple shear. *Russ Metall* **1**:99-105 (1981).
118. Skripnyuk VM, Rabkin E, Estrin Y and Lapovok R, Improving hydrogen storage properties of magnesium based alloys by equal channel angular pressing. *International Journal of Hydrogen Energy* **34**:6320-6324 (2009).
119. Reilly JJ and Wiswall Jr RH, The reaction of hydrogen with alloys of magnesium and nickel and the formation of  $\text{Mg}_2\text{NiH}_4$ . *Inorganic Chemistry* **7**:2254-2256 (1968).
120. Janot R, Aymard L, Rougier A, Nazri GA and Tarascon JM, Enhanced hydrogen sorption capacities and kinetics of  $\text{Mg}_2\text{Ni}$  alloys by ball-milling with carbon and Pd coating. *Journal of Materials Research* **18**:1749-1752 (2003).
121. Kodera Y, Yamasaki N, Yamamoto T, Kawasaki T, Ohyanagi M and Munir ZA, Hydrogen storage  $\text{Mg}_2\text{Ni}$  alloy produced by induction field activated combustion synthesis. *Journal of Alloys and Compounds* **446-447**:138-141 (2007).
122. Pozzo M and Alfe D, Structural properties and enthalpy of formation of magnesium hydride from quantum Monte Carlo calculations. *Phys Rev B* **77**:104103 (2008).
123. Semenenko KN, Verbetskii VN and Kuliev SI, Hydriding of Magnesium Alloys. *Zh Neorg Khim* **29**:2192-2194 (1984).
124. Kuliev SI, Klyamkin SN, Verbetskii VN, Gasan-Zade AA and Semenenko KN, Interaction between hydrogen and magnesium-misch metal-nickel, *metally* **1** (1988).
125. Ren Hp, Zhang Yh, Li Bw, Zhao Dl, Guo Sh and Wang Xi, Influence of the substitution of La for Mg on the microstructure and hydrogen storage characteristics of  $\text{Mg}_{20-x}\text{La}_x\text{Ni}_{10}$  ( $x = 0-6$ ) alloys. *International Journal of Hydrogen Energy* **34**:1429-1436 (2009).
126. Zuttel A, Wenger P, Rentsch S, Sudan P, Mauron P and Emmenegger C,  $\text{LiBH}_4$  a new hydrogen storage material. *Journal of Power Sources* **118**:1-7 (2003).
127. Porutsky SG, Zhurakovskiy EA, Mogilevskiy SA, Verbetsky VN, Bakuma OS and Semenenko KN, Electronic structure of  $\text{Mg}_2\text{FeH}_6$  and  $\text{Mg}_2\text{CoH}_5$  hydrides and binding role of hydrogen in them. *Solid State Communications* **74**:551-553 (1990).
128. Kalisvaart WP, Niessen RAH and Notten PHL, Electrochemical hydrogen storage in MgSc alloys: A comparative study between thin films and bulk materials. *Journal of Alloys and Compounds* **417**:280-291 (2006).
129. Andreasen A, Hydrogenation properties of Mg-Al alloys. *International Journal of Hydrogen Energy* **33**:7489-7497 (2008).

130. Crivello JC, Nobuki T and Kuji T, Improvement of Mg-Al alloys for hydrogen storage applications. *International Journal of Hydrogen Energy* **34**:1937-1943 (2009).
131. Crivello JC, Nobuki T, Kato S, Abe M and Kuji T, Hydrogen absorption properties of the Y-Mg<sub>17</sub>Al<sub>12</sub> phase and its Al-rich domain. *Journal of Alloys and Compounds* **446-447**:157-161 (2007).
132. Hanada N, Ichikawa T and Fujii H, Catalytic effect of nanoparticle 3d-transition metals on hydrogen storage properties in magnesium hydride MgH<sub>2</sub> prepared by mechanical milling. *Journal of Physical Chemistry B* **109**:7188-7194 (2005).
133. Yermakov AY, Mushnikov NV, Uimin MA, Gaviko VS, Tankeev AP, Skripov AV, Soloninin AV and Buzlukov AL, Hydrogen reaction kinetics of Mg-based alloys synthesized by mechanical milling. *Journal of Alloys and Compounds* **425**:367-372 (2006).
134. Dufour J and Huot J, Rapid activation, enhanced hydrogen sorption kinetics and air resistance in laminated Mg-Pd 2.5 at.%. *Journal of Alloys and Compounds* **439** (2007).
135. Friedrichs O, Aguey-Zinsou F, Justo A, Klassen T and Bormann R, MgH<sub>2</sub> with Nb<sub>2</sub>O<sub>5</sub> as additive, for hydrogen storage: Chemical, structural and kinetic behavior with heating. *Acta Materialia* **54**:105-110 (2006).
136. Reda MR, The effect of organic additive in Mg/graphite composite as hydrogen storage materials. *Journal of Alloys and Compounds* **480**:238-240 (2009).
137. Lu K, Nanocrystalline metals crystallized from amorphous solids: Nanocrystallization, structure, and properties. *Materials Science and Engineering R: Reports* **16**:161-221 (1996).
138. Terzieva M, Khrussanova M and Peshev P, Hydriding and dehydriding characteristics of Mg-LaNi<sub>5</sub> composite materials prepared by mechanical alloying. *Journal of Alloys and Compounds* **267**:235-239 (1998).
139. Xie L, Liu Y, Zhang X, Qu J, Wang Y and Li X, Catalytic effect of Ni nanoparticles on the desorption kinetics of MgH<sub>2</sub> nanoparticles. *Journal of Alloys and Compounds* **482**:388-392 (2009).
140. Hanada N, Ichikawa T, Hino S and Fujii H, Remarkable improvement of hydrogen sorption kinetics in magnesium catalyzed with Nb<sub>2</sub>O<sub>5</sub>. *Journal of Alloys and Compounds* **420**:46-49 (2006).
141. Bhat VV, Rougier A, Aymard L, Nazri GA and Tarascon JM, High surface area niobium oxides as catalysts for improved hydrogen sorption properties of ball milled MgH<sub>2</sub>. *Journal of Alloys and Compounds* **460**:507-512 (2008).
142. Ranjbar A, Guo ZP, Yu XB, Attard D, Calka A and Liu HK, Effects of SiC nanoparticles with and without Ni on the hydrogen storage properties of MgH<sub>2</sub>. *International Journal of Hydrogen Energy* **34**:7263-7268 (2009).
143. Makihara Y, Umeda K, Shoji F, Kato K and Miyairi Y, Cooperative dehydriding mechanism in a mechanically milled Mg-50 mass% ZrMn<sub>2</sub> composite. *Journal of Alloys and Compounds* **455**:385-391 (2008).
144. Vijay R, Sundaresan R, Maiya MP, Murthy SS, Fu Y, Klein HP and Groll M, Characterisation of Mg-x wt.% FeTi (x = 5-30) and Mg-40 wt.% FeTiMn hydrogen absorbing materials prepared by mechanical alloying. *Journal of Alloys and Compounds* **384**:283-295 (2004).
145. Yu XB, Guo YH, Yang H, Wu Z, Grant DM and Walker GS, Improved hydrogen storage in magnesium hydride catalyzed by nanosized Ti<sub>0.4</sub>Cr<sub>0.15</sub>Mn<sub>0.15</sub>V<sub>0.3</sub> alloy. *Journal of Physical Chemistry C* **113**:5324-5328 (2009).

146. Barkhordarian G, Klassen T, Dornheim M and Bormann R, Unexpected kinetic effect of MgB<sub>2</sub> in reactive hydride composites containing complex borohydrides. *Journal of Alloys and Compounds* **440** (2007).
147. Lim KL, Kazemian H, Yaakob Z and Daud WRW, Solid-state Materials and Methods for Hydrogen Storage: A Critical Review. *Chemical Engineering & Technology* **33**:213-226 (2009).
148. Kalia S, Cryogenic Processing: A Study of Materials at Low Temperatures. *Journal of Low Temperature Physics*:934-945 (2009).
149. De Jongh PE, Wagemans RWP, Eggenhuisen TM, Dauvillier BS, Radstake PB, Meeldijk JD, Geus JW and De Jong KP, The preparation of carbon-supported magnesium nanoparticles using melt infiltration. *Chemistry of Materials* **19**:6052-6057 (2007).
150. Joo SH, Choi SJ, Oh I, Kwak J, Liu Z, Terasaki O and Ryoo R, Ordered nanoporous arrays of carbon supporting high dispersions of platinum nanoparticles. *Nature* **412**:169-172 (2001).
151. Li S-B, Xiang W-H, Zhai H-X and Zhou Y, Formation of TiC hexagonal platelets and their growth mechanism. *Powder Technology* **185**:49-53 (2008).
152. [www.spexcsp.com](http://www.spexcsp.com).
153. Suryanarayana C, Mechanical alloying and milling. *Progress in Materials Science* **46**:1-184 (2001).
154. CHAN JH and T.BALKE S, The thermal degradation kinetics of polypropylene : Part III. Thermogravimetric analyses. *Polymer degradation and stability* **57**:135-149 (1997).
155. Qipeng G, Phase behaviour in epoxy resin containing phenolphthalein poly(ether ether sulphone). *Polymer* **34**:70-76 (1993).
156. Guo M and Brittain WJ, Structure and Properties of Naphthalene-Containing Polyesters. 4. New Insight into the Relationship of Transesterification and Miscibility. *Macromolecules* **31**:7166-7171 (1998).
157. Wally LC, Decomposition behavior of polyurethanes via mathematical simulation. *Journal of Applied Polymer Science* **53**:1759-1769 (1994).
158. Varin RA and et al., Particle size, grain size and gamma-MgH<sub>2</sub> effects on the desorption properties of nanocrystalline commercial magnesium hydride processed by controlled mechanical milling. *Nanotechnology* **17**:3856 (2006).
159. Huot J, Liang G, Boily S, Van Neste A and Schulz R, Structural study and hydrogen sorption kinetics of ball-milled magnesium hydride. *Journal of Alloys and Compounds* **293-295**:495-500 (1999).
160. Kojima Y KY and Haga T, *J. Alloys Compounds*. (2006).
161. Varin RA, Czujko T and Wronski Z, Particle size, grain size and gamma-MgH<sub>2</sub> effects on the desorption properties of nanocrystalline commercial magnesium hydride processed by controlled mechanical milling. *Nanotechnology*:3856-3865 (2006).
162. Fecht HJ, Nanostructure formation by mechanical attrition. *Nanostructured Materials* **6**:33-42 (1995).
163. Varin R A, T. C, Ch C and Wronski Z, *J. Alloys Compounds*. (2006).
164. Schimmel H G HJCLCTFD and Mulder FM, *J. Am. Chem. Soc.* **127**:14348 (2005).
165. Zaluska A and Zaluski L, Synergy of hydrogen sorption in ball-milled hydrides of Mg and Mg<sub>2</sub>Ni. *Journal of Alloys and Compounds* **289**:197-206 (1999).
166. Suryanaraayana. C, Mechanical alloying and milling. *ProgMater Sci* (2001).
167. Andrew P. E. York, John B. Claridge, Attila J. Brungs, Tsang SC and Green MLH, Molybdenum and tungsten carbides as catalysts for the conversion of methane to synthesis gas using stoichiometric feedstocks. *Chem Commun*:39-40 (1997).

168. Bououdina M, de Rango P, Fruchart D and Soubeyroux JL, Pressure-composition measurements and microstructural analysis of the Laves phases  $Zr(Cr_{0.5}Mo_{0.2}M_{0.3})_2$  with  $M=Fe, Co, Ni$ . *Journal of Alloys and Compounds* **253-254**:221-225 (1997).
169. Iwase K, Nakamura Y, Mori K, Harjo S, Ishigaki T, Kamiyama T and Akiba E, Hydrogen absorption-desorption properties and crystal structure analysis of Ti-Cr-Mo alloys. *Journal of Alloys and Compounds* **404-406**:99-102 (2005).
170. Huot J, Akiba E and Takada T, Mechanical alloying of Mg--Ni compounds under hydrogen and inert atmosphere. *Journal of Alloys and Compounds* **231**:815-819 (1995).
171. Tessier P and Akiba E, Catalysed reactive milling. *Journal of Alloys and Compounds* **293-295**:400-402 (1999).
172. Doppiu S, Solsona P, Spassov T, Barkhordarian G, Dornheim M, Klassen T and Bar MD, Thermodynamic properties and absorption-desorption kinetics of  $Mg_{87}Ni_{10}Al_3$  alloy synthesised by reactive ball milling under  $H_2$  atmosphere. *Journal of Alloys and Compounds* **404-406**:27-30 (2005).
173. Doppiu S, Schultz L and Gutfleisch O, In situ pressure and temperature monitoring during the conversion of Mg into  $MgH_2$  by high-pressure reactive ball milling. *Journal of Alloys and Compounds* **427**:204-208 (2007).
174. Hanada N, Ichikawa T and Fujii H, Catalytic Effect of Nanoparticle 3d-Transition Metals on Hydrogen Storage Properties in Magnesium Hydride  $MgH_2$  Prepared by Mechanical Milling. *The Journal of Physical Chemistry B* **109**:7188-7194 (2005).
175. Rostrup-Nielsen JR, Sehested J and K. J, Hydrogen and synthesis gas by steam- and  $CO_2$  reforming, in *Advances in Catalysis*. Academic Press, pp. 65-139 (2002).
176. Hu YH, Ruckenstein E, Bruce CG and Helmut K, Catalytic Conversion of Methane to Synthesis Gas by Partial Oxidation and  $CO_2$  Reforming, in *Advances in Catalysis*. Academic Press, pp. 297-345 (2004).
177. Hu YH and Ruckenstein E, Steam-Reforming Product ( $H_2/CO_2$  Mixture) Used as a Hydrogen Source for Hydrogen Storage in  $Li_3N$ . *Industrial & Engineering Chemistry Research* **46**:5940-5942 (2007).
178. Sakadjian BB, Iyer MV, Gupta H and Fan L-S, Kinetics and Structural Characterization of Calcium-Based Sorbents Calcined under Subatmospheric Conditions for the High-Temperature  $CO_2$  Capture Process. *Industrial & Engineering Chemistry Research* **46**:35-42 (2006).
179. Pacchioni G, Physisorbed and chemisorbed  $CO_2$  at surface and step sites of the  $MgO(100)$  surface. *Surface Science* **281**:207-219 (1993).
180. Pacchioni G, Ricart JM and Illas F, Ab Initio Cluster Model Calculations on the Chemisorption of  $CO_2$  and  $SO_2$  Probe Molecules on  $MgO$  and  $CaO(100)$  Surfaces. A Theoretical Measure of Oxide Basicity. *Journal of the American Chemical Society* **116**:10152-10158 (1994).
181. Ochs D, Brause M, Braun B, Maus-Friedrichs W and Kemper V,  $CO_2$  chemisorption at Mg and  $MgO$  surfaces: a study with MIES and UPS (He I). *Surface Science* **397**:101-107 (1998).
182. Lesar A, Prebil S and Milan, Enthalpy of the Gas-Phase  $CO_2 + Mg$  Reaction from ab Initio Total Energies. *Journal of Chemical Information and Computer Sciences* **42**:853-857 (2002).
183. Raiche GA and Belbruno JJ, Laser-assisted chemistry in the reaction  $Mg+CO_2 \rightarrow MgO+CO$ . *Chemical Physics Letters* **146**:52-57 (1988).
184. Scherrer P, Bestimmung der Grösse und der inneren Struktur von Kolloidteilchen mittels Röntgenstrahlen. *Göttinger Nachrichten Gesell* **2**:98 (1918).
185. Suryanarayana. C, Mechanical alloying and milling. *ProgMater Sci* (2001).

186. Kalia S, Cryogenic Processing: A Study of Materials at Low Temperatures. *Journal of Low Temperature Physics* (2009).
187. Chung KH, He J, Shin DH and Schoenung JM, Mechanisms of microstructure evolution during cryomilling in the presence of hard particles. *Materials Science and Engineering A* **356**:23-31 (2003).
188. Varin RA, Czujko T, Chiu C and Wronski Z, Particle size effects on the desorption properties of nanostructured magnesium dihydride (MgH<sub>2</sub>) synthesized by controlled reactive mechanical milling (CRMM). *Journal of Alloys and Compounds* **424**:356-364 (2006).
189. Reule H and Hirscher M, Hydrogen desorption properties of mechanically alloyed MgH<sub>2</sub> composite materials. *Journal of Alloys and Compounds* **305**:246-252 (2000).
190. Zheng S, Fang, Zhang J, Sun L, He B, Wei S, Chen G and Sun D, Study of the Correlation between the Stability of Mg-Based Hydride and the Ti-Containing Agent. *The Journal of Physical Chemistry C* **111**:14021-14025 (2007).
191. Kircher O and Fichtner M, Hydrogen exchange kinetics in NaAlH<sub>4</sub> catalyzed in different decomposition states. *Journal of Applied Physics* **95**:7748-7753 (2004).
192. Xiao X, Fan X, Yu K, Li S, Chen C, Wang Q and Chen L, Catalytic Mechanism of New TiC-Doped Sodium Alanate for Hydrogen Storage. *The Journal of Physical Chemistry C* **113**:20745-20751 (2009).
193. Eigen N, Gosch F, Dornheim M, Klassen T and Bormann R, Improved hydrogen sorption of sodium alanate by optimized processing. *Journal of Alloys and Compounds* **465**:310-316 (2008).
194. Gross KJ, Sandrock G and Thomas GJ, Dynamic in situ X-ray diffraction of catalyzed alanates. *Journal of Alloys and Compounds* **330-332**:691-695 (2002).
195. Bogdanovi B, cacute, Felderhoff M, Kaskel S, Pommerin A and Schlichte K, Improved Hydrogen Storage Properties of Ti-Doped Sodium Alanate Using Titanium Nanoparticles as Doping Agents. *Advanced Materials* **15**:1012-1015 (2003).
196. Lee G-J, Shim J-H, Cho YW and Lee KS, Improvement in desorption kinetics of NaAlH<sub>4</sub> catalyzed with TiO<sub>2</sub> nanopowder. *International Journal of Hydrogen Energy* **33**:3748-3753 (2008).
197. Xu X and Song C, Improving hydrogen storage/release properties of magnesium with nano-sized metal catalysts as measured by tapered element oscillating microbalance. *Applied Catalysis A: General* **300**:130-138 (2006).
198. Price DL and Cooper BR, Total energies and bonding for crystallographic structures in titanium-carbon and tungsten-carbon systems. *Physical Review B* **39**:4945 (1989).
199. Chien F-R, Clifton RJ and Nutt SR, Stress-induced phase transformation in single crystal titanium carbide. *Journal of the American Ceramic Society* **78**:1537-1545 (1995).
200. Chien FR, Nutt SR and Cummings D, Defect structures in single crystal TiC. *Philosophical Magazine A* **68**:325 - 348 (1993).
201. Vrel DL, Lihrmann J-M and Petitot J-P, Synthesis of Titanium Carbide by Self-Propagating Powder Reactions. 1. Enthalpy of Formation of TiC. *Journal of Chemical & Engineering Data* **40**:280-282 (1995).
202. Kubas GJ, CHEMISTRY: Breaking the H<sub>2</sub> Marriage and Reuniting the Couple. *Science* **314**:1096-1097 (2006).
203. EnvironmentalChemistry, <http://environmentalchemistry.com/yogi/periodic/>.
204. Solymosi F, The bonding, structure and reactions of CO<sub>2</sub> adsorbed on clean and promoted metal surfaces. *Journal of Molecular Catalysis* **65**:337-358 (1991).

## PUBLICATIONS AND PRESENTATIONS

1. **Mi Tian** and Congxiao Shang, 'Nano-structured  $\text{MgH}_2$  catalyzed by TiC nanoparticles for hydrogen storage', *Journal of Chemical Technology & Biotechnology*, Article first published online: 20 Aug, 2010. DOI: 10.1002/jctb.2479
2. **Mi Tian** and Congxiao Shang, 'Nano-structured  $\text{MgH}_2$  catalyzed with TiC nanoparticles for hydrogen storage', *Oral Presentation* at The 16th Joint Annual Conference of The Chinese Society of Chemical Science and Technology in the UK (CSCST) & The Society of Chemical Industry—Chinese UK Section (SCI—CS), University of London, UK, October, 2009.
3. **Mi Tian** and Congxiao Shang, 'Synthesis and characterization of nano-structural  $\text{MgH}_2/\text{Mo}_2\text{C}$  mixtures for hydrogen storage', *Poster Presentation* at UK NanoForum & Emerging Technologies, London, UK, November, 2009.